A Minimalistic Co-Culture Platform for Alpha-Synuclein Spreading in Human Dopaminergic Neurons

Inauguraldissertation

zur

Erlangung der Würde eines Doktors der Philosophie

vorgelegt der

Philosophisch-Naturwissenschaftlichen Fakultät

der Universität Basel

von

Andrej Bieri

aus Oberkirch, Luzern

Basel, 2018

Genehmigt von der Philosophisch-Naturwissenschaftlichen Fakultät

auf Antrag von

Prof. Dr. Henning Stahlberg & Prof. Dr. Roland Riek

Basel, den 22. Mai 2018

Prof. Dr. Martin Spiess, Dekan

SUMMARY

Parkinson's disease (PD) is the second major neurodegenerative disease and the most common movement disorder. Due to age being a critical risk factor, the rapid ageing of the world population further increases the prevalence of PD. So far no treatment is available and therapies mainly focus on motor symptoms by pharmacologically substituting striatal dopamine, caused by the loss of dopaminergic neurons in the substantia nigra. This neuronal loss and intracellular protein aggregates, termed Lewy bodies (LBs), are pathological characteristics of PD. With disease progression, a spread of LBs through the brain can be observed which mainly follows axonal projections. Understanding the mechanisms of this progressive spread could be central to discovering the underlying molecular pathogenesis of the disease. As LBs mainly consist of alpha-synuclein (α-syn), a prion-like spreading of α-syn was suggested and is now widely accepted as a component in the PD pathogenesis. New dopaminergic model systems to study the exact mechanisms underlying α-syn spread are urgently needed. As PD is a human disease, *in vitro* models should be derived from humans. Lund human mesencephalic (LUHMES) cells are a suitable alternative to other, mostly non-human, dopaminergic cell lines. However, difficulties cultivating them in microfluidics devices has made them thus far inaccessible for co-cultivation studies in the field of PD spreading.

In the first part of this thesis, a human dopaminergic cell model system for studying the spreading of α-syn fibrils is presented. First, the well-characterized LUHMES cell line was tested for suitability of PD research on prion-like spreading, as no data is currently available on this matter. For the analysis, immunofluorescence light microscopy was employed. An extended period of differentiation aimed for a high degree of neuronal maturity and long neurites to facilitate the connectivity of spatially-separated cell populations. Seeding experiments with α-syn fibrils revealed a weak toxicity against these assemblies, even at prolonged differentiation. Second, to study the transmission of α-syn fibrils via neuronal projections, we developed a light microscopy-compatible microfluidic co-culturing device, to maintain two LUHMES cell populations in separate cell compartments for up to two weeks of differentiation. During this time, a neurite network is

formed which connects the fluidically isolated cell growth compartments. The ability to cultivate cells with neurites and soma in an isolated environment enabled seeding and transmission experiments in anterograde and retrograde directions.

In the second part of this thesis, implementation strategies of the microfluidic co-culturing chip for alternative analysis methods are discussed. Firstly, the accessibility of the cells in the co-culturing device using a single-cell lysis instrument is evaluated. The tool allows for targeted lysis of individual adherent cells. Preliminary tests point in a promising direction, while LUHMES single cell lysate was successfully transferred to different analysis techniques. However, direct access to the channels of the microfluidic co-culturing chip was problematic and needs further modifications. Secondly, an implementation of the microfluidic device aiming for co-cultivation of LUHMES cells on electron microscopy grids to study neurite architecture was pursued. Thereby, microfluidic devices harbor only cell soma, but neurites can grow onto an electron microscopy grid, as only they are thin enough to be visualized by cryo-electron microscopy. Proof-of-concept experiments demonstrate the direct visualization of LUHMES cell neurites in a near-native, frozen-hydrated state.

CONTENTS

List of Abbreviations

AADC	Amino acid acetyl decarboxylase
α-syn	Alpha-synuclein
AD	Alzheimer's disease
ALS	Amyotrophic lateral sclerosis
BBB	Blood-brain barrier
CFD	Computational fluid dynamics
CLSM	Confocal laser scanning microscopy
CNS	Central nervous system
COC	Cyclic olefin copolymer
DAT	Dopamine transporter
DBS	Deep brain stimulation
DDC	Dopa decarboxylase
DLB	Dementia with Lewy bodies
EtOH	Ethanol
GABA	Glutamic acid decarboxylase
GDNF	Glial cell derived neurotrophic factor
HD	Huntington's disease
hESC	Human embryonic stem cells
hpSC	Human parthenogenetic stem cell
HSPG	Heparan sulfate proteoglycans

iPSC	Induced pluripotent stem cell
ITO	Indium tin oxide
kDa	Kilo Dalton
LB	Lewy body
L-DOPA	Levdopa (3,4- dihydroxy-L-phenylalanine)
LUHMES	Lund human mesencephalic
MAOA/B	Monoamine oxidase type A and B
MeOH	Methanol
MHB	Modified Hank's buffer
MPTP	Methyl-4-phenyl1,2,3,6-tetrahydropyridine
MS	Mass spectrometry
NAC	Non-amyloid-β component
ND	Neurodegenerative disease
NaOH	Sodium hydroxide
PARK	Parkinson disease associated genes
PEG	Polyethylene glycol
PD	Parkinson disease
PDMS	Polydimethylsiloxane
PLO	Poly-L-ornithine
PNS	Peripheral nervous system
ROS	Reactive oxygen species
RPPA	Reverse-phase protein array
RT	Room temperature
SN	Substantia nigra
TEM	Transmission electron microscopy
TH	Tyrosine hydroxylase
WGA	Wheat germ agglutinin

CHAPTER 1

Introduction

This introduction provides a general overview of neurodegenerative diseases with a focus on Parkinson's disease. The relevant biological background for this thesis is discussed. Special attention was paid to a more detailed discussion about current knowledge of the Parkinson's-related protein alpha-synuclein in terms of disease outbreak and progression. Thereafter, an overview of microfluidics is given with regard to its upcoming role in cell culture and its advantages and disadvantages therein. Parts of this introduction are being prepared for publication elsewhere.

1.1 Neurodegenerative Diseases: A Global Public Health Problem

The umbrella term "neurodegenerative disorders" combines brain-affecting processes with progressive loss of normal neuronal function, neuronal degeneration, and death of neurons. As a result of progressing neurodegeneration, diseases like Alzheimer's disease (AD), Parkinson's disease (PD), Huntington's disease (HD), and amyotrophic lateral sclerosis (ALS) occur, and are therefore termed neurodegenerative diseases (NDs). Most mechanisms behind these incurable neuronal degenerations are not yet understood.

Often, the disease's typical neurological alteration in the cerebral and peripheral nervous system starts long before its diagnosis. Although the nervous systems usually cannot repair itself, it is often very robust to changes, which leads to a detection of NDs in advanced years. Partly because of ageing populations and worldwide demographic changes disease prevalence is likely to increase. Especially in less developed countries – often with higher exposure to environmental risks, increasing life expectancy, and large populations – NDs will become a problem too. The World Health Organization (WHO) predicts that by mid-century NDs will overtake cancer as cause of death [1]. The current mortality of NDs does not reflect the overall burden of the disease since disabling effects are mostly present over many years. Taking the WHO estimates for "Disability-Adjusted Life Years" to compare

the impact among diseases, brain diseases are developing to be one of the leading global disease burdens (Figure 1) [2].

However, NDs are far from being fully understood and therapies often bring only symptomatic relief but do not stop the progress of neurodegeneration. The growing knowledge about the various NDs gathered in the last four decades reveales many similarities between these diseases on a molecular basis. This brings in another level of complexity but also the hope that research findings and subsequent therapies might be applicable to several diseases simultaneously.

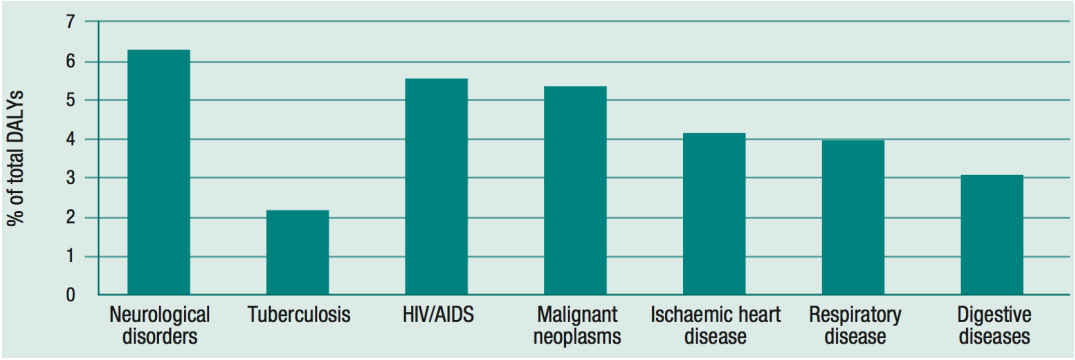

Figure 1. Percentage of total disability-adjusted life-years (DALYs) for neurological disorders and a selection of other diseases. One DALY is the equivalent of a healthy life year a disabled individual has lost. Modified from WHO report on Neurological Disorders 2006 [2].

1.2 Parkinson's Disease

Parkinson's disease (PD) was named in honor of James Parkinson who thoroughly documented the disease in "An Essay on the Shaking Palsy" in 1817 [3]. 200 years later, the disease is widely known by the public as it becomes increasingly prevalent, affecting approximately 0.1-0.2% of the population at any time [4]. Generally, the incidence increases with age, independent of gender [5]. The occurrence increases to over 1% of the population older than 65 years and to 5% when over the age of 80 [6]. The disease is not restricted to the elderly as 5% of diagnoses affects people under the age of 40. Young-onset PD is generally defined by an onset before the age of 45, with about 10% of patients showing a genetic predisposition. Genetically defined cases rise to over 40% of individuals with onset before 30 years of age [7, 8].

Gender differences were reported in several studies. In some, men are twice as likely to be affected than women [9-11]. Other studies only observed significant gender differences in prevalence among specific age groups or none when stratified by geographic location [5,

12]. PD is the second most common ND after AD, and represents the most common movement disorder.

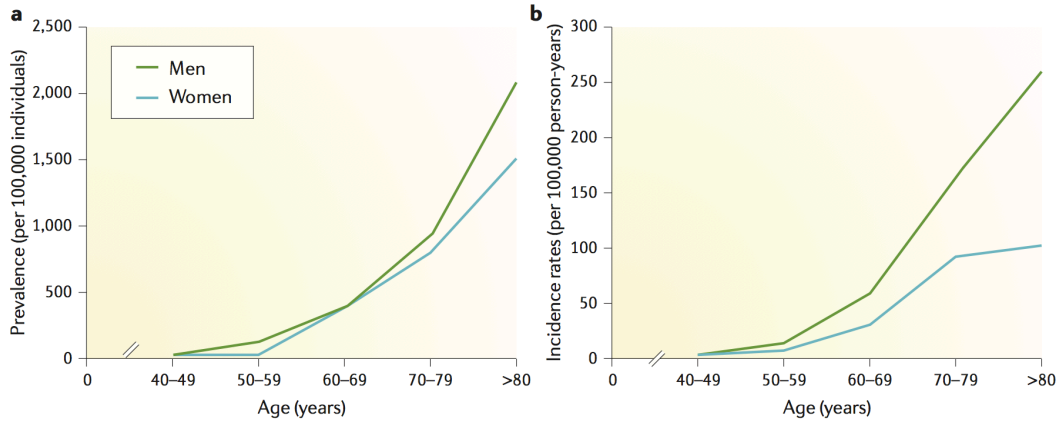

Figure 2. Prevalence (a) and Incidence (b) of PD in men and women. Reprinted with permission from ref [9]. Copyright (2017) Springer Nature.

1.2.1 Symptoms and Diagnosis

The characteristic motor features observed by James Parkinson are still considered the hallmark signs for idiopathic PD and are the prerequisite for clinical diagnosis. The motor aspects of the disease are bradykinesia, rigidity, and resting tremor, whereas in clinical diagnosis the obligated symptom of bradykinesia must be observed in combination with one or both of the other motor features [13]. Postural instability also used to be a diagnostic criterion, but this fourth cardinal sign was recently revised by the International Parkinson and Movement Disorder Society [4, 14]. However, only the main three motor symptoms are defined to be cardinal parkinsonism manifestations. If parkinsonism, the essential criterion of PD, is given, a range of supportive criteria, red flags, and absolute exclusion criteria are described to diagnose a clinically-defined PD patient [15]. Although older diagnostic criteria already increased the accuracy of clinical diagnosis up to 90% by including non-motor symptoms, the discrepancy between clinical diagnosis and pathological confirmation as gold standard persists [16, 17]. The newly defined supportive criteria also include non-motor symptoms which will probably improve the diagnostic accuracy.

However, the correct diagnosis of PD is important in order to evaluate possible and immediate therapeutic actions – the earlier the better. The difficulty is that parkinsonism can also occur in conditions other than PD. Still, with the help of defined criteria, the diagnosis remains primarily clinical. As no reliable test exists yet, clinicians are mainly forced to rule out other conditions leading to parkinsonism. This is usually the case for the

later stages of the disease and thus not useful for an early diagnosis. Besides misdiagnosed patients, there is an unknown number of unreported cases, mainly because only few develop cardinal signs under the age of 50. On the other hand, parkinsonian features in older populations are often mistaken for normal ageing signs [18].

Although clinical diagnostic techniques and laboratory analyses were developed, they do not make a defined diagnosis and can solely support the physicians in their final decision. By the 1980s ^{18}F-DOPA positron-emission tomography (PET) scanning techniques to visualize striatal dopamine (DA) depletion were demonstrated [19]. Since then, several other techniques in the field of neuroimaging were developed and approved for clinical diagnosis of PD. For example, the DaTscan (GE Healthcare) – a single-photon emission computer tomography (SPECT) technique – can be used to image dopaminergic degeneration by visualizing the amount of DA transporters [20]. This helps to distinguish PD from other diseases with similar symptoms. Several advanced magnetic resonance imaging (MRI) techniques are being developed for early disease detection and to monitor disease progression [21].

Besides imaging techniques, patients with early onset PD or a suggestive familial history can be tested for known genetic mutations. As PD is genetically heterogeneous and monogenetic forms only account for 3%-10% of the sporadic cases [22, 23], genetic testing is not yet a diagnostic routine, nor is it used for practical treatment decisions. However, many mutations leading to monogenetic PD are identified and the list of genes which contribute to a higher risk for sporadic PD continues to grow. With the application of genome-wide association studies, many low-risk loci were identified, which might account for an interacting effect in genetically heterogeneous PD [23]. Thus, advances in the field of genetics could make PD diagnosis based on genetic findings a tool in clinical routine.

Currently, there is no reliable test available that can achieve this task. Therefore, there is an urgent need for biomarkers to diagnose PD at a prodromal disease stage, that is, before cardinal signs show up, and to differentiate from other diseases but also to assess disease severity and prognosticate the course of the disease. To date, only a few biomarkers have been tested and there are currently none in standard clinical use, besides biomarkers for neuroimaging [24]. The general approach is to test for biochemical markers in cerebrospinal fluid or in the blood of patients. The most studied biomarker present in several biofluids is α-syn. The most prominent studies compared the total α-syn levels in the cerebrospinal fluid of PD patients with those of healthy control subjects. However, conflicting results with an overlap of α-syn levels in patients and healthy controls precluded clinical development as a diagnostic or prognostic biomarker [24]. A recent longitudinal study, which measured α-syn concentration changes in the cerebrospinal fluid of PD patients, did not show any substantial changes during a period of 4 years [25].

Similarly, biochemical markers quantitated in blood led to limited success. Despite the extensive search for biomarkers as a clinical tool, definitive diagnosis can only be made based on clinical symptoms in combination with neuropathological examination [26].

1.2.2 Neuropathology

The defining neuropathological characteristics of PD are loss of dopaminergic neurons in the substantia nigra (SN), which leads to DA depletion in the striatum, and abnormal intracellular protein aggregate formation [14, 27]. Currently, both of these neuropathological features are required to ultimately diagnose idiopathic PD. However, as with clinical diagnosis of PD, there are only provisional operating procedures and criteria used for the neuropathological assessment of PD [27].

The first hallmark of PD, neuronal loss, is not restricted to the SN but in early-stage disease predominantly affects the ventrolateral SN (Figure 3A). It is assessed by comparing pigmented melanine-containing neurons in the SN on histological sections with a control template. Other midbrain dopaminergic neurons might be affected at a later stage, whereas conclusions on disease duration can only be drawn from depletion in SN, not from other DA-containing cell groups [28]. Still, neuronal depletion is relatively localized in SN and a general atrophy of the brain is not typical for PD. Striatal DA deficiency and consequently onset of motor symptoms can be directly linked to the nigral neuronal loss via the nigrostriatal DA pathway and therefore to PD [29-32]. However, the loss of pigmented neurons in the SN is also observed in normal elders and in several other NDs [18].

The other neuropathological hallmark of PD is the cytoplasmic deposition of protein aggregates in different brain regions (Figure 3B-D). When located in neuron somas, they are termed Lewy bodies (LBs), and when the aggregates form in axons they are called Lewy neurites (LNs). The precise building block and the mechanism of formation of LBs remain unclear. The main constituents are neurofilament subunits, α-syn, and ubiquitin [33-35]. Furthermore, other proteins such as synaptophysin, synphilin-1, Tau, and heat shock proteins were found, as well as whole cell organelles, mostly mitochondria [36]. It was suggested that LBs might be related to aggrosomes, and thus are only a symptom, not the cause of PD [37].

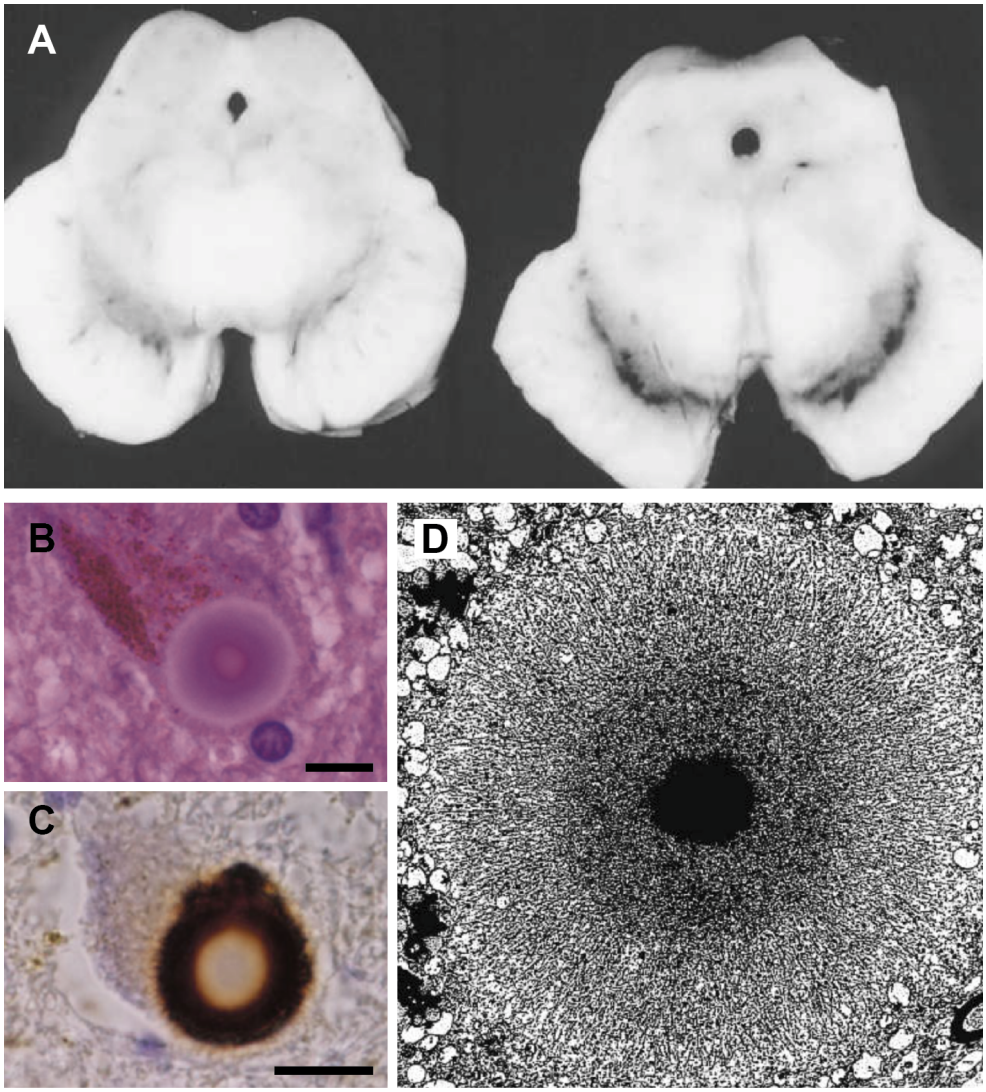

Figure 3. Demonstration of the pathological hallmarks of PD, Lewy bodies and depigmentation of the SN. (A) Horizontal sections through the midbrain of a PD patient (left) and a healthy control (right). Loss of pigmentation can be seen in the SN. (B) Concentric LB on a conventional haematoxylin and eosin stained histological section. (C) LB stained against α-syn. (D) Electron micrograph of a LB reveals a dense core and radiating filaments. Scale bars 10 µm. Reprinted and modified with permission from refs [38-40]. Copyright (2013) Springer Nature, (1996) Oxford University Press.

Initially, LBs are formed in monoaminergic and cholinergic brainstem neurons and in neurons of the olfactory system. With the progression of the diseases, they can also be found in limbic and neocortical brain regions [41]. In PD, Lewy pathology is often found at sites of neuronal loss. This has led to the conclusion that LBs might be the reason for neuronal degeneration [42]. Although more LBs can be found in patients with less severe neuronal depletion, it does not mean that all the lost neurons were affected by LBs and died. Indeed, it was shown that most SN neurons do not contain LBs when undergoing apoptotic cell death. Therefore, it was also not possible to correlate LB density with clinical disease symptoms or disease duration [43]. As for nigral neuronal degeneration,

LBs can also occur as a feature of normal ageing and in several other NDs, including dementia with Lewy bodies, AD, subacute sclerosing panencephalitis, Down's syndrome, infantile neuroxanal dystrophy, and Hallervorden-Spatz syndrome [18, 44]. Therefore, LBs are most likely not a sign of presymptomatic PD [27]. Overall, this pathophysiological feature of PD does not explain the neurodegeneration and is probably not even associated to the cell loss [43, 45].

For a definitive diagnosis of PD, LBs must be found in the SN or in the locus ceruleus in combination with nigral neuronal loss and cardinal clinical signs as obligated symptoms [14]. The postmortem findings can be quite challenging and conflicting to interpret, as individual pathological features can be heterogeneous. There may be patients with typical clinical symptoms but no LB pathology or nigral neuronal degeneration [46]. Still, based on the general neuropathological findings, a staging system was proposed to evaluate the progression of PD post-mortem [47]. This system, developed by Braak and colleagues, categorizes six stages with distinct topographical localization of the brain lesions, which is linked to a spatiotemporal route of Lewy pathology spreading (Figure 4). Therefore, an initial site of PD-related brain alteration had to be determined and defined in stage 1 and 2 as specific regions in the lower brainstem [48]. More precisely, in the dorsal vagal nucleus of the medulla oblongata and the olfactory bulb in stage 1, with spreading to medullar structures like the locus coeruleus and lower raphe nuclei in stage 2. In stages 3 and 4, the severity of these previously located lesions increases and spreads to the upper brainstem without cortical lesions, and it is not till stage 4 that a depigmentation in the SN is detectable. This devastation of the melano-neurons is likely to be the clinical manifestation of PD onset. Eventually, initial lesions in the mesocortex can be found in stage 4. In the final stages, 5 and 6, the destructive process of previously staged regions proceeds and the involvement of the neocortex becomes extensive [49].

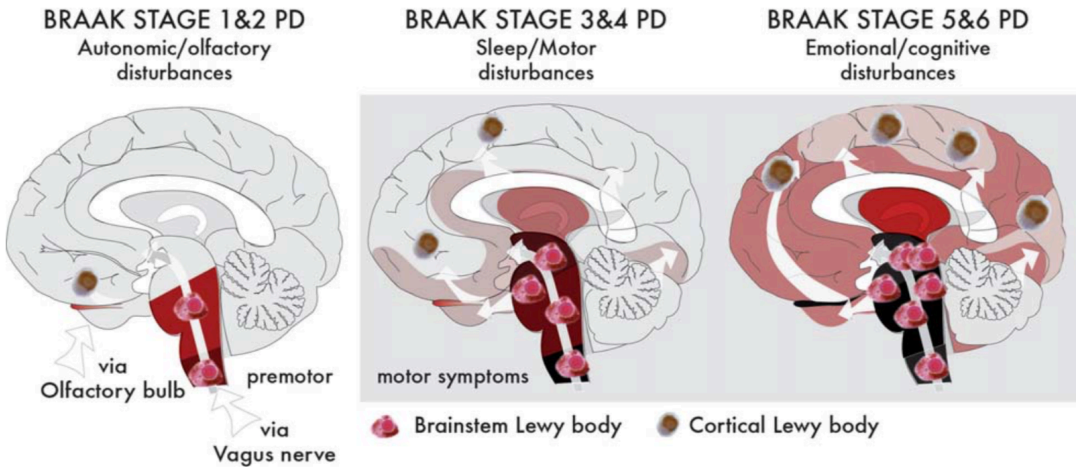

Figure 4. Representation of the Braak staging system for PD. Lewy pathology spreads from the possible initiation site in the olfactory bulb or via vagal inputs to the cortical regions. Reprinted from ref [41] with permission obtained from John Wiley and Sons. Copyright (2011) Movement Disorder Society.

However, due to significant heterogeneity in neuropathological examinations, several critical reappraisals suggested modifying the criteria of the Braak staging [50-52]. Especially with regard to the Lewy pathology, it was reported that half of the subjects could not be classified with the current staging system. The Braak hypothesis then also fails to explain why parkinsonism cannot be found in all patients with the characteristic Lewy pathology [53], or why not every PD pathology follows the predicted spreading pattern [54]. This shows the complexity of the disease and that several factors might influence initial disease outbreak, eventually leading to alternative spatiotemporal progression routes [55].

1.2.3 Pathophysiology

Based on neuropathological findings, the cardinal signs of PD can be explained by the loss of neuronigral substance [4]. But neither is there a clear clinical manifestation of the other neuropathological hallmarks LBs and LNs, nor can the significance of the pathological brain depletion explain clinical symptoms like dementia, depression, and several other non-motor symptoms.

With the discovery that PD patients' brains show a severe loss of DA in the caudate nucleus and the putamen, combined with the knowledge about the loss of SN neurons, which also show greatly reduced DA levels, a link between striatum and SN was concluded [31]. This so called "nigrostriatal DA pathway" starts in the SN where the cell bodies of the dopaminergic neurons are located and follows neuronal projections that lead to the dorsal striatum. Since these regions are critical for the motor system, neuronigral

depletion and subsequent reduction of DA leads to the symptomatic motor symptoms of PD, but not until 50% of the dopaminergic neurons in the SN are lost [50, 56].

Non-motor symptoms, including sleep disorder, cognitive impairment, autonomic dysfunction, and sensory symptoms are not easily explained by DA depletion. Several of these symptoms can precede the onset of the classical motor symptoms by more than a decade. Interestingly, some are partially treatable with dopaminergic drug strategies [57]. However, some of the physiological processes may be explained by Braak's hypothesis. For example, olfactory dysfunction can be a result of a degeneration in the olfactory bulb and the olfactory nucleus in Braak stage 1. Progression to the lower brain stem in Braak stage 2 might explain the involvement with sleep homeostasis and the links to other autonomic dysfunctions [58]. The role of LBs can only be indirectly assumed via their possible relation to brain lesions. It is only partially possible to assign the clinical signs to multiple sites of the pathology. How LBs and nigral pathology produce the clinical signs is not yet understood is the subject of intense debate [18, 50].

1.2.4 Epidemiology, Etiology, and Risk Factors

The etiology of PD remains unclear in most cases, with some being associated to genetic or environmental risk factors. It is agreed that increasing age remains the greatest risk factor for PD [59]. The lifetime risk of developing PD is as high as 6.7% at an age of 45 and the annual incidence increases nearly exponentially between the age groups of 60-64 and 85-89, from 0.07% to 0.6% [60]. The prevalence of several other diseases like AD and heart disease increase with ageing too, but none of them show such a marked increase as PD [61]. Ageing itself is a complex phenomenon. It is characterized by a progressive deterioration of physiological process, but the involved cellular mechanisms are only poorly understood. Besides PD, susceptibility to other diseases increases, but varies among individuals of a population and even in the different tissues of an individual [62]. Thus, age-related alteration of the brain is a risk factor for PD, but must not be regarded solely, since other PD risk factors might have simultaneous impacts on the mechanisms of ageing itself. That is to say, genetic and environmental factors influence ageing and ageing itself can lead to different responses to these factors. Some studies consider that PD is caused by a specific risk factor, which affects a certain population of dopaminergic neurons [61]. These neurons are usually also affected by normal ageing. Thus, there might not only be a single etiopathogenesis for neurons to degenerate in PD, but the condition arises because affected neurons might be particularly vulnerable to ageing in combination with other risk factors [63]. These competing theories are discussed in more detail in section 1.4.3.

In epidemiological studies, gender differences were reported with men carrying up to a twofold increased risk of developing PD compared to women [11]. In contrast, other studies did not observe any differences or even a higher risk for the female population

[64]. However, the general consensus tends to see gender differences, with PD in men being more common (Figure 2). A possible role of oestrogen as neuroprotective agent has been discussed [65], but gender-specific differences in exposure to environmental factors and healthcare discrepancies like underdiagnoses could also contribute.

Furthermore, different PD rates were found among a geographically defined population with different race and ethnicity, but evidence for biological causes could not be found, which leaves social causes as a possible explanation for these findings [10]. Generally, epidemiologic studies have to be carefully assessed since race and, therefore, genetic differences can have a dominant role over environmental contribution or vice versa. For example, increased prevalence was detected in Ashkenazi Jews [66], Native Americans, Alaska Natives [67], and Inuit [68], but could not be explained solely by either genetic or environmental factors.

Accumulation of PD cases in certain family trees led to the assumption of a genetic cause for the disease. It was not until 1997 when the first PD mutation, Ala53Thr in SNCA on chromosome 4q22.1, was discovered [69]. However, it was already clear by then that a single gene or even a single mutation cannot account for most of the sporadic and familial cases. Since then, more of these potent monogenetic causes of PD were discovered. Most significantly, the autosomal-dominant SNCA and LRRK2, but also autosomal-recessive PINK1, PARKIN, and DJ1, which – based on family history or early onset PD – were particularly amendable to discovery. It is believed that all monogenetic causes of PD are known and well described [70]. However, they are comparatively rare in familial PD and likely make only a small contribution to the etiology of PD. Together, they account for 5-10% of all PD cases [23], whereas it is estimated that heritability accounts for 27% overall [71]. To date, 23 gene loci were assigned to the “PD associated genes” (PARK) designation. Besides the known monogenetic forms, larger population-based studies found genetic low-risk factors within these genes, and new loci in which mutations are more frequent than in monogenetic PD but with a lower penetrance [72]. Genome-wide association studies have proven to be a powerful tool to identify and confirm more of the highly frequent low-risk variants which account for a small contribution to the risk of PD [73]. The interaction of these genes and their contribution to sporadic PD pathogenesis has become apparent during recent years but are yet to be understood [74].

In addition to this polygenetic etiology, it is presumed that multiple other factors like epigenetics and somatic mutations participate in the pathology of PD. There is growing evidence that epigenetic modifications introduce environmental risk factors into the disease development with multifactorial origin [75]. How and to what extent epigenetics act as a mediator for the gene-environment interaction remains to be elucidated [76]. However, environmental factors are considered to have an important role in PD

pathogenesis. Some studies have related the increase of PD during the industrial revolution to environmental toxins, some to the ageing of the population [77]. Epidemiological studies indicated an increased prevalence of PD in rural areas, likely due to elevated levels of environmental toxins from pesticides, herbicides, and insecticides [78]. Other factors like air pollution and metal emissions tend to have a higher influence in urban areas [79, 80]. It was hypothesized that biological and clinical factors such as influenza viruses, endotoxins from bacteria, and traumatic brain injury could act as indirect causes of PD [81-83]. Additionally, lifestyle factors including dietary factors could positively or negatively correlate with the incidence of PD, for example, it is lower in caffeine consumers and smokers but increases with a diet low in antioxidants [84].

Despite the evidence that environmental risk factors correlate with increased prevalence of PD, it would be an oversimplification to consider exposure to certain toxins a sole trigger for PD. For example, a meta-analysis of studies related to PD and pesticides revealed significant heterogeneity in the results, which may be biased by PD pathogenesis-related genes, different pathological mechanisms, and variations in patients [78]. Thus, it has become clear that PD has a multifactorial and polygenetic etiology defined by several factors including age, gender, race, genetic predisposition, and environment.

1.2.5 Therapy

1.2.5.1 Pharmacological Treatment Strategies

Unlike for other NDs, the list of treatment options for PD is quite unique with several effective medications used for symptomatic relief. Still, there is no cure or therapy that slows the progression of the disease currently available.

With the discovery that DA plays a role in the pathophysiology of PD, a key target for pharmacological treatment was found. Consequently, DA replacement treatments were started, first with intravenous and later with oral administration of the DA precursor L-DOPA [85-87]. More than 50 years after this revolutionary breakthrough, L-DOPA is still the most powerful drug against PD and almost all patients will eventually receive L-DOPA treatment at some point [88]. Co-administration with inhibitors of the aromatic amino acid decarboxylase is necessary to prevent early DA formation from L-DOPA, because DA is not able to cross the blood-brain barrier (BBB) and is further converted to norepinephrine. Since the use of such inhibitors shifts the metabolism of L-DOPA to another pathway, catechol-O-methyltransferase inhibitors are additionally administered to prevent further degradation. Advances in therapy often focus on more efficient administration or alternative delivery of L-DOPA to the brain and on preventing the side effects of long term therapies. The main complication upon chronic L-DOPA treatment is the development of dyskenesias among other motor and non-motor fluctuations [89]. The reason for the L-

DOPA-induced complications are still poorly understood, but irregular dosage due to rapid peripheral clearance, and variability in uptake and transport may affect such clinical responses [90]. The pharmaceutical industry, therefore, concentrates on novel release formulations and a more continuous delivery to improve the clinical response.

With L-DOPA still being the gold standard in PD treatment, deeper understanding of the nigrostriatal pathway revealed other possible targets in the dopaminergic system. Besides the peripherally active inhibitors to prevent the metabolism of L-DOPA, targeting the synaptic clearance of dopamine itself is an established treatment. For example, monoamine oxidase type A and B (MAOA/B) inhibitors, like selegiline and rasagiline, increase the synaptic concentration of dopamine [91]. Interestingly, selective inhibition of MAOA or MAOB does not alter the striatal dopamine levels [92].

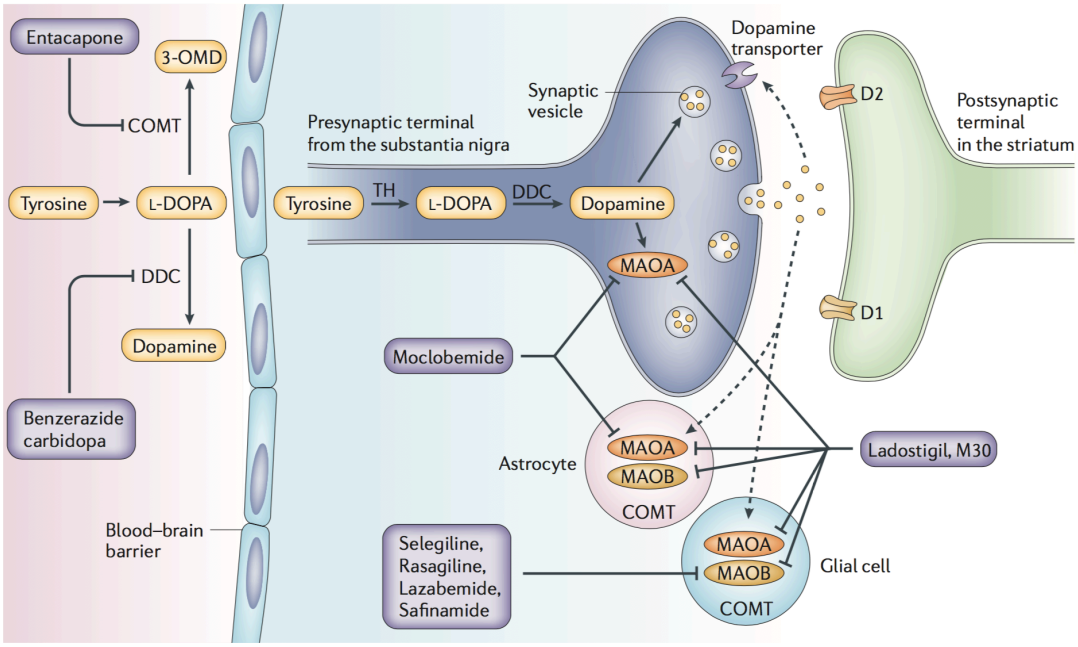

Figure 5. Schematic overview describing dopamine biosynthesis and metabolism. Natural L-DOPA is produced from the catalysis of the amino acid Tyrosine with the enzyme Tyrosine Hydroxylase (TH). Subsequently, Dopamine is the result of L-DOPA by decarboxylation with dopa decarboxylase (DDC). Since Dopamine itself cannot cross the BBB but L-DOPA can, the synthesis has to be blocked by DDC inhibitors that cannot cross the BBB. Dopamine metabolization happens by monoamine oxidase A and B. To efficiently increase striatal dopamine levels, both MAOA/B have to be inhibited. Reprinted with permission from ref [93]. Copyright (2006) Springer Nature.

Furthermore, there are also postsynaptic active treatment strategies available. Dopamine agonists act directly on dopamine receptors and are often used in combination with L-DOPA to prevent motor fluctuations. The main advantage of these agonists is their longer half-life and the possibility for continuous administration via transdermal patches.

Unfortunately, the effects are much smaller compared to L-DOPA and possible side effects, such as drowsiness and loss of impulse control, are serious drawbacks [94].

Besides the mentioned symptomatic dopaminergic therapy, there is a need for therapies that focus on the L-DOPA-induced complications and on the non-motor symptoms. Since non-motor symptoms originate from various regions in the nervous system, PD seems to have impacts on other parts of the nervous system apart from the dopaminergic pathways. Amantadine is the only drug for L-DOPA induced dyskensia currently in clinical use, although its efficacy is still a controversy [9, 95]. Often, the non-motor symptoms such as cognitive dysfunction, autonomic failure, and depression cannot be reduced by dopaminergic therapy strategies and can even be aggravated [57]. Clozapine is currently the most efficient drug to treat PD-related psychosis that does not worsen parkinsonism. Depressions – which are widely spread among PD patients – can be treated with common tricyclic antidepressants and serotonin reuptake inhibitors. Additionally, there are several drugs available to treat the autonomic failure in late-stage PD. In particular, droxidopa is used as special PD drug for postural hypotension, and common drugs to treat incontinence and constipation are available.

1.2.5.2 Non-Pharmacological Treatment Strategies

Besides pharmacological management to treat PD, there are surgical treatments and various non-invasive and experimental treatment options available. In cases of surgical treatments, deep-brain stimulation (DBS) has mainly replaced all other ablative procedures [96]. It needs the correct surgical implantation of small electrodes in either the globus pallidus internus or the subthalamic nucleus. These can be programmed to fire high-frequency pulses usually of 130-185 kHz to reduce the inhibitory state of the thalamus. The mortality of DBS's surgical implantation lies below 0.5%, but there is no guarantee of success with the therapy [97]. The candidate's response to L-DOPA is an important criterion for a benefit-risk profile. Generally, DBS is favourable if the patient has an excellent response to L-DOPA but develops long-term motor complications. On the other hand, patients with no improvement of motor symptoms upon dopaminergic treatment also do not respond to DBS. Although there is only poor evidence for a neuroprotective effect of DBS, motor symptoms and the severity of L-DOPA-induced dyskinesia can be improved significantly in certain patients [98].

Additional non-medical and non-surgical therapies include physical exercise, occupational therapy, language therapy, and cognition therapy. Various studies have documented the positive effects on motor and non-motor disabilities in PD [99]. Especially physiotherapy with exercises seems to help in disabilities like mobility, balance, and speech functions when the patients respond poorly to drugs and DBS [100].

1.2.5.3 Alternative Therapeutic Strategies and Clinical Trials

Since α-syn is now widely regarded as a key contributor to the sporadic form of PD it has become a high value target for drug development. The main purpose is to identify and inhibit pathological species from transmission to other cells. Since α-syn accumulates in LBs, the hallmark of PD, prevention of such aggregate formation and its clearance may bring a disease-modifying effect. If α-syn really is involved in the disease progressing mechanisms, these strategies might even have a disease-halting effect. Currently, several anti-α-syn strategies are being pursued in clinical trials. The two most advanced strategies are both based on immunotherapy to remove toxic forms of α-syn and to stop the passing of the condition from one cell to another. AFFITOPE®, also called PD03A, from the company AFFiRiS, is a vaccine based on a α-syn-mimic plus an adjuvant for which a Phase II efficacy trial is currently planned. Besides this active immunization strategy, the company Prothena has developed a drug with a passive immunization approach [101]. PRX002, also called RG7935, is an anti-α-syn monoclonal antibody drug currently in Phase II clinical trial [102]. Other anti-α-syn drugs in early-stage trials are BIIB054 from Biogen, ACI-870 from AC Immune, NPT088 from Proclara Biosciences, and NPT200-11 from NeuroPore Therapies Inc.

Gene therapy is another strategy to overcome nigral neuronal loss and reduced dopamine levels by increasing the expression of disease-relevant proteins on site. Mainly two strategies are being tested to either increase expression of growth factors or enzymes in neurotransmitter synthesis pathways. All the gene therapies in human trials used either adeno-associated viral vector serotype 2 or lentivirus vector platforms [103]. Two PD gene therapies aimed for a neurotrophic factor approach by increasing the expression of neurturin or glia cell-derived neurotrophic factor. This could be an important step to form a neuroprotective environment for the remaining brain tissue in case a drug for slowing down PD progression is found. Another three approaches have tried to improve motor symptoms by indirectly increasing levels of GABA or DA via expression of glutamic acid decarboxylase or DDC and tyrosine hydroxylase (TH). So far, all five clinical gene therapy approaches in PD showed low efficacy, with some still being tested in clinical trials [104]. Nevertheless, the trials showed that viral vectors can be safely delivered to the brain and the foreign genes can be expressed without serious long term adverse effects. These progressions in the field provide an important basis for future trials.

Besides stopping PD from progressing, bringing symptomatic relief for the patient, and stabilizing the condition in a neuroprotective environment, there is a need for replacing the affected cells. Unless there are early disease markers, parkinsonism is only diagnosed after half of the dopaminergic neurons in the SN have already been lost. Consequently, stopping disease progression will not provide normal motor function without further dopamine

replacement. The two strategies for a cell replacement-based therapy are either based on fetal cells or stem cells. The relatively old-fashioned approach of transplanting dopaminergic cells from aborted embryos or fetuses showed promising motor improvements in early reports. It even created some long-term improvements in a few patients, but limited beneficial effects overall, as well as adverse effects like graft-induced dyskinesias, were reported in several other clinical programs and contradicted these initial trials [105-107]. On the basis of a re-evaluation of these early studies, a new trial with fetal ventral mesencephalic dopaminergic cells was designed and is currently ongoing. This European clinical trial, known as TRANSEURO, aims to find a solution for graft-induced dyskinesias, which is important for future trials, especially when stem cell grafting in humans is being initiated [9, 106].

The second ongoing clinical study for cell replacement – the very first using stem cells – is being conducted by International Stem Cell Corporation (www.internationalstemcell.com). The company will be using human parthenogenetic neural stem cells (hpNSC), which are produced by chemically triggering cell division of unfertilized female egg cells. Using this process called parthenogenesis to produce cells for transplantation has the advantage of not destroying viable organisms as it is the case with embryonic cells, fetal cells, and embryonic stem cells. However, the GForce-PD consortium criticized these trials for being premature [108]. This international initiative of leading scientists working on stem-cell therapy for PD are discussing key issues to translate stem cell treatment in PD to a safe clinical model [106]. Besides hpNSC and human embryonic stem cells (hESCs), human induced pluripotent stem cells (iPSCs) can also be used to generate dopaminergic neurons, though hESCs seem to have the most potential [106]. However, using iPSCs would avoid most ethical problems associated with hESCs transplantation. The development of new differentiation protocols has brought hESCs to a similar level of efficacy as fetal dopaminergic neurons when tested in animal models [109]. Thus, the launch of stem cell grafting in human trials seems to be feasible within the next years.

Another important issue that has to be considered regarding the long-term effects of such neuroregenerative strategies is that the pathology itself might affect the newly grafted tissue. In 2008, two studies showed that grafted embryonic dopaminergic neurons developed LB pathology in patients a decade after transplantation [110, 111]. It is likely that this will also be the case for stem cell grafting. This additionally exemplifies the urgent need for disease-modifying therapies in PD in order to avoid a compromise of neuroregenerative therapies. Nevertheless, the effects on grafted tissue might impair its function only after a decade, since the pathology progresses slowly and does only affects a minority of transplanted cells. Thus, the transplanted neurons could potentially be of therapeutic value for an extended period [112].

1.3 Alpha-Synuclein

1.3.1 α-Synuclein in Parkinson's Disease

The first time α-syn drew the attention of scientists was when its involvement in AD was discovered. In 1993, it was isolated from amyloid plaques in AD brains and was first called NACP, for non-amyloid component of plaques [113]. Later it was renamed to alpha-synuclein due to the homology with synuclein from *Torpedo* electroplaques, where the name originated from the high abundance of synuclein in both synapses and nuclei of neurons [114]. The first link to PD was drawn in 1997 when a missense mutation A53T of α-syn was discovered in the "Contursi kindred" – relatives of a family branch originating in the town of Contursi Terme – with apparent autosomal-dominant PD [69, 115]. This was also the first discovery of a genetic cause leading to PD. Additional mutations in the SNCA gene were discovered in the following years, which supported the evidence of an involvement of α-syn in PD. The most important autosomal-dominant mutations are A30P and E46K [116, 117], along with the more recently discovered H50Q and G51D [118, 119]. Autosomal-dominant forms of PD were also reported for duplication and triplication in the SNCA gene, providing evidence that increased α-syn expression may result in a causal increased risk of developing PD [120, 121].

The most supporting discovery was made in 1997, soon after the first PD gene was found, showing that LBs were strongly immunoreactive to α-syn [33]. Sensitive antibody labeling soon replaced ubiquitin staining for detecting LBs and most importantly was applicable to sporadic PD and DLB [122]. This demonstrated that α-syn is most likely involved in more than only some specific types of monogenetic PD [123]. However, it is still unclear how α-syn is involved in PD and other α-syn-related pathologies.

1.3.2 Structure

The SNCA gene consist of 6 exons with a size of 42 to 1110 base pairs. Exon 2 encodes the start codon ATG and the translation stops at a TAA stop codon which is encoded by exon 6. The full-length α-syn is the predominant form, but shorter isoforms have been reported as well [124]. α-Syn is an acidic protein (pK_a of 4.7) of 140 amino acids with a molecular weight of 14.46 kDa.

The alpha helical lysine-rich amino terminal domain (residues 1-87) has a crucial role in membrane interaction. It is a positively charged region, including seven series of 11 amino acid repeats which contains a highly conserved KTKEGV motif (Figure 6). The ability of α-syn to interact with lipid membranes is attributed to this repeat sequence which is similar to the α-helical domain of apolioproteins [125]. The core region (residues 65-90) contains a highly hydrophobic motif and is known as non-amyloid-β component (NAC), as this was the region of α-syn that was first purified from AD amyloid plaques [113]. The NAC

region is involved in α-syn amyloid formation because it can form cross β-sheets [126, 127]. The acidic carboxyl-terminal domain (residues 91-140) is disordered and might be an important reaction site for small molecules, metals, and proteins. It contains 10 glutamic and 5 aspartic acid residues, which gives the tail a low hydrophobicity with a high net charge and thus, a random coil structure [128].

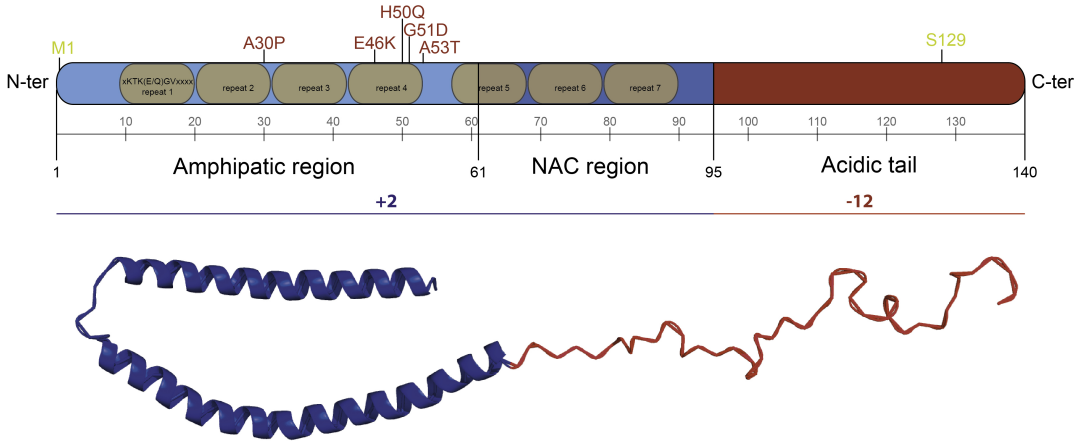

Figure 6. Domain organization of α-syn. Common mutations in hereditary PD are labeled with red font. The blue parts show the N-terminal region with a positive charge, the red region shows the negatively charged C-terminus. The full length human micelle-bound α-syn structure was determined by NMR (PDB ID: 1XQ8) [129].

When expressed in *Escherichia coli*, α-syn predominantly exists as a stable intrinsically disordered monomer with few secondary structures [130]. In physiological conditions an unfolded monomer is expected to be susceptible to degradation, which is not in agreement with the high abundance of α-syn in various brain regions [131]. Therefore, oligomerization or association with other proteins and subsequent structural and functional changes were proposed. Indeed, a predominant oligomeric α-syn form could be isolated from mammalian cells, red blood cells, and even from *Escherichia coli* [132, 133]. These studies used NMR, SEC, chemical crosslinking, and native PAGE to show that α-syn folds to a tetrameric α-helical form, which seems to be resistant to aggregation. Conflicting results from other studies could not verify these findings, and showed in native gels that α-syn derived from mammalian cell lines and red blood cells, or isolated from mice, rats, and human brains behaved similarly to stable unfolded α-syn produced in *E. coli* [134]. Additional NMR data ruled out a substantial population of stable oligomers but still recommended dynamic oligomer species that exist in an equilibrium with unfolded monomers [135].

The conformational flexibility of α-syn seems to allow the protein to adapt specific conformations depending on the interaction partner, such as membranes or other proteins. For example, an α-helical α-syn structure is stabilized upon binding with synthetic phospholipid membranes [125]. Several factors, including oxidative stress, post-translational modifications, and the concentration of membrane constituents, were shown to shift the equilibrium from monomeric to different conformational or oligomeric states [131]. So far, little is known about the regulation of interaction and equilibrium mechanisms with different conformational or oligomeric changes of α-syn. Knowing how the conformational variability is involved in α-syn toxicity would be a crucial factor in targeting α-syn for therapeutic reasons. Currently, there are no studies resolving the α-syn oligomeric structure at a high resolution, likely due to a high heterogeneity of the formed oligomers. However, cryo-TEM single particle reconstruction of *in vitro*-produced α-syn oligomers showed that a hollow cylindrical architecture was a characteristic to all the heterogenous species, despite variations in size, β-sheet content, and exposed hydrophobicity [136]. This cylindrical architecture is similar to the amyloid fibrillary structure, suggesting that these oligomers which accumulate during the process of fibril formation are kinetically trapped in this state. In other studies, several more species have been observed including annular and chain-like oligomers and more might exist [137].

Besides the oligomeric species of α-syn, protofibrils and fibrils have been associated with the pathology of PD. Radially-oriented filaments were observed in early electron microscopic studies of LBs [32, 35]. Later, filaments were extracted from PD patients' brains, which stained strongly with anti-α-syn-antibodies [122, 138]. Initial thoughts were that these aggregates of fibrils have the purpose of clearing toxic oligomeric species to form more stable fibrils with reduced toxicity. However, it was shown that the PD-linked mutations A53T and E46K enhance the fibril formation *in vitro* and in animal models [139].

During *in vitro* reconstitution, several different polymorphisms of α-syn fibrils were observed, including ribbon-like and helical filaments [140]. A number of studies determined the NAC region as crucial for such aggregations. For example, deletion of residues 71-82 within this region prevents the fibril formation, but the 12-residues segment itself can undergo self-aggregation [141]. Other regions outside of NAC are less crucial but can influence the filament structure. Electron paramagnetic resonance spectroscopy studies indicated a highly-ordered NAC region and a less ordered N-terminal region with heterogeneous secondary structures. The C-terminus is completely unfolded [142]. To date, no full-length structure of any α-syn fibril species has been determined. However, a central segment of the NAC domain with the crucial role for fibrillization (residues 68-78) was synthetically produced and the atomic resolution structure has been determined by

micro-electron diffraction [126]. The observed pairs of face-to-face β-sheets form the spine of the fibril.

Recently, a cryo-EM structure of α-syn fibrils (residues 1-121) has been reported [143] where two protofilaments form the fibril. Interestingly, the NAC region in this structure was located at the center of a single protofilament, and therefore, cannot be responsible for the interaction between two protofilaments but rather contributes to the filament formation. Additionally, several familial SNCA mutations have been located at the core of the fibril, where they would compromise fibril formation and stability.

1.3.3 Interaction Partners

The physiological function of α-syn and its role in PD is not entirely understood. However, its role can be associated with its ability to interact with membrane lipids and with many proteins [128]. After the discovery that α-syn interacts with membranes in cell cultures and brain tissue *in vitro*, experiments with membrane mimics and physiologically relevant membranes were started to describe the α-syn-lipid interaction and to elucidate the membrane properties that affect the binding [144]. Binding experiments with liposomes comprised of different types of lipids suggested an electrostatic interaction with the lysine rich α-syn N-terminus. It was observed that α-syn only binds to anionic not zwitterionic lipids [125]. The preferred binding to negatively charged headgroups is in agreement with the physiological interaction of α-syn with phospholipids in biological membranes [145, 146]. Upon membrane binding, the natively unfolded α-syn adopts a α-helical structure exclusively on the N-terminus, which is in contrast to the β-sheet formation in α-syn fibrils [147]. Furthermore, studies demonstrated the ability of α-syn to bind to small and large unilamellar vesicles with diameters of 10-100 nm and 100-1000 nm respectively [148]. The binding was stronger to the small vesicles and binding to giant unilamellar vesicles with a diameter larger than 1 μm was drastically reduced. This suggests that the membrane curvature has a strong effect on the membrane binding affinity of α-syn [149]. Furthermore, the binding affinity is affected by small packaging defects in the lipid ordering [150]. Taken together, binding of α-syn monomers to lipids is accompanied by α-helix formation of the N-terminus and happens preferentially on negatively charged lipids in membranes with high curvature and defect structures.

Besides the ability of α-syn to bind to membranous structures, it is possible that certain physiological or disease-related functions are caused by its ability to interact with many proteins. For example, an interaction with tubulin was suggested, since the formation of α-syn fibrils is accelerated by inoculating the reaction solution with tubulin [151]. On the other hand, oligomeric species α-syn can inhibit the polymerization of tubulin into microtubules [152]. Co-immunoprecipitation studies also indicated a relation between α-syn and LRRK2 although a direct biochemical interaction was not shown. It is assumed

that both proteins are involved in many common intracellular and potential pathogenic pathways, including microtubule assembly, function of mitochondria, and autophagy [153]. Furthermore, it was shown that A53T and A30P mutants of α-syn interact with syniphilin-1 in a different way than wild type α-syn. Instead of protecting α-syn from degradation by the proteasome [154], the mutant forms only bind and increase the number of α-syn-syniphilin-1 complexes [155].

A list of interaction partners at the presynaptic terminal is compatible with a possible neurotransmitter regulation function of α-syn. Like mutations in LRRK2 and SNCA, mutations in parkin are a cause of familial PD. All three proteins are involved in synaptic vesicle dynamics, where they might interact with each other. Additionally, direct binding of α-syn NAC domain to the DA transporter (DAT) was reported. It was suggested that this interaction leads to membrane clustering of DAT, and thereby to enhances DAT activity with subsequent increased levels of intracellular DA, which can be damaging to neurons [156]. Further presynaptice protein interactions of α-syn include SNARE complex, synaptobrevin-2, vesicle-associated membrane protein 2 (VAMP2), rab3, and synaptic vesicle proteins synapsin III and synaptophysin [157].

1.3.4 Function

Human α-syn is mainly expressed in the SN, neocortex, hippocampus, thalamus, and cerebellum, where it is located predominantly at presynaptic terminals in a soluble state [158]. The nuclear localization of endogenous α-syn was never confirmed in humans and is the subject of controversial debates [128]. Several studies reported the existence of recombinant α-syn in nuclei of mouse brains and cell cultures [159]. In mice, a co-localization with histones was observed as a consequence of exposure to the herbicide paraquat and subsequent increased concentration of α-syn in nuclei [160] or upon overexpression of α-syn in transgenic mice [161]. The physiological and pathological importance of these findings are not clear at the present time.

Several immunohistochemical studies have reported a predominant synaptic co-localization of α-syn and subcellular fractionation revealed an extensive synaptosomal localization [162]. Because α-syn has later been detected in vesicular fractions of the human brain [163] and α-syn binding to liposomes was demonstrated [125], the physiological function of α-syn was assumed to be associated with synaptic vesicles. Primary cell cultures with suppressed expression of α-syn showed a decrease of the vesicular pool [164]. A modest overexpression of α-syn led to a reduced neurotransmitter release and a smaller synaptic vesicle recycling-pool due to a reduced synaptic vesicle reclustering after endocytosis [165], with the consequence of impaired neurotransmission [166]. At this position, α-syn might act as a modulator of intersynaptic vesicle mobility to maintain recycling-pool homeostasis [167]. Overall, these studies suggest a physiological

role of α-syn to attenuate neurotransmitter release. However, late α-syn agglomeration during neurodevelopment and its sole expression in vertebrates does not concede an essential function for basic neurotransmitter release [168].

The exact mechanisms of the α-syn action on synaptic vesicle regulation are yet to be determined. As of now, many interaction partners with a neurotransmitter release function were found, though some of them might be responsible for the synaptic physiology of α-syn. One associated protein family of utmost importance in the neurotransmitter release cycle are the SNARE complexes. These proteins mediate the membrane fusion of synaptic vesicles and are, therefore, crucial for vesicle release and recycling. During SNARE complex assembly/disassembly in each neurotransmitter release cycle, the SNARE proteins are particularly vulnerable to degeneration. At this stage, α-syn acts as a molecular chaperone, assisting in SNARE complex assembly [169, 170]. Specifically, α-syn directly binds to the SNARE proteins synaptobrevin-2 and VAMP2, and assists the assembly through a nonenzymatic mechanism [171]. *In vitro* assembly was only possible with proteins reconstituted in plasma membrane mimics, thus cytosolic monomeric α-syn is not able to enhance the assembly, it requires the formation of a multimeric membrane-bound state [172, 173].

The chaperone function of α-syn has been reported in other cellular processes and is consistent with important chaperone qualities: i) α-syn is capable to interact with other intracellular proteins via the N-terminus; ii) it is structurally and functionally homologous to the 14-3-3 family of chaperone proteins [174]; and iii) the C-terminus of α-syn acts as a solubilizing domain based on the observation that it suppresses aggregation under chemical and thermal denaturing conditions [175].

α-Syn has been reported to bind to polyunsaturated fatty acids, suggesting a role in controlling the polyunsaturated fatty acid level in the brain. However, this is controversial because it is unlikely that α-syn acts as a carrier for fatty acids [176].

α-Syn may also be involved in suppression of apoptosis and may act as an antioxidant. By modulating nuclear factor-κB it indirectly acts on the protein kinase C δ levels, which is involved in apoptosis mechanisms [177]. Protein kinase C δ is oxidative stress sensitive, therefore, the antioxidant effect of α-syn has an impact on apoptosis too. Furthermore, dopaminergic neurons are particularly prone to oxidation of unsaturated phospholipids because they generate highly reactive dopamine. Only the monomeric form of α-syn can bind to lipid membranes in such a manner that it prevents lipid oxidation [178].

Another hypothesis suggests the involvement of α-syn in apoptosis not via antioxidant effects or protein kinase C, but via interaction with cytochrome c oxidase in mitochondrial membranes [179].

Generally, it is believed that the main physiological function is attributed to the localization of α-syn to presynaptic terminals. Subcellular localization also revealed substantial concentrations in nuclei, mitochondria, endoplasmatic reticulum, golgi, and red blood cells. At this locations, the functional significance remains unclear [168]. Whilst understanding the physiological role of α-syn does not directly lead to pathological effects in PD, it might be important therein.

1.3.5 Neurotoxicity

Since α-syn was found to be a main constituent of LBs it has become the most promising candidate to be involved in PD pathogenesis. The underlying molecular mechanisms related to toxic α-syn species and PD are poorly understood and highly controversial (Figure 7). In cases where one or more misfolded α-syn strains are the cause of PD, during the folding process of natively disordered monomers to multimers, and oligomers towards protofibrils, fibrils, and eventually LBs, there must be an α-syn species which has acquired neurotoxic properties. Therefore, it is crucial to investigate the mechanisms that lead to the initial misfolding, detect the toxic species, and understand their biomolecular action on neurons. In order to develop a neurotoxic effect, disease-responsible forms of α-syn need to spread over several brain regions to finally affect the brain in a neuropathological pattern. The theories behind the spreading of PD neuropathology are discussed in chapter 1.4.2 and 1.4.3. Independent of the species that might play the main role in the disease pathogenesis, all of them are in an equilibrium whereby higher order species are constantly built and disintegrated from a pool of endogenous α-syn. How these equilibria behave would be an interesting study but challenging due to problems in categorizing different species in a constantly moving ensemble.

Starting from monomers, overexpression of α-syn in mice led to increased neurotoxic effects [161, 180, 181] and outweighed the neuropathological alterations resulting from α-syn depletion [182, 183]. This correlates with the higher risk of developing PD in patients with SNCA gene multiplication [121, 184]. It does not necessarily indicate a possible pathogenic role of monomeric α-syn. It rather suggests that higher concentrations increase the likelihood of forming higher order α-syn complexes, in which toxic α-syn species might also be produced.

When assessing the toxicity of the monomeric, oligomeric, or fibrillary form of α-syn, either the *in vitro*-produced or *in vivo*-recovered α-syn species is often seeded into model systems to induce PD pathology. Under these physiological conditions, fibrillary α-syn forms have proven to be the only species capable of recruiting endogenous α-syn, and the cytotoxic potential was demonstrated [185]. The relevance of seeding capacity is subject of the 'α-syn spreading theories' (Chapter 1.4.2). Regarding the cytotoxic effects, there is some controversial evidence of toxic effects of fibrils, depending on the model system. In

animal experiments, inoculation of synthetic human α-syn fibrils into transgenic mice initiated LB pathology and reduced lifetime [186]. Importantly, this was observed for experiments with wild-type mice as well [187]. Even the brain homogenate of older transgenic mice with α-syn pathology had a pathology-accelerating effect upon inoculation in younger mice [186]. Fibrils were also isolated directly from PD patients brain homogenate, but there is no literature repeating those studies with control subjects [122].

However, as fibrils are an inert entity, they might have a sort of storage or clearance effect compared to the several types of metastable oligomers that exist during the assembly process [188]. Furthermore, some data suggest that fibrils cannot be efficiently formed without an air-water interface [189]. Thus, fully developed amyloid assemblies might play an important role in PD, but scientific opinion has been shifted to transient oligomeric species as being the important cytotoxic species [139, 190]. Still, recent findings have revealed fundamental differences of fibril polymorphisms with different levels of toxicity, which brings α-syn fibrils as disease-responsible candidate back to the discussion [140].

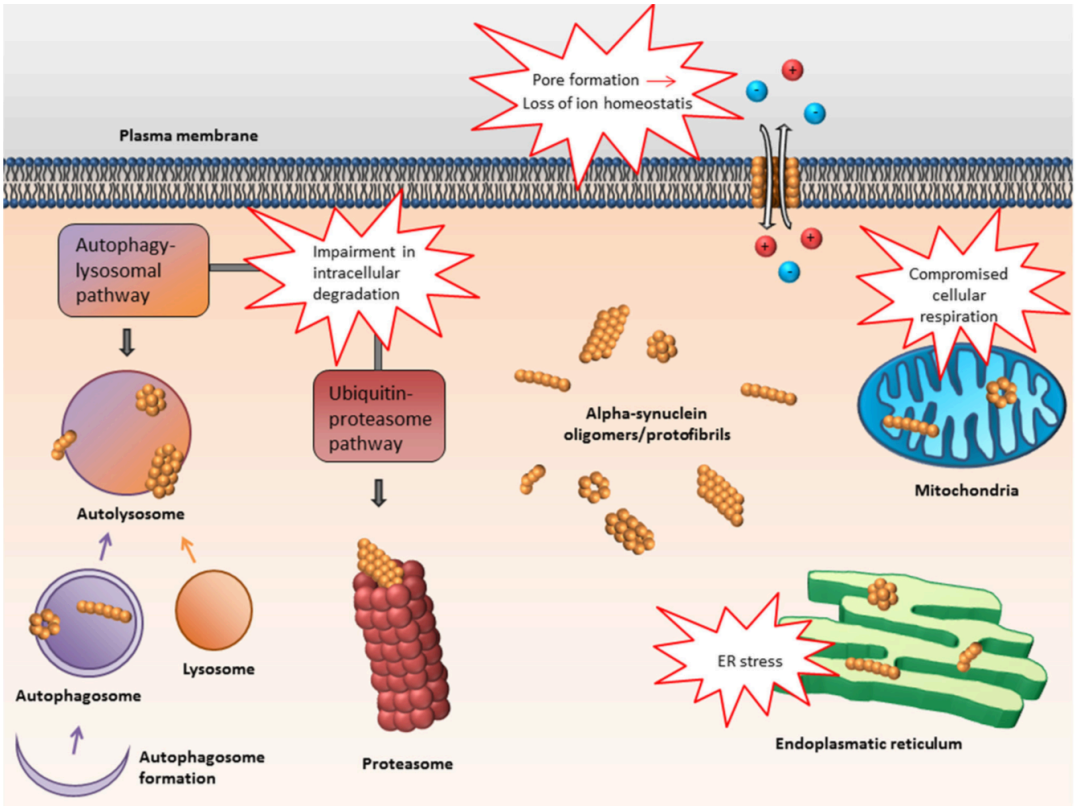

Figure 7. Possible toxic effects of α-syn. Reprinted with permission from ref [191]. Copyright (2016) Ingelsson Creative Commons License 4.0.

In vivo experiments with a rat lentiviral system demonstrated a significantly higher toxic effect of the oligomer-forming E35K and E57K α-syn mutants versus the human wild type form [137]. The loss of nigral tyroxine hydroxalse positive neurons was most striking for the oligomer-forming mutants but was not significantly higher compared to the fibril-forming E46K mutant. In cell-based systems, the E57K oligomer-forming mutation had the highest toxic effect. Besides the acute lentiviral expression of oligomer forming α-syn mutations, transgenic mouse models were developed where these mutations are chronically expressed throughout the brain. A chronic α-syn mutation E57K expression showed extensive synaptic and dendritic loss, and a reduction of synapsin 1 and synaptic vesicles [192].

In addition to a large number of studies on cellular and animal models, direct clinic-pathological observations in brains with LB pathology were made regarding the oligomeric α-syn species. Compared to healthy controls, increased levels of soluble α-syn oligomers with various sizes were detected [193, 194].

There are far more studies focusing on the toxicity of oligomeric species. Therefore, most proposed α-syn cytotoxic mechanisms are based on oligomer-mediated effects. Since several physiological functions of α-syn have been proposed, direct cytotoxic effects may arise by perturbing these natural functions. Specifically, it was speculated that altering the regulating role of α-syn in SNARE complex mediated processes leads to synaptic toxicity and impaired neuronal signaling. *In vitro* studies revealed that large α-syn oligomers efficiently inhibited SNARE complex mediated vesicle docking [195]. Extracellularly added α-syn oligomers, but not monomers and fibrils, displayed an impairment of long term potentiation in hippocampal brain slices of rats [196]. An increased synaptic transmission based on N-metyl-D-aspartate receptor activation was suggested to abolish the long term potentiation, since the effect could be avoided by blocking this glutamate receptor subtype.

Another toxic property of α-syn is thought to be a consequence of its ability to impair membrane integrity and permeability. On synthetic vesicles, protofibrils rather than fibrils or monomers were binding very tightly and permeabilized the membrane [197]. Further, the oligomer-prone mutants A30P and A53T have revealed greater permeabilizing ability than wild type α-syn [198]. Consequently, rupture of the lipid membrane can induce calcium influx into the cell and disrupt cellular ion homeostasis. In cell cultures, various oligomers were reported to induce cell death, presumably by forming a pore in the cell membrane [199]. This would be consistent with earlier studies where perturbed calcium homeostasis was suggested to be important in the pathogenesis of AD [200].

Intracellular degradation of α-syn is assigned to the autophagy-lysosome pathway and the ubiquitin-proteasome system. The first seems to be more important in the clearance of

oligomeric α-syn species, mainly by macroautophagy and chaperone-mediated autophagy [201]. Impairment of these systems could contribute to accumulation of misfolded α-syn due to weak clearance. Since the activity of both systems decline with normal ageing, the increasing level of α-syn in the SN is consistent with the reduced proteostasis activity [202]. In return, it was reported that the ubiquitin-proteasome system could be impaired by α-syn oligomers [203] and α-syn overexpression, or that different forms of α-syn inhibit both main mechanisms of the lysosomal autophagy system [204, 205]. Another study showed that accumulation of a α-syn reduced the lysosomal activity in dopaminergic cell models likely due to decreased hydrolase trafficking [206]. Thus, this vicious cycle where the degradation systems are inhibited by their target needs fewer initial toxic species to trigger a pathologic chain reaction. With respect to ageing – the widely accepted main risk factor – a progressive impairment of proteolytic mechanisms, which leads to an increasing aggregate accumulation in the ageing brain, might explain the higher risk of PD in older age and LB formation in otherwise neurologically healthy individuals.

Mitochondrial dysfunction by direct and indirect action of different forms of α-syn has been implicated as an important cytotoxic effect in the pathogenesis of PD. Furthermore, dopaminergic neurons are particularly sensitive to mitochondrial defects as they have a high-energy consumption and increased oxidative stress [207]. There is evidence from several *in vitro* studies to suggest that α-syn localize to mitochondria where it predominantly associates to the inner mitochondrial membrane [208, 209]. Consequently, increased mitochondrial dysfunction due to impaired complex I function was detected [210]. Overexpressed oligomer-forming α-syn A53T and A30P or overexpressed wild type α-syn in SH-SY neuroblastoma cells were aggregated and localized inside mitochondria [211]. The binding to mitochondria is concentration dependent. Simultaneously, decreased mitochondrial transmembrane potential, increased mitochondrial reactive oxygen species, and impaired cellular respiration was shown. In mice, overexpression of A53T α-syn in dopaminergic neurons led to a localization of monomeric and oligomeric α-syn to mitochondria, and increased mitophagy was detected along with impaired complex I function [212]. Morphological changes of mitochondria were observed in α-syn overexpressing SH-SY5Y cells. The increased expression caused the formation of α-syn oligomers which were suggested to be involved in the mitochondrial fragmentation [213]. Interestingly, the fission preceded any defective mitochondrial function [214]. Overall, it was shown in animal and cell models that α-syn oligomers, rather than monomers and fibrils, are able to elicit several mitochondrial phenotypes, including reduced complex I activity, reduced mitochondrial transmembrane potential, altered Ca^{2+} homeostasis, and enhanced cytochrome *c* release [215]. Overall, mitochondrial deficits, with or without α-syn toxicity, is recognized as a crucial pathogenic event in PD [216]. Besides natural age-related progressive mitochondrial dysfunction, the role of mitochondria in PD is

underlined by neurotoxins like methyl-4-phenyl1,2,3,6-tetrahydropyridine (MPTP) and rotenone, which can induce nearly identical symptoms to parkinsonism [217]. Additionally, several mitochondria-related gene mutations, including PINK1 and DJ-1 are associated with familial PD [70].

Endoplasmatic reticulum is another cell organelle that is involved in the cellular toxicity of α-syn. Accumulation of α-syn with toxic oligomer formation within the endoplasmatic reticulum has been demonstrated in mice overexpressing A53T α-syn mutants and in human brain with LB pathology [218]. The subsequent chronic stress and impaired protein quality control of the endoplasmatic reticulum may contribute to PD pathology. Medication with an endoplasmatic reticulum stress inhibitor reduced levels of oligomers in mouse endoplasmatic reticulum and [218] reduced microsomal accumulation of both monomeric and oligomeric α-syn [219]. Furthermore, only oligomeric α-syn but not monomeric or fibrillar α-syn was efficiently able to induce the endoplasmatic reticulum response factor x-box binding protein 1 [220].

Inducing a neuroinflammatory response of glia cells might be a further mechanism in α-syn neurotoxicity. While physiologically working astrocytes and microglia participate in clearance of pathologically active protein aggregates, upon contact with α-syn aggregates they have a pro-inflammatory effect and cause inflammation and enhanced neurodegeneration [221, 222]. Although there are reports that fibrillar α-syn species lead to a stronger inflammatory response [223], several *in vivo* and *in vitro* studies showed enhanced oligomer-induced inflammatory signals in microglia [224-226]. It was proposed that the phagocytosis of oligomers leads to the activation of NADPH oxidase and production of reactive oxygen species [224]. Another report showed that MAP kinase inhibitors could prevent the oligomer-induced microglia activation and attenuated the neuronal loss in rats [225]. Altogether, several studies suggest that mostly α-syn oligomers could develop toxic effects and enhance inflammatory responses by microglia activation.

Overall, several mechanisms for fibrillar and oligomeric α-syn-induced neurodegeneration were suggested, and oligomers are the most convincing candidates for being responsible for several damaging effects, and thus a possible target for a therapeutic interventions [191].

1.4 Synucleinopathies

Synucleinopathies is an umbrella term for all neurodegenerative conditions with a pathological LB characteristic. As it is not known to what extent α-syn pathology is involved in the mechanisms of the individual diseases and α-syn pathology also occurs in neurologically healthy individuals, this term might have little practical value in diagnostics. Still, pathological similarities raise hopes of transferring scientific findings

among the conditions and eventually making use of one potential pharmaceutical treatment in several α-syn related diseases. The three main synucleinopathies are sporadic PD, DLB, and multi system atrophy (MSA). However, AD was the first identified and likely the most frequent neurodegenerative disorder with α-syn-containing deposits in patients [113]. Additionally, pathologic α-syn accumulations have been found in several other rare ND, including neurodegeneration with brain iron accumulation 1 (formerly Hallervorden-Spatz syndrome) [227, 228], amyotrophic lateral sclerosis (ALS) [229], Parkinsonism-dementia complex of Guam [230], frontotemporal dementia [231], Pick disease [232], diffuse LB disease [233], pure autonomic failure [234], progressive supranuclear palsy [235], Krabbe disease [236] and corticobasal degeneration [237]. It is unclear whether synucleinopathies share a common pathogenic mechanism or if there is a mutual relationship with a common final pathology [238].

1.4.1 Lewy Pathology

The function of LBs is not understood. Most studies view LBs as neurotoxic, whereas some theories attribute a certain neuroprotective function by clearing cytotoxic α-syn species from neurons [37, 188]. Since Lewy pathology occurs in many diseases, mostly not in consistent patterns, and 10% of neurologically normal individuals over 60 years are affected [239], the relevance of these abnormal deposits are often questioned. Furthermore, the severity of the Lewy pathology often does not correlate with the disease progression [240] and patients with parkin gene mutations or the LRRK2 G2109S mutation often do not show any LB formation [46].

To understand the pathological function of LBs, the formation process and exact structure is crucial. Although the molecular composition was determined, LBs could not be generated artificially and there is only speculation about the formation mechanism. The ultrastructure of LBs was determined in 1965 and remains the primary described structure to date [35]. This study revealed that LBs are not confined circular bodies with a densely packed core surrounded by radiating filaments. This was confirmed later and two different types of LBs were proposed, a common classical type and a second cortical type without a dense core but mainly composed of circular fibrils [32]. Later, dense core vesicles were described as being located in the vicinity of LBs [241].

However, recent findings suggest a different structure, in which the LB contains a crowded mass of membranes from vesicles, deformed mitochondria, and disrupted cytoskeletal elements [242]. In contrast to all the other studies, no filamentous structures were observed, mitochondria were most frequently found in the periphery and the vesicular structures were detected in the center of the LBs. Based on these findings, a five-step model of LB formation was proposed with the conclusion that impaired trafficking of organelles is a key driver of PD pathogenesis [242]. These results are currently still under

review and have not yet been replicated. Thus, further research is needed to understand the nature and the role of LBs in synucleinopathies. Support for these findings could be provided by a recently developed transgenic mouse model [243]. By inactivation of constitutive autophagy in dopaminergic neurons, LB formation was induced, which contained many mitochondria.

1.4.2 Prion-like Spreading

The Braak staging proposed a characteristic spatiotemporal spreading pattern of Lewy pathology between interconnected regions in the PNS and CNS in PD patients [244]. Additionally, spreading of the host pathology onto grafted neurons in PD-affected brains was discovered [110, 111]. These neuropathological findings suggested a spread of Lewy pathology in a prion-like manner [245]. This prion hypothesis has been supported by a growing number of studies, which show the necessary steps for α-syn to spread along neuronal projections, being internalized and released by neurons, and recruiting endogenous α-syn to misfold [246].

The prion-like spreading theory presumes an initial misfolding of α-syn to trigger the disease. The subsequent toxic function of oligomer and fibril species has been discussed in chapter 1.3.5. Although oligomer and fibril formation is reproducible *in vitro*, the initial formation in the nervous system remains elusive, especially since an air-water interface is required for the aggregation [189]. It is assumed that normal stochastic misfolding and failing quality control mechanisms can result in a meta stable species that starts the spreading. Thus, high local α-syn concentrations due to relative overproduction may favor such an equilibrium shift from monomeric to oligomeric species [247], or certain mutations could increase the stability of α-syn in an oligomeric state [139]. Impaired proteolytic defense mechanisms, which normally degrade protein accumulations, and certain vulnerable neuronal populations may also play an important role in the initial triggering of α-syn accumulation and aggregation [248]. To assess the other elements of protein spreading, specifically axonal transport, uptake and release by neurons, and accumulation of endogenous α-syn, a list of experiments have been done in cell cultures and *in vivo*.

1.4.2.1 Transport

The relatively long distances between the typical LB-affected brain regions makes axonal transport likely to be involved in the spreading of PD pathology. Experiments with neuronal cell culture systems showed both retrograde and anterograde transport of preformed oligomeric [249] and fibrillar α-syn [250], with transport in retrograde direction being more efficient [251]. Although transport velocity in the anterograde direction is similar to fast axonal transport, it was suggested that α-syn aggregates are transported by

the axonal slow component b transport due to observed characteristic pauses. Additionally, α-syn fibrils might share features with the slow component b cargo [250]. Axonal transport of preformed aggregates from an initial neuron to second and third order neurons was observed and aggregation of endogenous α-syn was induced in the new cellular hosts [252, 253]. Thus, initial misfolded α-syn has the potential to progressively spread and induce Lewy pathology in distant regions, which is consistent with the Braak staging.

Cell-to-cell transmission of α-syn aggregates was shown in several *in vivo* experiments. Wild type and α-syn transgenic mice injected with preformed fibrils or fibrils isolated from PD brain homogenate of transgenic mice showed endogenous α-syn aggregate formation at the injection site and in axonal retrograde and anterograde connected brain regions [186, 187]. Similarly, the intracerebral inoculation of isolated α-syn derived from DLB and PD patient brains induced α-syn pathology in monkeys and wild-type mice [254, 255].

Overall, axonal transport was shown in cell culture systems and animal experiments with intrastriatal pathogenic α-syn injection, which suggests a disease progression that is consistent with the Braak spreading. Still, the involved cellular mechanisms are largely unknown.

Besides axonal transport, a direct cell-to-cell transfer of α-syn assemblies over short distances was hypothesized, since transmission via tunneling nanotubes was already demonstrated for the scrapie prion protein [256]. Recent findings confirmed the spreading of fibrillar α-syn in co-cultured neurons through tunneling nanotubes [257]. Importantly, this transport was also demonstrated between non-neuronal cell types, which would ease the transfer throughout the brain [258]. The transfer of the aggregates from the initial cell happened inside lysosomal vesicles. The recipient cell showed clear signs of seed fibrillization of endogenous α-syn. These findings suggest a new role for lysosomes in the spreading of α-syn assemblies.

1.4.2.2 Release

In cell culture based experiments axonal transport of preformed fibrils from an initial cell population up to a third order population was observed [252]. Consequently, an uptake and release must have happened in order to spread the aggregation. Importantly, α-syn monoclonal antibodies reduced spreading *in vivo* and *in vitro* by inhibiting aggregate uptake and, therefore, cell-to-cell transmission [252]. Since antibodies have access to the preformed fibrils, they are not being secreted in vesicles.

In vitro, soluble forms of α-syn may be secreted by non-classical endoplasmatic reticulum independent vesicle-mediated exocytosis [259, 260]. Whether the same pathway mediates the release of aggregated α-syn is not clear. Recently, involvement of ubiquitin-specific

peptidase 19 and DnaJ/Hsc70 pathways in the release of α-syn was demonstrated [261, 262]. Both chaperone-mediated pathways secrete their cargo in a non-encapsulated form. Furthermore, release of fibrils after retrograde and anterograde transport is likely to be independent of cell lysis, as observed in primary cell cultures [251]. Overall, a non-conventional secretion of α-syn assemblies seems likely.

Exosomes might also participate in bridging the extracellular space during cell-to-cell transfer. However, exosomal release of fibrillar α-syn has not been demonstrated yet [246]. In general, the amount of endogenous α-syn secreted in exosomes is significantly lower than α-syn secreted by exocytosis [263, 264]. Other α-syn assemblies, like smaller oligomeric species, may still participate in the release via exosomes.

Additionally, the transfer from cell-to-cell through tunneling nanotubes was shown, which makes the release of toxic α-syn into the extracellular space obsolete [257]. Although this type of transfer is believed to be highly efficient, it remains unclear to what extent it participates in the spreading of α-syn.

1.4.2.3 Uptake

The uptake of preformed aggregates from the cell media is a rapid process in cell culture systems. It was reported that after 16 hours incubation of cells with a fibril concentration of 0.5 and 1 μM the uptake efficiency of the cells was 75 and 100 %, respectively [257]. In general, incubation for 1 hour *in vitro* for seed uptake was sufficient [265]. When α-syn fibrils were injected in mouse brains, they were found in neurons and glia cells close to the site of injection within a few hours [266]. Aggregates were taken up in cell soma, dendrites, and axons, explaining the transport in axonally retrograde and anterograde connected brain regions [250, 252, 253]. There are various reasons for the conflicting uptake concentrations and kinetics reported. Different cell culture types and conditions could influence the ability of the cell model to internalize the protein aggregates. Furthermore, α-syn oligomer and fibril formation could have been conducted under different conditions, and prolonged sonication time and power to fragment the fibrils could have produced different seeds. Especially, *in vitro*-prepared fibrils can be influenced by many conditions, including type of buffer, temperature, and concentrations, leading to different fibrillary strains, which might have different spreading properties [140, 267, 268].

It is likely that uptake of α-syn aggregates follows endocytic pathways, based on the observation that reduced uptake was found when endocytosis was inhibited by low temperatures or blocking of dynamin 1 [259]. Marking endosomal trafficking against early endosome proteins EEA1 and Rab5, and late endosomal markers Rab5 and LAMP1, revealed that internalized proteins merged in early and late endosomes and in lysosomes [269-272]. For most internalized aggregates, lysosomal degradation happens within hours,

but conflicting reports suffer from similar experimental heterogeneity as for the reported uptake kinetics. How the remaining α-syn aggregates escape from the endosomal compartment before degradation is not known. However, the surrounding lipid membranes prevent access to endogenous α-syn, which is required to comply with the prion-like theory.

Several cell surface proteins that can interact with α-syn were identified. Heparan sulfate proteoglycans (HSPG) is a potential binding partner for neurodegenerative hallmark proteins, including scrapie prion protein [273, 274], α-syn, and misfolded tau. [275]. HSPG initial interaction might be of non-specific electrostatic nature. Still, heparin can competitively inhibit internalization of α-syn fibrils [275]. Interestingly, internalization of larger α-syn amyloid aggregates but not non-amyloid oligomers is dependent on HSPG [276].

Recently, lymphocyte-activation gene 3 (LAG3), neurexin 1β and APLP1 were recognized as cell surface partners for α-syn preformed fibrils [277]. LAG3 most selectively bound to fibrils and co-endocytosed in cortical neuron cultures. Overexpression of LAG3 increased the uptake of fibrillary α-syn whereas knockdown of LAG3 prevented α-syn pathology. Similarly, internalization could competitively be blocked by LAG3-specific antibodies [277].

In addition to HSPG and LAG3, the a3-subunit of Na^+/K^+-ATPase (NKA) was identified as a potential binding partner for α-syn aggregates [278]. Similar to LAG3, NKA specifically interacts with α-syn fibrils but not with monomers. The authors demonstrated that NKA got trapped within clusters of α-syn assemblies on the cell membrane. This compromised the Na^+ gradient in cultured neurons and may affect the relation with several other interaction partners.

1.4.3 Neuronal Selective-Vulnerability

With the increasing popularity of the α-syn pathogenic spread theory, there is also a growing resistance against the simplicity of the “prion-like” spreading mechanisms [55]. The principal alternative is a concept based on cell-autonomous factors which make certain neurons intrinsically more vulnerable to PD pathogenic processes. This older concept of selective neuronal vulnerability mainly conflicts with the oversimplification of non-cell-autonomous mechanisms of the pathogenic spreading.

Although the prion hypothesis provides an explanation for the progressive spreading pattern in PD brains, it fails to explain the observed staging of the Lewy pathology, on which the Braak stages are based. Besides that, the Lewy pathology cannot completely be correlated to all clinical states [53]. The idea of inter-neuron LB spread through the brain, driven by endogenous α-syn recruitment, cannot explain different spreading patterns and

affection of non-connected areas. The selective vulnerability hypothesis suggests cell-autonomous mechanisms that drive the Lewy pathology and neuronal death; α-syn itself is not seen as a propagating pathogen [279]. To date, little is known about the selective cell death of similar neurons within the same brain regions [63]. However, a vulnerable neuron, which is susceptible to PD-associated factors like age, environmental toxins, mutations, and oxidative stress, is possibley also more vulnerable to α-syn pathology, including the pathogenic spreading. Albeit the prion hypothesis is simple and has its shortcomings, it can be combined with the selective vulnerability theory, which would explain a lot of the pathology in PD [280].

1.4.4 Strain Dependence

Regarding α-syn as main pathological driver in synucleinopathies, basic differences in their pathology might be explained with different "strains" of toxic α-syn adopting different structural conformations [281]. It was hypothesized that the assemblies themselves, rather than the process of formation and spreading, may cause the toxic effects. Consequently, one protein but different strains could explain the various outcomes in different synucleinopathies. Additionally, the pattern of Lewy pathology, which can eventually be linked to clinical symptoms, can vary in different cases of the same disease. The reasons underlying these distinct clinical and pathological phenotypes within one disease remain unclear but might also be explained by the "strain hypothesis". Recently, this hypothesis was supported with the characterization of two different α-syn assemblies [140]. These two α-syn polymorphs, fibrils and ribbons, had different levels of toxicity and showed different propagation properties in cell cultures. Following these findings, the same fibrils and ribbons were injected to the SN of rats [282]. It was shown that fibrils appear to be the major toxic strain, having a higher potential for degenerating dopaminergic neurons and causing motor deficits. In contrast, ribbons caused more deposition of α-syn in the brain. Furthermore, intravenous systemic administration of the same strains crossed the BBB. In the brain, ribbons but not fibrils led to the generation of glial cytoplasmic inclusions.

Additionally, α-syn strains were discovered that showed different efficiencies in cross-seeding tau aggregation [267]. Not only neuronal cell cultures but also α-syn inoculated mice showed signs of differentially induced tau pathology, depending on the α-syn strains.

Overall, fibrillar α-syn polymorphisms were demonstrated to have different efficacies in the recruitment of endogenous α-syn as well as in their ability to promote tau inclusions. They exhibited different toxicities, binding efficiencies, and penetration efficiencies in cell cultures [185].

1.5 Cell Culture Models for Parkinson's Disease

The field of PD has been struggling for a long time to find a disease-relevant animal model system that presents all the cardinal symptoms of PD. The multitude of the established animal models are rodent models, which only partially recapitulate the pathological features observed in humans. The growing importance of non-motor signs in PD patients is only poorly described in rodent models [283]. To study a single PD feature, cell culture models are an important alternative to animal models. Defined cell types in homogeneous isolation offers the advantage of studying specific cellular processes, which appear to have an important contribution to a disease, as it is the case for dopaminergic neurons in PD. Regarding our limited understanding of α-syn-mediated toxicity, it is important to investigate the cytotoxic mechanisms by reproducing the main aspect of disease spreading, including uptake, release, transport, and seeded aggregation of α-syn on easy cellular models. Since neither animal nor cellular models are able to fully recapitulate PD, dissecting the overall processes in simple molecular events is important to identify the main players in this disease [284]. However, the pathogenesis of a disease requires the interaction of several cell types, which to a certain degree can be established in cell culture systems but often can only be studied in animal models.

Besides restricting the number of animal experiments for ethical reasons, cellular models offer several advantages: (i) easy access to genetic modifications for pharmacological testing; (ii) accessibility to imaging and biochemical analysis; (iii) experimental upscaling and high-throughput screening for pharmacological candidates and disease conditions [285]. Primary cell cultures only partially share these advantages, since they are derived from rat or mouse embryos and have a finite life span. This excludes their use in high-throughput experiments and ethical questions still arise. Additionally, heterogeneous cell populations and differences among preparations are major drawbacks.

The development of differentiated dopaminergic cell models is of particular interest in PD research. Although other types of neuronal cells in PD brains are known to degenerate, these cells are particularly vulnerable. Thus, the importance of dopamine depletion and motor-symptoms in PD puts dopaminergic neurons in the focus of many studies. Primary neuron cultures yield less than 10% dopaminergic neurons, whereas immortalized cell lines display the full range of advantages of cellular models and can present monocultures of dopaminergic neurons [285, 286]. Immortalized cell lines are generally easy to maintain with minimal equipment and their rapid proliferation makes them accessible to large scale studies [287]. In contrast to primary cell cultures, they can also originate from humans.

In PD, several immortalized cell lines from human and mouse have been used, mainly HEK293, H4, SH-SY5Y, PC12, and LUHMES cells [284]. Although HEK293 cells do not have a dopaminergic phenotype [284], they are frequently used to study α-syn aggregation,

secretion, and transmission, since they are suitable for large scale screening and easy to cultivate [288, 289].

The human neuroblastoma cell line SH-SY5Y can develop dopaminergic neuron-like properties upon differentiation with retinoic acid [290]. They are easy to maintain which makes them suitable for large screening studies, but differentiation can be difficult and the cell response can be inconsistent [291]. Since the differentiated cells can exhibit dopaminergic, cholinergic, and noradrenergic phenotypes using various differentiation protocols, they are not considered as authentic dopaminergic neurons [292].

PC12 are another frequently used cell line in PD research. The cells from a pheochromocytoma of the rat adrenal medulla can be differentiated towards a neuron-like phenotype. They are often used to study PD toxins since they are susceptible to 6-OHDA, MPP+, rotenone, and paraquat [284].

Besides these cell lines and primary cell cultures, the development of hESC and iPSC have a great potential to model human diseases *in vitro*. Especially the fast progression in iPSC differentiation to midbrain dopaminergic neurons will be of great use as a PD model system [293, 294]. As they are generated from adult cells, they circumvent the ethical issues of hESC [295]. Additionally, sporadic and familial PD iPSC lines can be generated from PD patients, which makes them a unique model system [296]. However, differentiation to mature neurons is cost- and time-intensive and can result in heterogeneous populations. Future developments in iPSC technology will provide the PD field with a wide range of options to perform *in vitro* studies. For now, easily accessible, stable, and homogeneous cell cultures, as provided by immortalized cell lines, are still required.

1.5.1 LUHMES Cell Line

Lund human mesencephalic cells (LUHMES) are a subclone of MESC2.10 cells, which were generated from ventral mesencephalic tissue of an 8-week-old human fetus [297]. MESC2.10 were immortalized by transformation with a LINX-v-myc retroviral vector. The v-myc oncogene overexpression can be controlled with tetracycline. Thus, overexpression and proliferation of the cells can be stopped with tetracycline, resulting in a shut-down of the myc transgene and subsequent formation of post-mitotic neurons [298]. The addition of tetracycline, glial cell derived neurotrophic factor (GDNF), and cAMP promotes the morphological differentiation to dopaminergic neurons [297]. However, the MESC2.10 cell line was reported to show an unstable and heterogeneous TH expression [299]. Its subclone, the LUHMES cell line, features a similar behaviour compared to primary cell cultures when exposed to PD toxins and a more stable dopaminergic phenotype is achieved [300].

With an optimized differentiation protocol, LUHMES cells became a suitable homogeneous cell line, with comprehensive characteristics with respect to morphology, neurite outgrowth, expression of neuronal markers, and electrophysiology [301, 302]. A strong dopaminergic phenotype with high TH levels, dopamine release, and synaptic marker expression that reaches its maximum after five days of differentiation was reported. Differentiated LUHMES cells appear to be highly sensitive to PD toxins, which has been exploited in several studies [303].

However, LUHMES cells cannot be regarded as completely differentiated neurons due to co-expression of several mature and precursor dopaminergic neuronal markers at all stages [301]. Additionally, conflicting results about heterogeneous expression of TH were reported [304].

Some efforts are required to perform genetic modification in LUHMES cells since classical transfection techniques have proven to be inefficient. Generally, lentiviral gene transfer in the proliferating state are used to perform experiments with the cells in differentiated states [305]. With this technique, several stable LUHMES models were developed, including models to study α-syn aggregation and models to study mitochondria motility [305, 306].

Recently, a co-culture model of LUHMES cells and astrocytes was developed to address functional questions of glia cells in neuropharmacological studies [307]. This new model should also enable studies on the astrocytes neuroprotective properties and on glia-cell derived neurodegenerative factors [308].

Supplemental to the standard adherent cultures, neurosphere formation and three-dimensional cultivation of LUHMES cells was studied [309, 310]. With a slightly adapted differentiation protocols, this model allows the differentiation of LUHMES cells for more than 20 days, which allows long-term experiments with the advantages of the standard LUHMES cells.

Microfluidic devices offer great advantages in cell cultivation, for example to study axonal transport of proteins. Although the cultivation of LUHMES cells in microfluidic devices has been mentioned in the literature, no such results were published to date [284, 311]. It is assumed that the cultivation of LUHMES cells is unstable in microfluidics and full maturity of the cells cannot be reached [312].

1.6 Microfluidic Cell Culture

Since the development of cell culturing, the basic techniques have not changed [313]. The introduction of robotics has improved accuracy and increased throughput to allow large scale screening with minimal cell numbers, which became the last revolution in cell culture

technology. In the last few years, microfluidics allowed miniaturization of cell cultures down to a single cell level in devices with precisely defined geometries, substrates, and flow. Together with automatic manipulation and analysis this technology cleared the way for a biological lab-on-a-chip.

Cultivating with microfluidics offers several advantages. Small volumes can be precisely regulated down to the fL-range and can be automated to a great extent [314]. This provides a highly-controlled environment for cell cultures without the need for manual intervention. This increases the reproducibility, which is important when high parallelization on a single chip performs a multitude of individually controlled experiments. Screening many conditions simultaneously with a single batch of cells improves consistency among assays. This high-throughput and controlled way of culturing is of great use, especially for demanding cell lines [315].

Soft lithography of polydimethylsiloxane (PDMS) has become a standard technique for the manufacturing of microfluidic cell culture devices. It allows the integration of micromechanical valves, channels and assay chambers in compact devices. For optical analysis, PDMS offers the great advantages of being transparent with low levels of auto-fluorescence and only containing small enclosed volumes. These excellent imaging properties and the high degree of control renders PDMS microfluidics ideal for live cell imaging.

However, there are several issues that need to be addressed when working with cell cultures in PDMS microfluidics. Very often, revisions of the cell culture protocols are needed. Care must be taken in the production of PDMS devices, since improperly cured, non-cross-linked polymers might change the experimental conditions [316]. PDMS has very high gas permeability, which also can result in evaporation of cell media from the devices or can induce a different pH behavior compared to macroscale culturing. The small volumes in microfluidic devices compared to standard culturing dishes could also lead to different conditions, since consumption of nutrients and increase of waste products happens rapidly. Thus, a more frequent exchange of media is needed. Additionally, PDMS absorbs hydrophobic molecules, which complicates the evaluation of liquid content especially at these small volumes. Thus, the media composition may need to be adjusted [317]. Another important factor that needs to be considered in microfluidic devices is liquid flow, which can alter the growth of the cells and can induce shear stress, altering the outcome of the experiments [318].

A growing number of studies use microfluidic devices to culture neuronal cells and physically separate cell bodies from their axonal projections [250-253, 277, 319]. The fluidically isolated compartments ensure that transfer can only happen intracellularly through neurites, independent from flow and diffusion in cell media. Several of these

devices are commercially available. Studying intraneuronal transport, these devices can provide direct evidence that extracellularly-added peptides are taken up by soma or axons and transported in anterograde or retrograde direction respectively. The excellent optical properties of PDMS are ideal to monitor cell cultures and track fluorescently labeled protein assemblies using live cell light microscopy.

CHAPTER 2

Dopaminergic Neuronal Model for Spreading of Fibrillar α-Synuclein in Parkinson's Using LUHMES Cells

This chapter describes the development of a microfluidic device to co-culture fluidically isolated LUHMES cell populations for seeding experiments. Furthermore, LUHMES cells were evaluated for their use as a model in the prion-like spreading hypothesis of PD. This chapter is being prepared for submission.

A. Bieri[1], R. Sütterlin[1], H. Stahlberg[1], T. Braun[1*]

1 Center for Cellular Imaging and NanoAnalytics (C-CINA), Biozentrum, University of Basel, Basel 4056, Switzerland

* Corresponding author: thomas.braun@unibas.ch

Abstract

We present a dopaminergic model system to study the prion-like cell-to-cell spreading of α-synuclein (α-syn) by combining Lund human mesencephalic (LUHMES) cell cultures with microfluidics, separating two cell populations only allowing neurite interactions.

Aggregation of α-syn is a hallmark of Parkinson's disease (PD). A prion-like spreading mechanism from one to the next cell could explain the stereotypic distribution of the protein aggregation in the brains of patients. The mechanisms underlying the long range axonal transport of α-syn aggregates and the cell-to-cell migration might be a key element in understanding the progression of PD. Unfortunately, *in situ* studies on a molecular and structural level are limited in patients, and model systems must be used. Cellular culture systems that allow spatial separation of cell bodies and neurites are of great use. We developed microfluidic chips and cell-culturing protocols to spatially control the cell growth and separate different populations of LUHMES cells, which can be differentiated to dopaminergic, neuron-like cells. We show that this combination of microfluidics and LUHMES cells can be used for direct observation of axonal transport of α-syn aggregates. The individual handling of cell populations without cross-contamination of testing agents

is possible. We observed that LUHMES cells transport α-syn fibrils with low efficiency in anterograde and retrograde directions.

2.1 Introduction

The loss of dopaminergic neurons in the substantia nigra is characteristic of PD. The symptomatic occurrence of aggregated α-syn, the putative main constituent of the so-called Lewy bodies and Lewy neurites [33], suggests this protein plays a major role in PD. When Braak and colleagues reported a stereotypic spreading of the Lewy pathology in PD [47], α-syn itself was found to be a potentially infectious neurotropic protein. First evidence emerged from grafted fetal neurons implanted into the forebrain of PD patients for therapeutic reasons. These neurons also showed a Lewy body-like pathology in post-mortem analysis several years after implantation [110, 111]. These observations combined with the Braak model of PD led to the "prion-like" spreading hypothesis, which is now a firmly established model for the disease progression of PD [320]. Although this theory is still controversial discussed [55], uptake, template misfolding, and cell-to-cell transmission has been shown for preformed α-syn fibrils in several *in vivo* and *in vitro* studies [253, 319, 321]. To understand the mechanisms of prion-like PD progression it is essential to know how α-syn is transmitted from one cell to another. Transfer of aggregates is possible through extracellular space or by direct cell-to-cell contact. The first may involve active secretion strategies like exocytosis [260, 263], or passive processes by releasing naked protein aggregates to the culture media from intact and dead cells [322]. A release-independent mechanism was reported where tunneling nanotubes mediate the transmission of aggregates from cell-to-cell. [257]. However, typical spatial distributions of Lewy bodies between axonally interconnected regions in the PNS and CNS suggest a long range axonal spread of α-syn. It has been shown in mice that injected α-syn fibrils induce endogenous α-syn to aggregate, even at a distant region from the injection site [255]. In cell cultures, several groups reported the transmission of exogenously-added, preformed α-syn fibrils and oligomers along axonal projections in both anterograde and retrograde directions [250, 251, 253]. From axons, α-syn aggregates likely are not transferred in direct contact but secreted into the media independent of axonal lysis [251].

Microfluidic chambers are a useful tool to address the questions of neuron-to-neuron transmission [323]. To study axonal transport, cell populations are spatially separated by microchannels in such a way that only axonal projection can establish contacts between cells. A controlled media flow prevents transport other than through axons. In these studies primary cell cultures are mostly used [250-252, 324, 325]. These are only available with low yield, are not of human origin, and long differentiation times make large-scale experiments difficult. Other neuronal models are available more easily, such as PC12 rat

cells and SH-SY5Y neuroblastoma cell line. Unfortunately, they suffer from interspecies differences or are difficult to differentiate into post-mitotic neurons [285]. Therefore, the LUHMES cell line is a promising alternative [286, 298]. More easily available, homogeneous, and rapidly to differentiate, they play an increasing role in PD research [284]. Despite their use in neurotoxic screening and further development as a 3D model in neurospheres [309, 310], LUHMES cells were never cultivated in microfluidic devices to study α-syn spreading. Most likely this is due to poor growth in microfluidic devices or resistance against neurite guidance through the devices's connecting parts.

In this study, we developed a cellular tissue model system allowing large-scale experiments with homogeneously differentiated dopaminergic LUHMES cells. We designed a microfluidic device to create a viable environment for this cell type with two connected but flow-separated growth chambers. As a result, LUHMES cells can easily be made available for high throughput experiments with two isolated cell populations, e.g. for the testing of axonal transport upon α-syn aggregate incubation, or for toxin testing. Using this system, we tested the α-syn uptake and cell-to-cell transfer in LUHMES cells.

2.2 Results

An *in vitro* model system for the prion-like spreading of α-syn through neurites requires at least two components: firstly, a device (chip) that mechanically separates the two cell populations and restricts the interactions of the cells between their neurites, and, secondly, a dopaminergic cell culture growing in the chip.

2.2.1 Chip Design and Fabrication

The design principles of the microfluidic chip for the compartmented cultivation of neuronal cells are depicted in Figure 8A and are adapted from Dinh et al. [311]. Two cell growth chambers with a height of 30 µm are oriented towards a "communication region", exhibiting small channels with a reduced height (~3 µm width, ~4 µm height) perpendicular to the growth compartments, solely allowing neurite outgrowth. Additionally, a central channel (80 µm width, 30 µm height) divides the communication region (Figure 8C 6). The chip exhibits three main channels, two supporting the cell growth compartment and a central channel crossing the "communication region." Every channel consists of an inlet reservoir, an outlet reservoir, and a channel restriction to reduce the flow rate. Note that the flow rate of the central channel is higher to produce an underpressure in the central channel relative to the cell chambers. We used soft lithography and replica molding for the PDMS chip production.

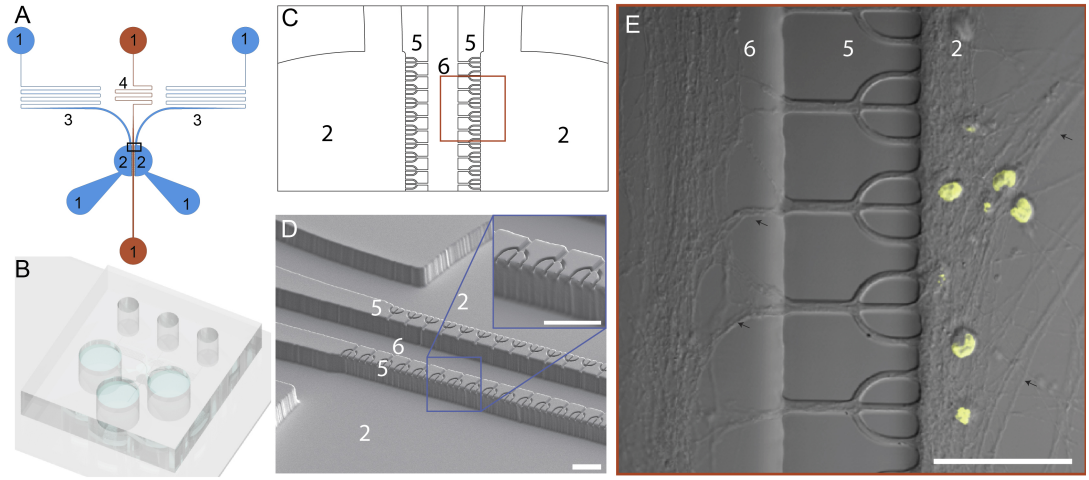

Figure 8. Design of the microfluidics for the minimalistic tissue. (A) The arrangement of the individual chip components. Three independent channels each exhibit an inlet and outlet port (1). Two cell culturing chambers (2, blue) are symmetrically arranged towards a central channel (red). The cell culturing channels and central channel are separated by microchannels (not visible). All three main channels exhibit a flow which is controlled by resistive channels (3, 4). The flow in the central channel is higher since the restriction (4) is shorter. (B) Microfluidic chip bonded onto a glass plate, showing the channel ports (rendered image). (C) Details of the microchannels (5). The microchannels are arranged perpendicular to the cell growth chambers (2) and the central channel (6). (D) SEM of the microchannel region. Note the cell growth chamber (2) and the central channel have a height of approximately 30 µm, but the microchannels exhibit only a height of 4 µm, preventing the passage of the cell somas and only permitting the outgrowth of neurites. The inset shows the indicated region at higher magnification. (E) DIC image of LUHMES cells differentiated for 10 days. Nuclei DNA is stained by the DAPI fluorescence dye (yellow) in the cell growth chamber (2). Black arrows indicate some dendrites. Note the absence of nuclei in the central channel (6), demonstrating the specific permissibility of dendrite outgrowth through the microchannel region (5). Scale bars 50 µm.

2.2.2 Flow Behavior and In-Chip Isolation of Fluidic Compartments

The flow behavior of the chip was tested using fluorescent dyes (Figure 9). The hydrostatic pressure difference between the inlet and outlet port drives the buffer exchange of the cell media in the growth chamber, and after approximately 10 min upon filling the inlet port, the entire growth-media is replaced (Figure 9). After 24h the pressure difference between the inlet and outlet port drops to 0, the flow stops, and buffer exchange only happens by diffusion. By emptying the outlet ports every 24 h the buffer flow in the cell culture chamber and the central channel is maintained. Additionally, water evaporation must be considered to maintain a healthy growth environment in the microfluidic chip. The inlet ports ran dry within three days despite being stored in humidified cell incubators. Therefore, the chips were placed in a Petri dish along with two stripes of wet filter papers. In this condition cells can survive for three days without media change.

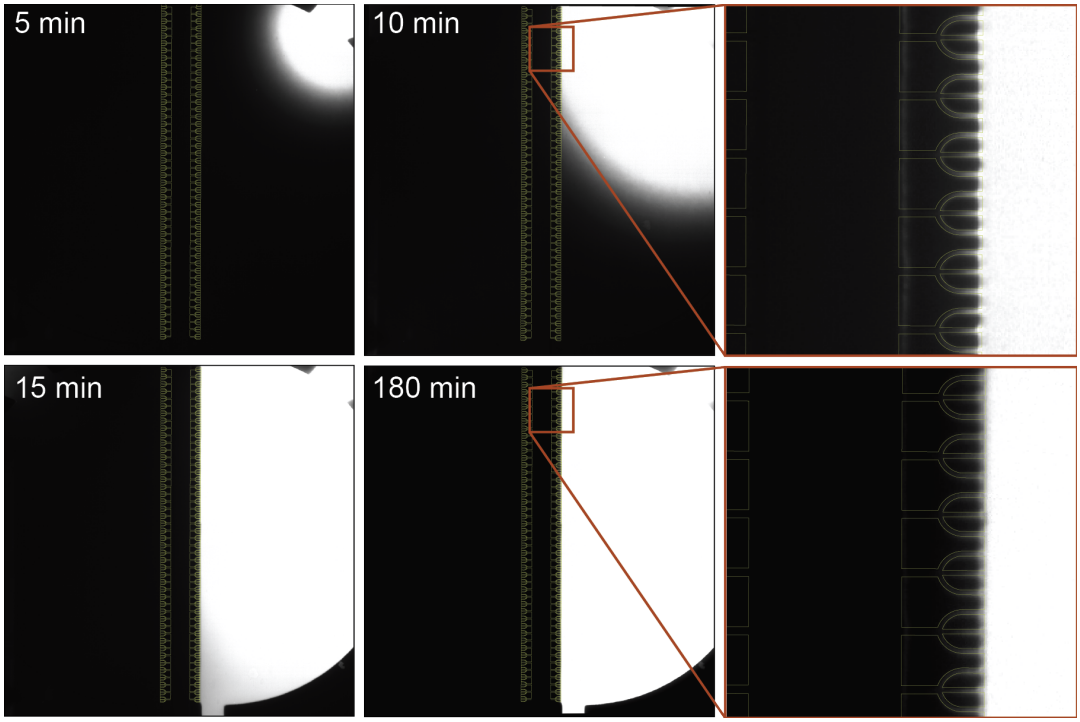

Figure 9. Hydrostatic-pressure driven flow through the channels and fluidic isolation between the individual channels. Central and left inlet ports were filled with PBS, whereas the right channel was filled with PBS complemented with 20 µM sulforhodamine B. The hydrostatic pressure difference is enough to start filling the cell growth chamber with the liquid within 10 min. Note the fluid isolation of the individual channels.

Furthermore, the fluorescent experiments in Figure 9 demonstrate the isolation between the two cell-culturing chambers, preventing the diffusion of small molecules from one cell growth chamber to the other. Only slight traces of the fluorescent dye enter the center channels in the communication region by diffusion and liquid flow. Finite element simulations corroborate the experimental results (Supplemental Figure A.1). Although the central channel got a cross flow close to the outlet, cell chambers were isolated.

2.2.3 LUHMES Cells Differentiation

Three prerequisites for the cell cultures in our model systems must be fulfilled: (i) the cells can be differentiated to neuron-like cells, exhibiting the morphological shape of neurons; (ii) expression level and cellular distribution of selected markers, e.g. synaptophysin and tyrosine hydroxylase (TH), are comparable to the ones observed in primary cell cultures. Especially in neuronal cells with extended neurite networks, the localization of neuronal markers can give relevant information on the differentiation state; and (iii) a similar differentiation pattern among a cell population is needed for reproducible experiments in microfluidics due to low cell numbers.

We tested LUHMES cells for the expression of general neuronal markers (Figure 10) and dopaminergic indicators (Figure 11A) using immunofluorescence labeling and confocal

light microscopy. Expression of the cytoskeletal protein β-III-tubulin (a general neuronal marker) was observed in 100% of the differentiating cells and appears not to increase with longer differentiation times (Figure 10A). After 12 days of differentiation, β-III-tubulin could only be found in neuritic extensions but not in the cell somas. Proliferating LUHMES cells also stained positively against β-III-tubulin to a small heterogeneous extent.

The expression of synaptophysin (Figure 10B), a marker for neuroendocrine cells, was highly heterogeneous up to day 16 of differentiation. We found high expression levels in only a few cell groups, whereas most of the cells were not labeled at all. In later stages of differentiation, a regular expression pattern was found among the entire cell population and after day 18 of differentiation, definite labeling in 100% of LUHMES cells was observed.

The expression of TH among the cell population was studied to examine the differentiation of dopaminergic neurons (Figure 11A). We detected weak labeling against TH before day 12 of differentiation, with only a few cells expressing a lot of TH. Just after 20 days of differentiation, a uniform TH expression was found among the entire cell population.

To study PD-related prion-like spreading α-syn expression levels must be considered (Figure 11B). The immunofluorescence levels of α-syn in proliferating LUHMES cells was low. After six days of differentiation, a uniform labeling of α-syn was visible and the fluorescent intensity remained at a similar level at longer differentiation times. All cells were labeled in soma and neurites. Interestingly, after longer differentiation, several neurites start to build up droplet-like inclusions, which stain highly positive against α-syn.

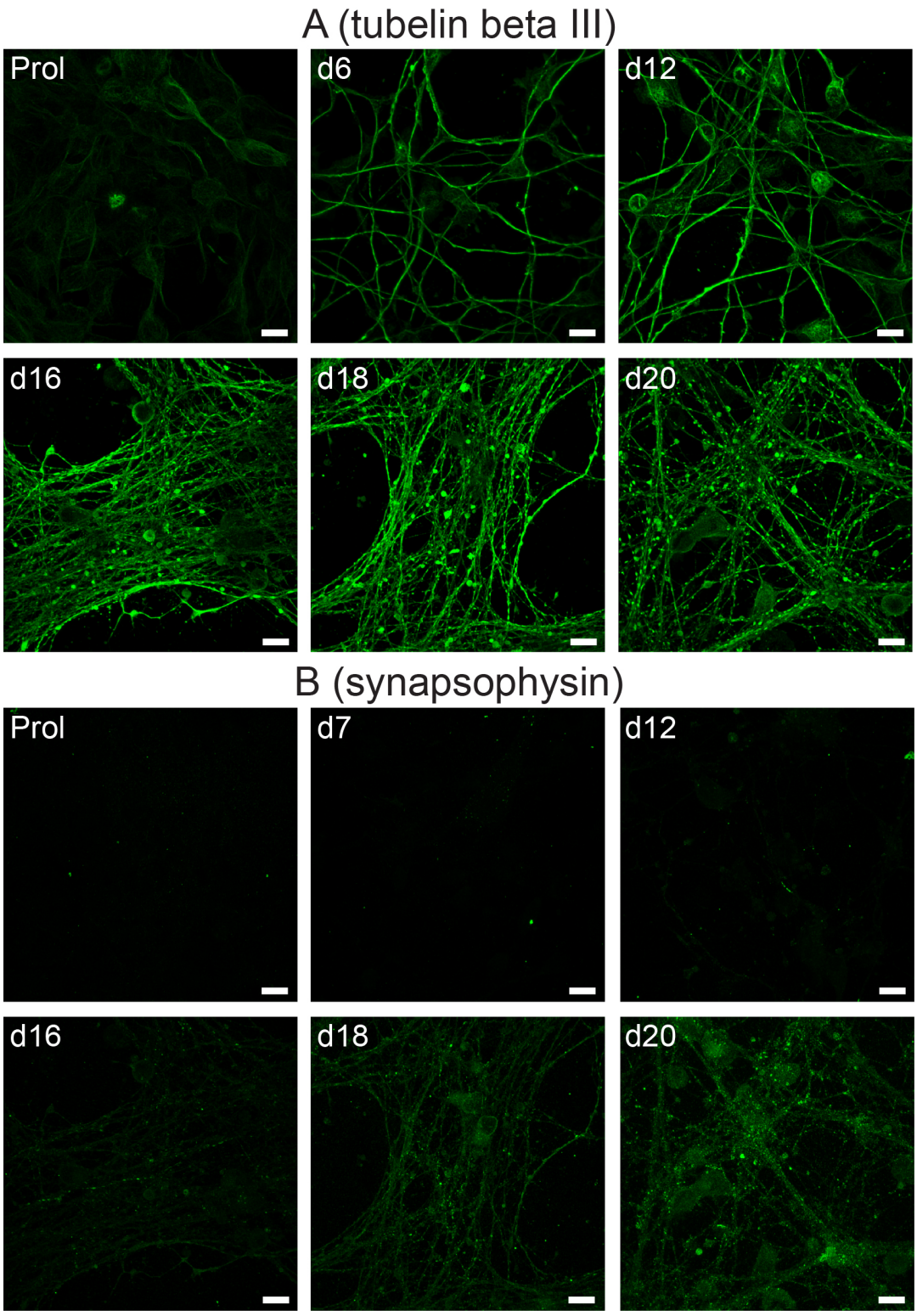

Figure 10. LUHMES cell differentiation monitored for general neuronal markers tubulin beta III (A) and synaptophysin (B) by confocal microscopy. Scale bars 10 µm.

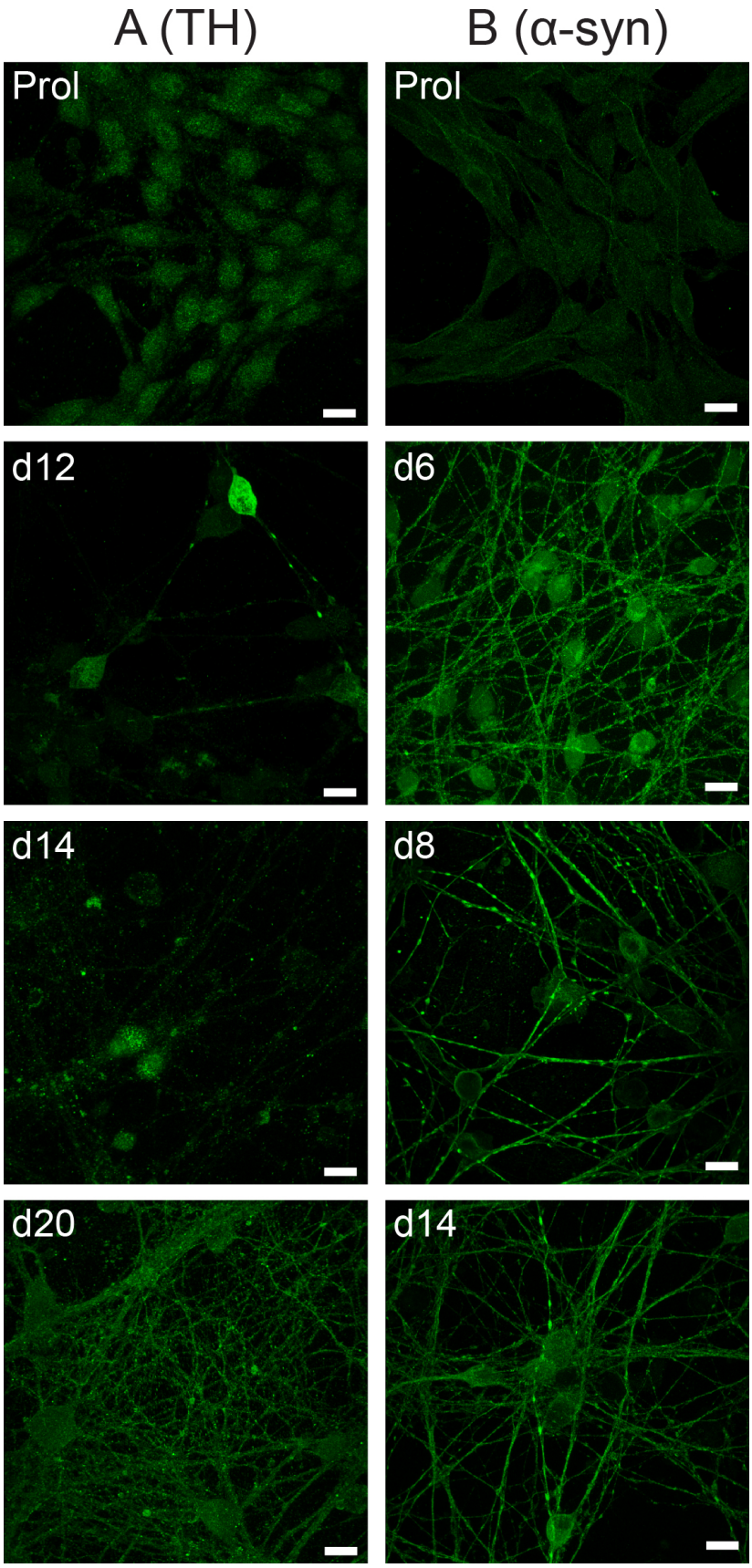

Figure 11. Immunofluorescence microscopy of proliferating (prol) and differentiating LUHMES cells up to day 12 (d12) or day 20 (d20). A) Immunofluorescence signal of tyrosine hydroxylase (TH). B) Fluorescence labeling of α-syn. Scale bars 10 µm.

2.2.4 LUHMES Cell Differentiation in Microfluidic Devices

In our hands, the standard protocols developed for LUHMES cultivation in dishes or well plates did not work in microfluidic chips. Therefore, heuristic optimization by adapting both the microfluidics and cultivation protocols was necessary for a stable co-culturing of LUHMES cells.

Firstly, we adapted the microfluidic chip design from Dinh et al. [311] as described above. Secondly, the standard surface-coating protocols for LUHMES cultivation using poly-L-ornithine and fibronectin [298] did not promote cell attachment in microfluidic devices (Supplemental Figure A.2). But Geltrex® was a suitable substrate for surface coating, leading to a homogenous adhering cell monolayer [309, 326].

Figure 12 shows the differentiation of LUHMES cells in the microfluidic chip. Cells displayed flat morphology a few hours after passaging. After four days, some cells started to attach to the PDMS and grew upside-down. Between day 3 and day 5, a meshwork of neurites began to build up. Subsequently, the neurites grew through the microchannels and started to interconnect the cell populations in the two cultivation chambers. Remarkably, if solely one cell pool was occupied, the neurite network through the microchannels developed slower. Importantly, the microchannels were designed with a height of 4 µm only (Figure 8D). An initial implementation of the chip was established with 3 µm wide and 10 µm height channels, through which cells could actively pass. Channels with a cross-section of 3 µm x 4 µm efficiently suppressed this behavior and built a substantial barrier for the cell somas.

We observed that the liquid flow in the microfluidic chip influenced the outgrowth of the neurites (Figure 12, day 5 to 10). By comparing the neurite growth-pattern with the simulated fluid stream (Supplemental Figure A.1), we recognized that the neurites tend to align along the streamlines and that faster local liquid flow promotes longer neurite outgrowth. Interestingly, this also happens against the stream, and some neurites grew into the supplying channels.

After approximately 8 days, large bundles of neurites are formed in both cell cultivation chambers and in the middle of the central channel. Reducing the flow in the central channel by a longer resistance pipe (Figure 8A-4), the bundle formation is reduced, and the neurites grow more directly to the other cell pool. As observed in cell cultivation in flasks or well plates, the cell somas in microfluidics move closer together and build clusters after 8 days.

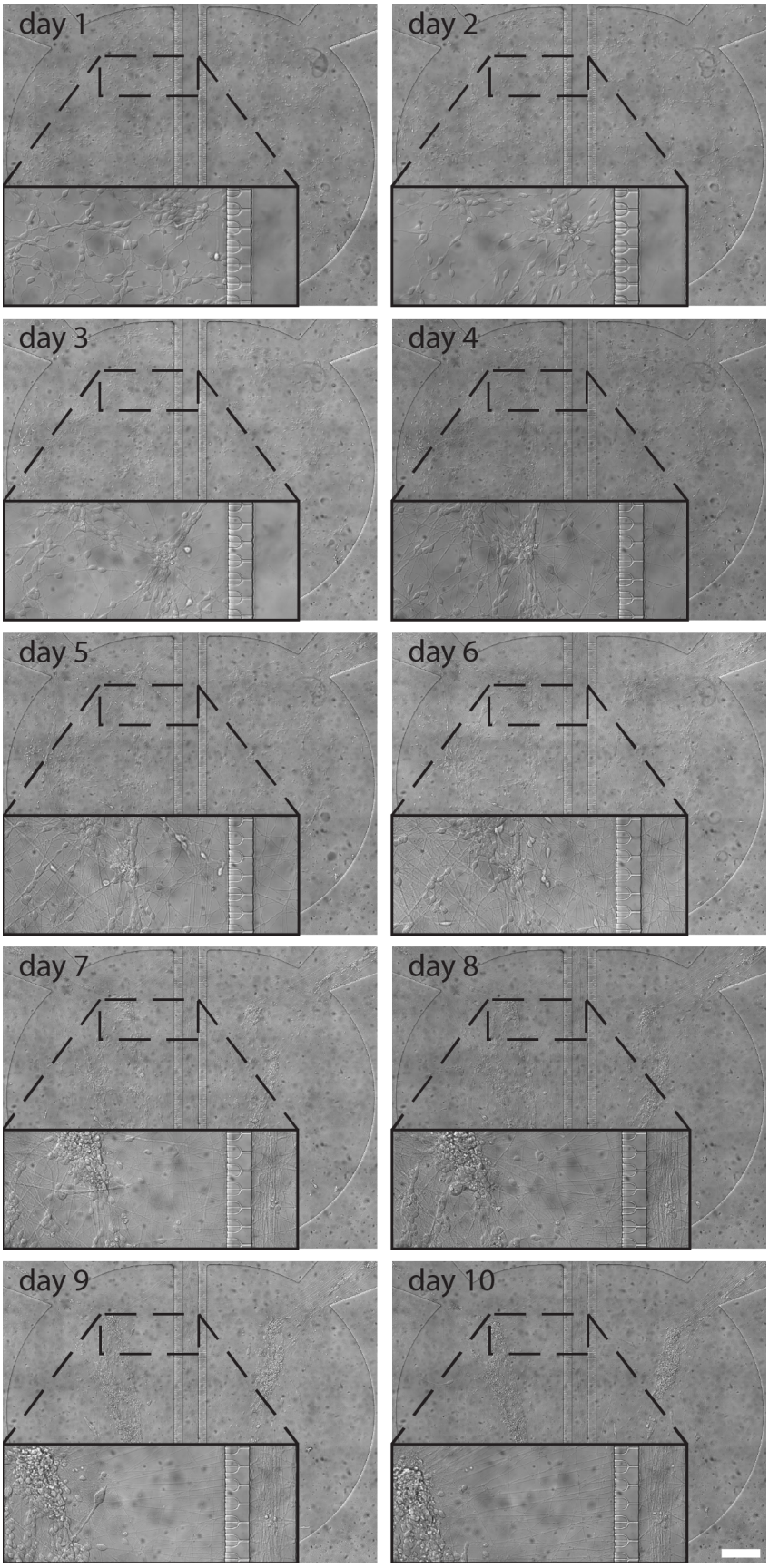

Figure 12. Differentiation of LUHMES cells in the microfluidic chip for days 1 to 10. The overviews show the complete cell population, the insets have three times larger magnification including the central channel region. Scale bar 200 µm.

2.2.5 Exposure of LUHMES Cells to α-Synuclein Fibril Fragments

Seeding experiments in 12-well plates were performed to optimize α-syn fibril-fragment preparation, cell-incubation times, and fibril concentrations. Filaments of overexpressed and purified α-syn were fragmented using a sonicator and labeled with a fluorescent dye. Figure 13A depicts a negative-stain preparation of fragmented filaments in the transmission electron microscope (TEM). The overview image shows fragments where 80% of the fragments exhibit a length between 40 and 100 nm and a thickness of approx. 8 nm or 16 nm respectively. Note, that smaller pieces were also visible in the background. Most filament fragments seem to consist of two filaments (note the darker strip in the middle along the filament axis). LUHMES cells after 3 days of differentiation were exposed ("seeded") for 24 h with α-syn filament fragments. Incubation with varying concentration of seeds (Supplemental Figure A.3) showed that the seed readily associated with the cells. Some of the α-syn fibril fragments were internalized into the cell as shown by confocal microscopy (Figure 13B). The number of seeds taken up by the cell depends on the incubation time and seed concentration in the cell media (Supplemental Figure A.3A). At low levels of 0.05 µg /ml (monomer concentration) few cells took up the fibrils within an hour. At ten times higher fibril concentrations, the seeds cover the cells almost completely after 1 day of incubation. Subsequent seeding experiments were performed using a seed concentration of 0.1 µg /ml and an incubation time of 24h.

To study the retrograde transport of α-syn fibrils, cell media containing fluorescently labeled fibrils was added to the central channel of the microfluidic device. Care had to be taken to load the seed solution after the other ports were filled and to empty the inlet with fibril solution first. Otherwise, crossflow might occur. For both retrograde and anterograde transport, the neurites were regularly observed by fluorescent microscopy and fixed at different chasing times to be analyzed by confocal microscopy. Figure 13C shows an example of retrograde transport of seeds in the chip. Seeds (0.1 µg/ml) were supplied to the central channel and after 24 h the media was exchanged to remove unbound seeds. After a chasing time of 4 days, we fixed and analyzed the cells in the microfluidic chip by confocal fluorescence microscopy. Whereas neurites readily took up the seeds, only a few seeds were transported through the microchannel. Intracellular transfer of α-syn seeds happened only with low efficiency and for short distances of below 200 µm.

Similar experiments (Supplemental Figure A.5) were performed to study anterograde seed transport with comparable results as described above. Note that we did not detect any toxicological effects or morphological changes of the LUHMES cells in all our seeding experiments.

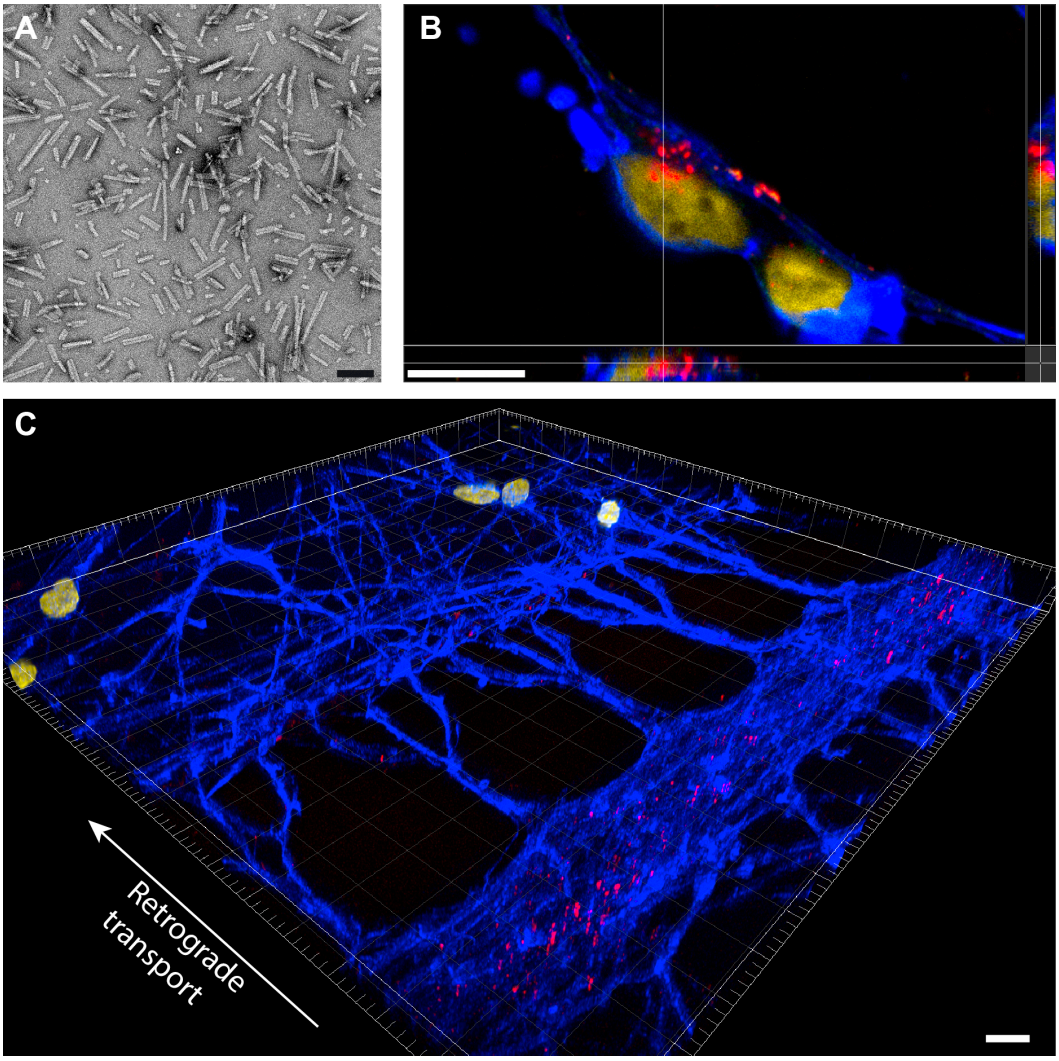

Figure 13. Internalization of α-syn fibrils by LUHMES cells. Alex546 labeled fibrils (red) were added at a concentration of 0.1 µg/ml (monomer concentration). (A) TEM image of sonicated fibrils used for seeding experiments. (B) Representative confocal image of LUHMES cells after 3 days of exposure to α-syn fibrils showing internalized seeds. Nuclei are shown in yellow and actin labeling is shown in blue. (C) Retrograde transport of fibrillar α-syn seeds from (A). Black scale bar 100 nm. White scale bars 10 µm.

2.3 Discussion

Cell models are an important alternative to animal experiments to tackle specific questions in PD pathogenesis and progression. The LUHMES cell line is a human, immortalized cell line and represents the advantages of cell culture models to a great extent. In contrast to primary cell cultures, studies using LUHMES cells cultivated over one week in microfluidic devices were not published till now. Here we describe a microfluidic chip design and cultivation protocols allowing LUHMES neuron differentiation and cell growth for more than two weeks.

To assess the suitability of the LUHMES cell line as a dopaminergic model in microfluidics, we first studied its differentiation to a "dopaminergic monoculture." Previous reports showed that also proliferating LUHMES cells stain against β-III-tubulin and mRNA levels do not increase substantially after two days of differentiation [301]. Thus, β-III-tubulin correlates with the earliest phase of differentiation. Our results corroborate these findings. Confocal microscopy of immunolabeled differentiating LUHMES cells showed a steady and uniform pattern of β-III-tubulin and the fluorescent signals did not further increase after 6 days of differentiation. However, after 12 days we found β-III-tubulin-III labeling only in neuritic projections and not in the cell somas having implications for guidance and maintenance of the neurites. The neurite outgrowth and proper β-III-tubulin labeling make LUHMES cells suitable for intraneuronal transport studies in microfluidics and analysis by optical microscopy.

We found a heterogeneous expression of TH in LUHMES cell cultures in the early days of differentiation. Such an unstable expression was already reported for MESC2.10 cells [299], from which LUHMES cells were sub-cloned, and this was recently observed to be the case for LUHMES cells too [304]. Longer differentiation times of 20 days were needed with our protocols to reach homogenous TH expression levels. Using higher cAMP levels in the cell media could accelerate the maturing of TH expression.

It was reported that α-syn co-localizes with synaptophysin in the presynaptic terminals of mature primary neurons [164]. Additionally, LBs show immunoreactivity against synaptophysin [327]. Therefore, we tested LUHMES cells for stable expression of synaptophysin. Mostly no positive labeling against synaptophysin was found up to day 16 of differentiation, except for intense heterogeneous labeling of a few regions per well. This finding is consistent with previous studies where LUHMES cells were grown in 3D for up to 21 days, finding a similar increase in synaptophysin levels from day 12 to 21 of differentiation [310]. In another study, high synaptophysin mRNA levels were observed after day 6 of differentiation [301, 305], however, mRNA levels do not necessarily correlate with the expression levels of proteins [328].

To assess LUHMES cells as a platform for seed-induced aggregation and transmission of misfolded α-syn species, a stable endogenous α-syn level in wt-LUHMES is required. Optionally, the overexpression of different types of α-syn was already demonstrated in LUHMES cells, whereas controversial results regarding α-syn-induced cytotoxicity were presented [304, 305]. The possibility of a reduced tolerance against high levels of α-syn is not compatible with long differentiation times, which might be needed for an increased maturity of LUHMES cells. In our hands, strong and uniform labeling of α-syn was detected after six days of differentiation, which did not rise any further with longer differentiation times. This finding is different from observations where α-syn was weakly

labeled at the beginning of the differentiation, but where increasing levels of α-syn up to day 9 of differentiation were observed [305]. Combined with the synaptophysin results, we conclude that differentiating LUHMES cell cultures for an extended period seems to be essential for synaptogenesis in LUHMES cells.

The expression of critical cell differentiation markers and the neurite length of LUHMES cells makes them a good cell line to study the prion-like behavior of fibrillar α-syn in microfluidic devices. Despite no media change for two days, no cross flow from one chamber to the other was observed (Figure 9). Fluid isolation and constant stream were maintained over two weeks with minimal effort and equipment. Due to high cell motility, there was no need to array the cells along the connecting microchannels as proposed before [311]. Restricting the cell mobility to only a small band in front of the microchannels promoted cell clustering in front of the microchannels, and the underpressure in the central channel imposed shear stress to the cells. We only could achieve a stable cell growth of LUHMES cells in the microfluidic chips using Geltrex® for the surface coating, and employing higher concentrations of media supplements. More supplements were useful, as supplement concentration in media can be reduced in PDMS devices, likely due to diffusion and absorption of small molecules like growth factors into the PDMS, lower volume to cell ratio, and media dilution when chips were kept in an incubation chamber over two days without media replacement [316]. Increasing the size of the cell pools had a positive effect on cell growth, likely due to the aversion of cells to grow in low numbers. Additionally, the significant pools led to a reduction of the stream, which reduced the alignment of the neurites to the flow. Still, constant flow in the microfluidic device seemed to have a strong influence on the cell network but not on the cell morphology (Figure 12). On about day 4 of differentiation, a neurite meshwork started to build up through the microchannels which connected the two fluidically isolated cell populations. Since cells could be reliably differentiated for two weeks in microfluidic devices, this left about 10 days to perform pulse-chase experiments or toxicity studies.

Several studies reported the uptake and axonal transport of α-syn fibrils in primary mouse neurons [250, 251, 319]. The anterograde transport was stated to be more efficient than the retrograde axonal transport [251]. Our data suggest that studies on intracellular transport could also be conducted on the human LUHMES cell line. The transport of seeded fibrils was observed in both directions, although only for short distances of less than 200 µm and in only a few events. From our results we cannot conclude that transport in one or the other direction is more efficient. The rate-limiting steps could not only be the transport itself but also the uptake and release of the fibrils. The internalization of the fibrils could easily be observed and increased by higher fibril concentrations or incubation times, as LUHMES cells don't show any adverse effect on this type of fibrils. Fluorescent fibrils mostly attached to the cells and were not internalized, which was shown by washing cells with

trypsin to remove a great amount of the membrane-bound fibrils. In microfluidic devices, the constant flow seemed to have a big influence on the uptake, especially on the neurite site. While the binding of the fluorescent fibrils to the cell membrane looked similar in the cell growth chamber and on 12 wells, much lower concentrations were detected on neurites in the central channel, likely due to the higher flow. On neurites in the central channel no bigger aggregates or elongated assemblies were found. Thus, retrograde transport was especially limited by the uptake rate of fibrillar α-syn. Regarding the anterograde transport, the few events could be explained with the longer distance to the separating area, as soma often arranged around the center of the growth chambers. However, similar studies using primary neurons reported fluorescent fibril transmission over distances of 1 mm [252].

Another limiting factor might be the secretion of the previously internalized fibrils. In general, a higher number of fibrils were observed on the background after a few days of seed incubation, even when membrane-bound fibrils were removed with trypsin. Thus, fibrils were released, although it is likely that a substantial amount came from apoptotic cells. In the case of microfluidic co-culturing, the release without immediate uptake of second order neuronal cells leads to a decrease of fibril concentration because of the constant flow. This was less the case in 12-well plates where we observed a slow decrease of the fluorescent signal.

Degradation of internalized fibrils could decrease the number of seed transmission events even further. Lysosomal degradation of α-syn fibrils could be a significant limitation, and no studies exist about lysosomal degradation in LUHMES cells. Studies about degradation kinetics using other cell cultures reported that most internalized fibrils are degraded, although there are controversies [246]. However, intracellular α-syn assemblies in LUHMES cells were observed more than 14 days after incubation, and several studies show high concentrations of transmitted α-syn fibrils in primary cell cultures after several days of incubation [253, 319].

In general, we have shown that LUHMES cells can be used to monitor the anterograde and retrograde transport of possible prion-like proteins. As only one type of fibril was tested here, comparisons to other kinds of fibrils, oligomers, and different types of prion-like proteins would eventually reveal strain-dependent transport behaviors.

2.4 Conclusion and Outlook

In this paper, we demonstrate the integration of the LUHMES cell line into microfluidic devices for separating soma and neurites. Therefore, no additional surface patterning or guidance molecules were needed. Besides the production of the microfluidic chips, the effort for cultivation is comparable with standard protocols and can be done in every cell culture lab without additional equipment. LUHMES cells exhibit a strong dopaminergic phenotype, and therefore, seem to be ideal for testing Parkinson's disease-related agents. Since the system is a low-cost application, it is ideal for high throughput experiments for testing several different strains of α-syn assemblies to measure transmission efficiencies.

CHAPTER 3

Testing Key Steps for Prion-Like α-Synuclein Hypothesis in LUHMES Cell Line

This chapter addresses questions about the required steps of α-syn seed propagation, namely internalization, transport, and release of α-syn assemblies. It is a continuation of the previous chapter with additional experiments and discussions concerning the prion hypothesis in LUHMES cells.

3.1 Introduction

In the previous chapter 2, LUHMES cells were systematically tested for dopaminergic characteristics in order to evaluate their use to serve as an *in vitro* model system for the study of the prion-like spreading hypothesis of PD. Furthermore, a co-culturing device was developed which allows the co-cultivation of LUHMES cells with soma and neurites physically separated. Both dopaminergic characteristics and co-cultivation of LUHMES cells are required to conduct experiments that address the different steps of α-syn pathological spreading – internalization, transport, and release of α-syn fibrils – which are central for the prion-like hypothesis. A detailed review of these steps can be found in the introduction of this thesis (section 1.4.2). In this chapter, we pursued seeding experiments using mostly preformed α-syn fibrils. Furthermore, seeding experiments with differently prepared α-syn assemblies were performed, since recent findings have indicated that distinct α-syn strains might be responsible for the heterogeneous pathological patterns of synucleinopathies [329].

3.2 Results and Discussion

3.2.1 Internalization of α-Syn Assemblies

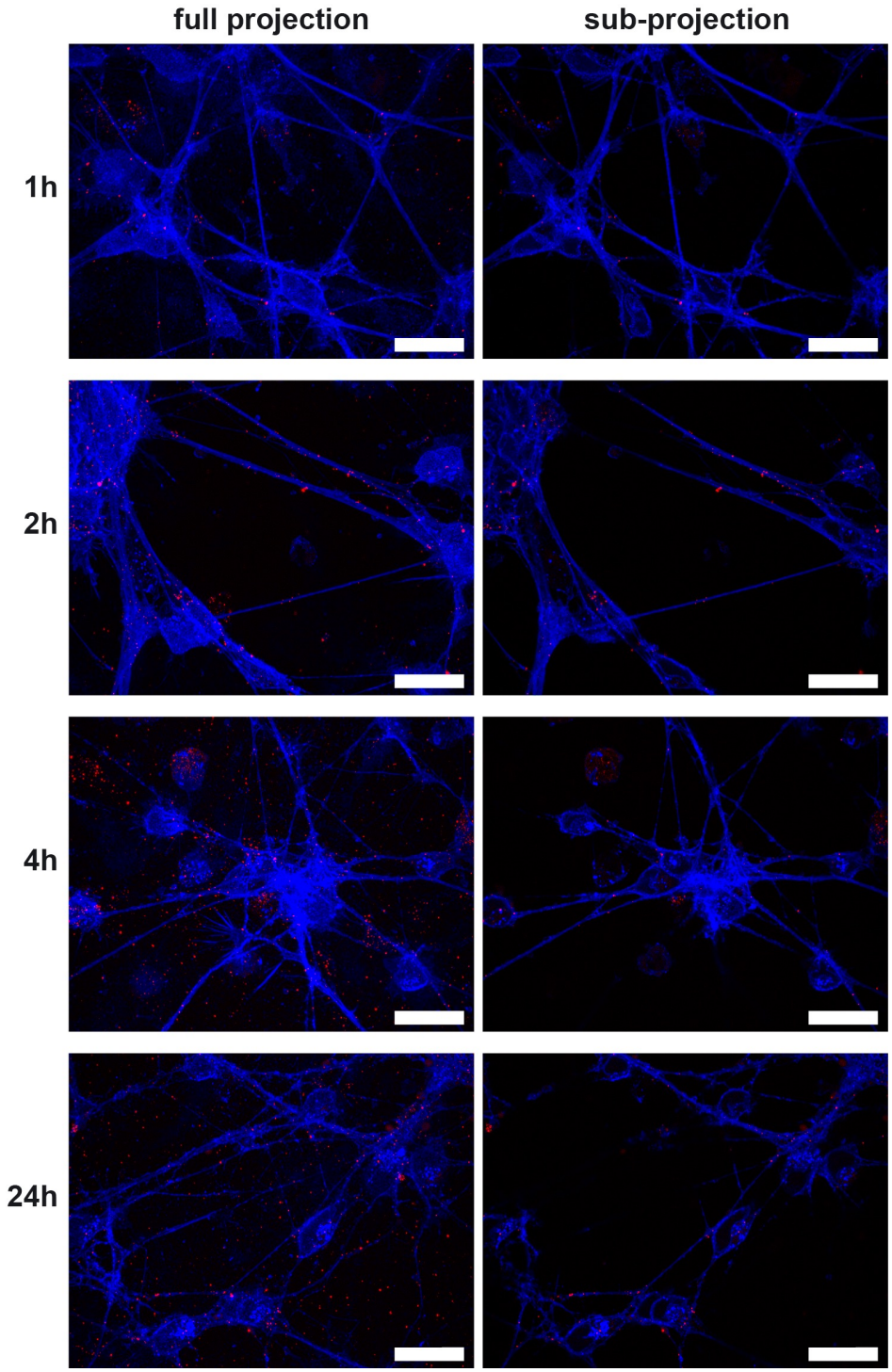

Figure 14. Time course of internalization of fluorescent α-syn seeds in LUHMES cells on day 8 of differentiation. Fibrillar seeds were added at a concentration of 0.1 µg/ml and cells were fixed after the indicated time passed. Left panel shows maximum intensity z-projections of confocal stacks. In the right panel, projections of sub-stacks (corresponding to 1 µm in z-direction) were selected to only show a volume that is cutting through the cells. Scale bars 20 µm.

Internalization of α-syn fibrils was previously demonstrated by confocal microscopy (section 2.2.5). In general, this is assumed to be a fast process after initial binding of fibrils to various structures on the cell membrane [277]. Among different studies, the kinetics of seed uptake appear to vary, which could be explained by unequal cellular models and conditions, strain differences in α-syn fibril samples, and in different seed-preparation techniques [246]. To get insights into seed internalization of LUHMES cells, we analyzed the uptake of fluorescent α-syn fibrils in time course experiments (Figure 14). After 1 h incubation time at an α-syn fibril concentration of 0.1 µg/ml several fluorescent puncta were found within cells (Figure 14, right panel). Interestingly, the intracellular concentration of seeds only increased up to 2 h of incubation and not gradually for 24 h. The overall concentration of seeds sticking to the cell membrane and to the growth substrate increased constantly because seeds in solution had more time to settle (Figure 14, left panel). In a similar experiment (Supplemental Figure A.3), cells were incubated for 1 h with fluorescent seeds but were cultivated for another 3 days instead of immediate fixation. More fibrils were detected in this previous experiment, indicating that LUHMES cells internalized the membrane-bound fibrils during the additional 3 days of cultivation. Since the intracellular concentration does not show a significant increase at 24 h of incubation (Figure 14, right panel), it is suggested that after a rapid initial internalization, large amounts of seeds follow a slower internalization mechanism.

It was reported that seed uptake into neuronal cells reaches a maximum level between 6 h and 24 h, and that the majority of endocytosed fibrils are degraded [257, 269]. It is likely that the uptake and degradation kinetics largely depend on the cell type [246]. Thus, the observed uptake kinetics into LUHMES cells does not contradict the published findings. Focusing on fluorescent puncta after long cultivation times, we saw a decrease of fibrils associated to cellular structures, but mostly an increasing background of fluorescent fibrils (Supplemental Figure A.3B). It seems that the fibrils were not necessarily degraded but rather secreted from the cells. Indeed, we could not observe a co-localization of α-syn fibrils with lysosome-associated membrane protein (LAMP) 1 and 2 (Figure 15A and B). To verify these results, a pulse-chase experiment using fluorescently labeled wheat-germ agglutinin (WGA) was done. WGA is a widely-used lectin which binds to glycoproteins and is often used for cell membrane and Golgi labeling. When used in live cells at 37°C, it rapidly enters the endosome-lysosome pathway where fluorescent signals can be observed in early endosomes after 10 min, in late endosomes after 30 min, and in lysosomes after 1 hour [330]. When seed-loaded LUHMES cells were incubated with fluorescent WGA, no significant co-localization was observed (Figure 15C). It is possible that fluorescent dyes dissociate from the fibrils in the lumen of the endocytic compartments and, therefore, no co-localization of α-syn fibrils and lysosomes is observed. However, this would imply that fluorescent puncta only consist of aggregated fluorophores and that they are not located in

the endosome-lysosome compartments. Still, this would not explain why other studies have observed co-localization and high levels of fluorescent puncta, even after long cultivation times [253].

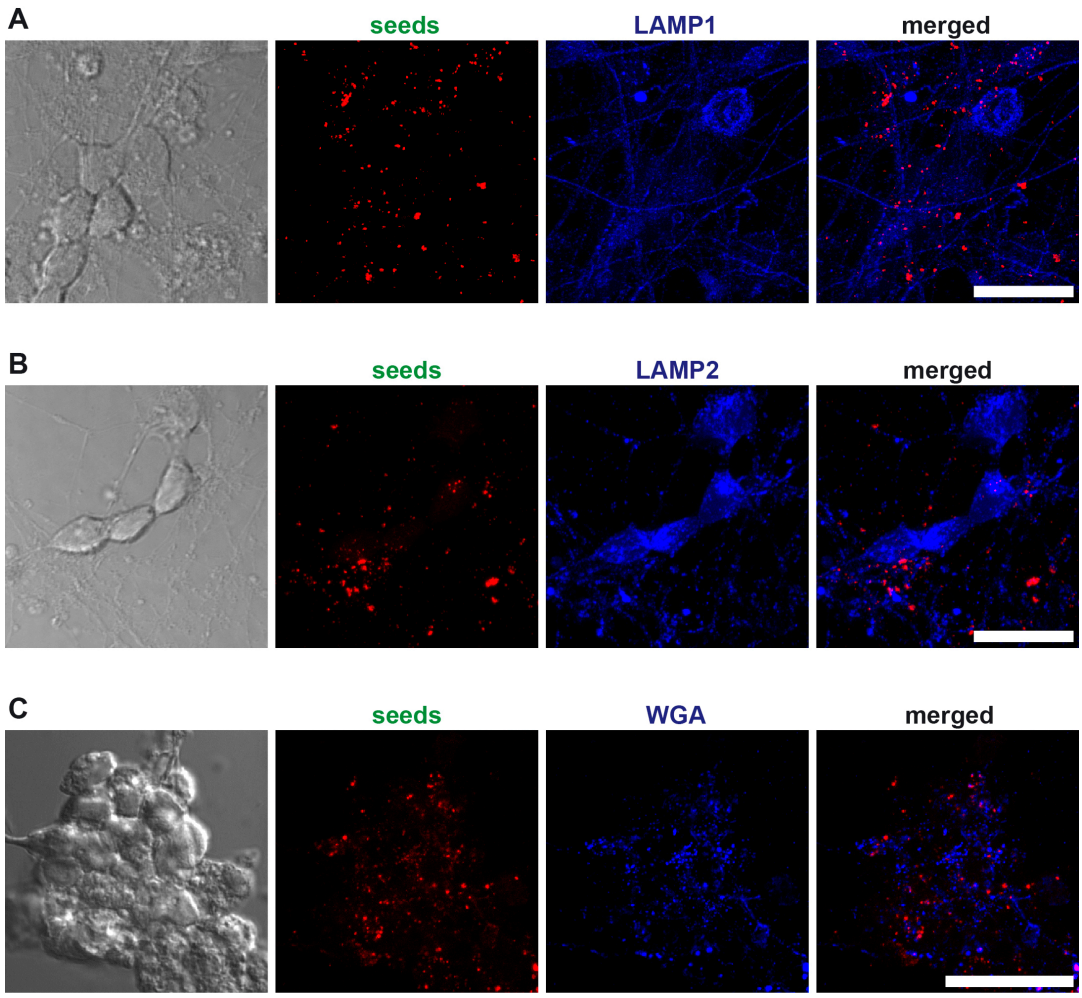

Figure 15. Localization of α-syn fibrils and lysosomes in LUHMES cells. Cells were incubated with seeds from α-syn fibrils. Fixed cells were immunofluorescent labeled with LAMP1 (A) and LAMP2 (B). Alternatively, cells were incubated with fluorescent WGA which is known to co-localize with LAMP positive structures (C). Scale bars 20 µm.

Consistent to co-localization with endosomal markers and degradation of internalized α-syn fibril, a decrease of extracellular fibrils was reported, indicating that the fibrils are being cleared from the media by endocytoses [269]. To verify these findings in LUHMES cell cultures, cell lysate was prepared on three different days after seed incubation. In addition, supernatant of the detached cells was collected prior lysis; one set of cells was detached with trypsin and the other by gently rinsing with PBS. Trypsin was used to efficiently remove membrane-bound α-syn aggregates. The supernatant was analyzed by dot blot immunolabeling, and cell lysate was analyzed by reverse phase protein arrays (RPPA), whose development is described in section 4.2.3. Cell lysate from cells which where incubated with fibrils for two days showed high levels of α-syn, but only when cells were not trypsinized before lysis (Figure 16, top panel d8). This indicates that membrane-bound fibrils exceeded the concentration of endocytosed fibrils by far, even after 2 days of incubation. The signals equalize after 4 days of cultivation (Figure 16, top panel d10), which supports the theory that LUHMES cells require longer time for internalization after initial seed binding. At this point, membrane-bound fibrils appear to be less abundant than intracellular seeds. After 6 days of incubation (Figure 16, top panel d10), the α-syn signal in trypsinized cells was higher than when detached without trypsin. Since the latter represents endocytosed and membrane-bound fibrils combined, a higher signal from only endocytosed fibrils is contradictory. However, since the control with simple cell media shows an increased signal too, the findings on day 13 of differentiation are not reliable.

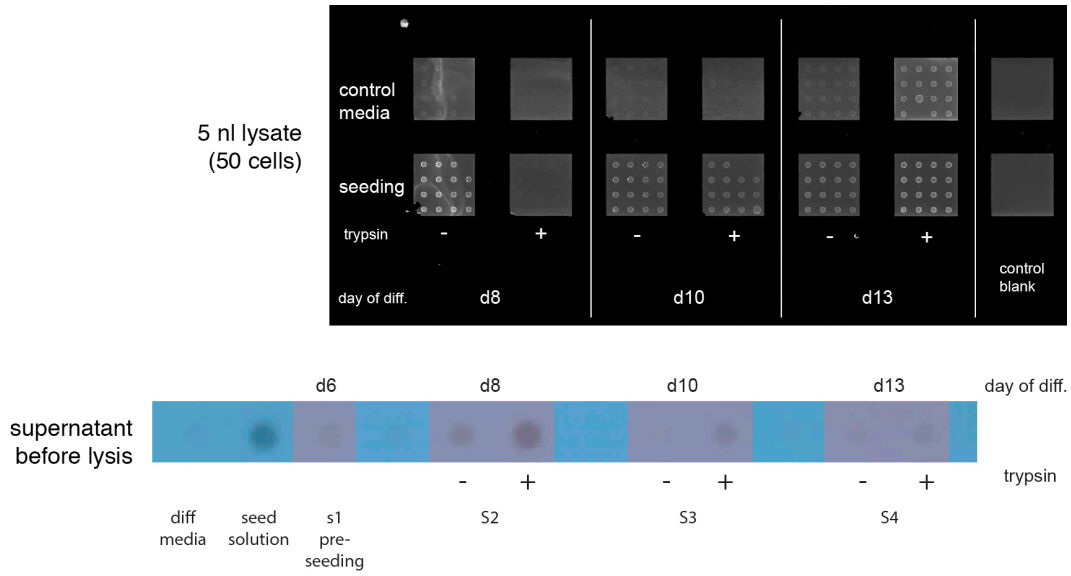

Figure 16. Immunoblot analysis of LUHMES cell lysate and media supernatant after α-syn fibril seeding. Top panel shows a reverse phase protein array of LUHMES cell lysate prepared on three different days of differentiation. Bottom panel shows a dot blot analysis of the supernatant which was collected from the supernatant of the pelleted cells before they were lysed.

Dot blot analysis of the supernatant of the very same experiment shows a decreasing signal of fibrils in the supernatant (Figure 16, bottom panel). This is in agreement with the increased number of internalized fibrils. Since the cell media was exchanged several times before analysis, this represents only the fibrils which were secreted or membrane-bound and then released into the media. Interestingly, when no trypsin was used, there was still a weak signal of extracellular fibrils up to 6 days after seed incubation. Insufficient washing could explain the higher signal during the first harvesting on day 8 of differentiation (Figure 16, bottom panel). But it is unlikely that initially seeded fibrils are in the media after three washing steps before day 13 of differentiation. This indicates that some fibrils are released back into the media without degradation.

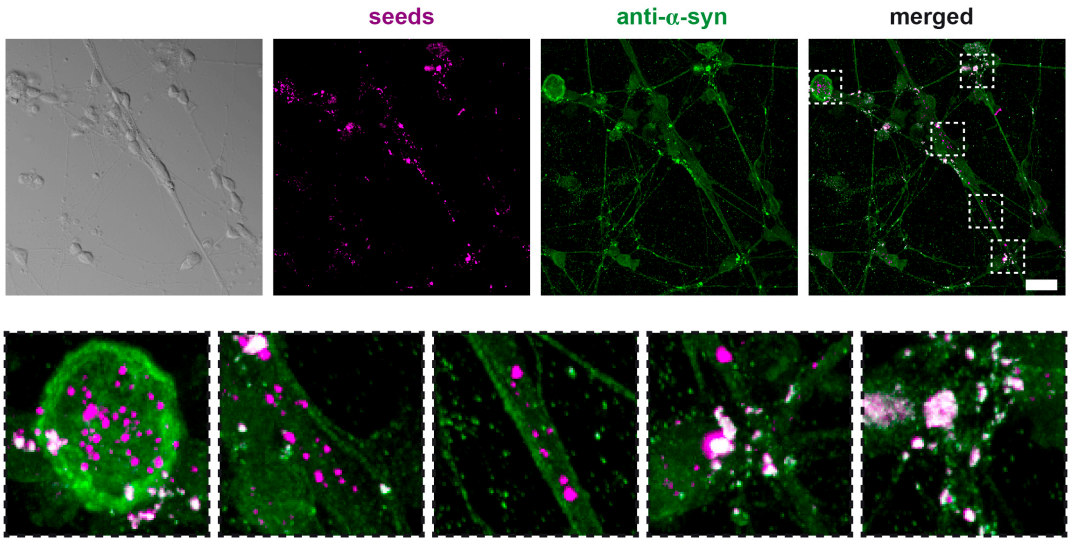

Figure 17. LUHMES cells were incubated with 0.5 µg/ml α-syn for one hour on day 7 of differentiation and fixed on day 10 of differentiation. Seeds are represented in magenta, endogenous α-syn in green, and seeds which were recognized by anti-α-syn-antibodies in white. Scale bar 20 µm.

When fixed LUHMES cells were immunofluorescence labeled with anti-α-syn antibodies, both endogenous α-syn and seeds were labeled (Figure 17). Since seeds are already fluorescently marked, double-labeling results in a distinct color in the additive color system. In Figure 17, antibodies labeled both endogenous α-syn (green) and seeds (white). α-Syn fibrils which were not recognized by the antibodies do not result in an additive signal (magenta). An incomplete labeling was observed with all the tested antibodies, while some only poorly recognized seeds (Supplemental Figure B.2). However, even antibodies with good labeling efficiency against seeds did not bind to all α-syn fibrils (Figure 17, insets). The reason that not all α-syn fibrils are recognized by the antibodies remains unknown. It might be due to changed or hidden epitopes on α-syn, or due to

dissociation of the dyes from α-syn as mentioned above. It appears that most of the evaded seeds are located within cell bodies or neurites, but not antibody bound seeds without association to cellular structures were also present. These extracellular blank seeds, and a thorough permebilization of the cells before immunolabeling, excludes the option of shielding organelles, such as lysosomes, which could prevent the contact with antibodies. It can only be hypothesized that α-syn fibrils were modified during aggregation within the cells, which made them undetectable. Since evasion from degradation and release from cells is required to fulfill the prion-like spreading hypothesis, it might explains the potentially modified fibrils outside of cells.

Although we did not find any signs for fibril degradation by the endosome-lysosome pathway, we cannot implicate a complete evasion of the used α-syn fibrils from this system. It was shown that α-syn are immediately internalized, but a possible saturation is only reached after several days of incubation. Furthermore, a part of the seeded fibrils is not recognized by antibodies. There are many open questions regarding α-syn fibril internalization and escape from degradation [246].

3.2.2 Release of α-Syn Fibrils and Intercellular Transfer

Cell-to-cell transfer of α-syn fibrils can be established by direct cellular contacts or via transport through extracellular space. Recently, direct transfer through tunneling nanotubes was demonstrated [257]. Although this was claimed to be a highly efficient process, it is expected that the majority of intercellular transfers involve a vesicle-free release from the donor cells to extracellular space [252].

In most of our seeding experiments, a lot of α-syn fibrils were found in the background not associated to soma or neurites, and this number increased the longer the cells were cultivated after seeding (Supplemental Figure A.3B). Mostly the background signals derived from membrane-bound fibrils, since trypsin treated samples showed largely reduced numbers of fibrils in the background. However, fibrils could still be found in the background of trypsin-treated samples (Supplemental Figure A.3B). These were either secreted or released from dying cells.

To see if α-syn fibrils are transferred between LUHMES cells, α-syn fibrils were separately labeled with two different dyes and seeded onto two separate cell cultures. After one day, both cell populations were trypsinized to remove membrane-bound fibrils, and mixed together for further cultivation. After 10 days of incubation, we did not detect a single cell which contained both types of fibrils (Figure 18). Extracellular seeds were often found in close proximity to cellular debris, as they could be recognized by the contracted nuclei in Figure 18. This indicates that most of the free α-syn fibrils were not secreted but were exposed to cell media after the α-syn harboring cell died. Interestingly, regardless of

the fact that they derived from dead cells, released α-syn fibrils did not enter intact cells. It is likely that intercellular transfer is a relatively rare event. In similar experiments, a transfer efficiency below 20% for cells which are not in close contact was reported [257]. It is also worth noting that published studies which used different cell types and different seed preparation protocols also reported different levels of uptake and transfer [257, 270, 288].

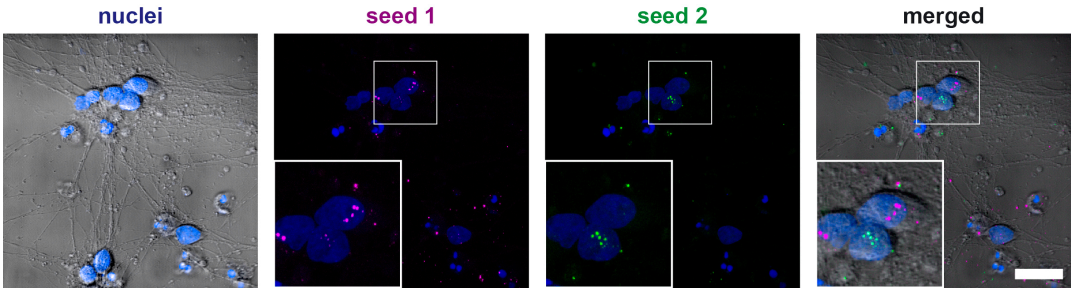

Figure 18. Seeding experiment on LUHMES cells using two differently labeled seeds (green and magenta) of the same filament sample. Separate cell cultures were incubated with the particular seeds on day 1 of differentiation. The next day, cells were trypsinized and combined for cultivation until day 11 of differentiation. Nuclei (blue) and bright field image were adjusted for the merged figure to highlight the seeds. The channel represented by the green color is leaking to the magenta channel. Scale bar 20 µm.

3.2.3 Recruiting Endogenous α-Syn

Template recruitment of endogenous α-syn by misfolded seeds should be discernable in the fluorescent pattern of immunolabeled α-syn, as was demonstrated in several studies [253, 267, 319]. In our seeding experiments, the endogenous α-syn labeling never showed any difference between α-syn fibril-induced samples and control cell cultures. The endogenous α-syn was mostly homogeneously distributed in soma and neurites (Supplemental Figure B.2).

Usually α-syn seeds aggregate with each other after a few days of incubation in cell cultures. When comparing Figure 14, where cells were fixed after short incubation times, and most other experiments, where cells were further cultivated after seeding (e.g. Figure 17), we see an increase in size of the fluorescent puncta. Thus, preformed fibrils still aggregate, although the concentration is extremely low. Since many of these aggregates can be found in association with cellular material, we hypothesize a local increase of seed concentration on the cellular membranes, which assists the formation of larger α-syn fibrils aggregates. Although aggregate formation of the added seeds was common, additional α-syn labeling with antibodies did not reveal a growth of the original seeds. This indicated that endogenous α-syn was not recruited by misfolded α-syn templates. The

reasons that no changes were observed could be various. Eventually, template recruitment is only visible after long cultivation times, which is not manageable for LUHMES cells. Furthermore, cellular model systems in general can have different responses to α-syn seeding and since α-syn strains might play an important role in synucleinopathies, various seeds might trigger aggregation with different efficiencies. Thus, the weak response in this study might be attributed to the strain of α-syn we used, fluorescent modification of the seeds, or to LUHMES cells themselves.

3.2.4 Strains of α-Syn: Fibrils, Ribbons, and Oligomers

For the majority of the seeds produced in this thesis, an adapted version of a published protocol was used [189] (Figure 19,A). Additionally, we adapted three published protocols which aim for α-syn fibril, ribbon, and oligomer production [140, 331, 332]. A representative selection of the fibrils, which were produced based on these protocols can be seen in Figure 19 and in Supplemental Figure B.1. All fibril-formation protocols use similar protein concentrations, incubation temperatures, and pH. The main differences among them was the type of buffer and salt concentration. As a result, structurally different fibrils were formed. Although the standard fibrils were incubated for 7 days, batches of fibrils could already be found 30 h after incubation (Supplemental Figure B.1). The fibrils were of heterogeneous length and seemed to be ruptured. It is likely that incubation on a shaker caused this fragmentation, since the initial protocol used a rotating wheel in which longer fibrils were formed [189]. By using the same buffer, extremely long filaments could be formed over long incubation times, even at RT (Supplementary Information B.1). Such long networks were also observed when using Tris buffer. There, prolonged incubation times led to large insoluble aggregation which are difficult to detected by TEM, since aggregates cleared all the free fibrils from the solution and concentrated in big precipitates (Supplemental Figure B.1).

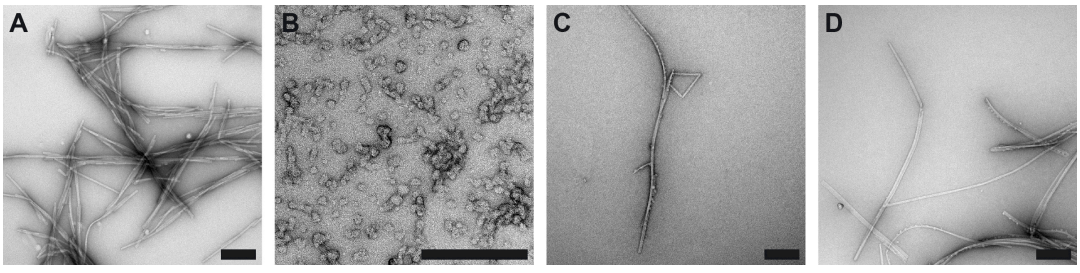

Figure 19. Representative images of negatively stained α-syn fibrils and oligomers produced with different protocols. These protocols manly differ in buffer composition. (A) Standard fibrillization protocol for this thesis using PBS according to ref. [189]. (B) Oligomers were formed based on common protocol from ref. [332]. (C) Fibrils made in sodium phosphate buffer at high salt concentrations. Triggering the initial fibril formation was omitted from the protocol [331]. (D) In Tris buffer, α-syn assemble to ribbon like fibrils [140]. Scale bars 200 nm.

When using phosphate buffer at high salt concentrations, usually less fibrils were formed and were often decorated by oligomers (Figure 19C). In Tris buffer, a similar decoration was observed but fibrils developed a ribbon-like structure. As this decoration looks like oligomers, they might be related to the fibril formation process. Interestingly, we did not find any oligomers during the standard procedure. This is remarkable, since oligomer and standard fibril formation followed the same protocol, except oligomers were harvested after two days of incubation from a threefold-higher concentrated α-syn solution, followed by separation from already formed fibrils and subsequent up concentration. Thus, oligomers in Figure 19B represent the precursors of those fibrils. Overall, a high heterogeneity of fibrils can be formed by changing one of the many conditions. This is important, regarding reproducibility of experiments, but also in the context of PD progression. Even minor changes in certain cells can completely alter the environment for toxic α-syn formation.

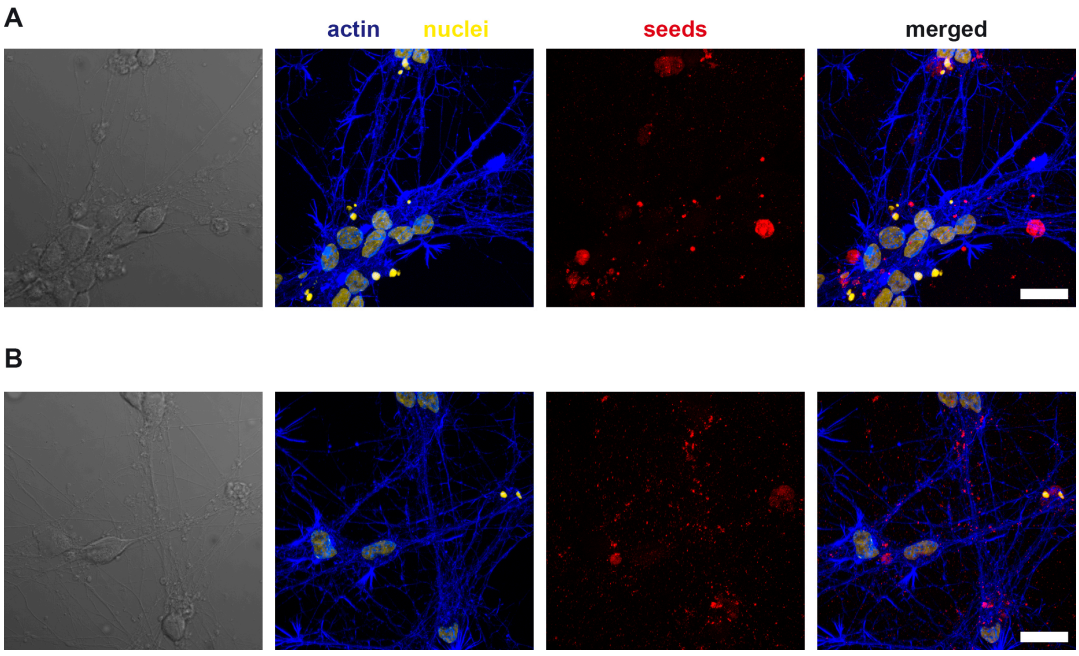

Figure 20. Representative confocal microscopy images of seeding experiments using oligomers which were either added on day 3 of differentiation (A) or on day 6 of differentiation. LUHMES cells were fixed on day 13 of differentiation. Scale bar 20 µm.

Besides the already mentioned seeding experiments with sonicated α-syn fibrils, LUHMES cells were incubated with fluorescently labeled oligomers on either day 3 (Figure 20A) or day 6 (Figure 20B) of differentiation and were cultivated for an additional 10 or 7 days respectively. Comparing those two preparations, less oligomers could be found in the background of day 3 seeded cells. Additionally, fluorescent spots are bigger

and often concentrate on cell debris. Overall, similar levels of fluorescence were observed in both preparations, which indicates that oligomers were not cleared from the background by internalization and degradation. Rather, they accumulated to big aggregates and even completely occupied whole cells (Figure 20A). Whether or not oligomers were responsible for the cell death of the fully fluorescent cells remains to be tested. It needs to be explained why those cells internalized such amounts of seeds whereas cell soma and neurites of neighboring cells display virtually no fluorescent seeds. In context with the selective vulnerability theory, it almost seems that those cells selectively internalized the seeds.

Examining cell preparations where oligomers were added 3 days later (Figure 20B), signs of aggregate formation start to appear. Still, the fluorescent signals are more diffuse and although there are dead cells, none of them accumulated big amounts of seeds. Furthermore, seeds are distributed evenly on soma and neurites. Whether these differences among the two preparations result from the longer exposure to seeds, or if the differentiation status on time of seeding plays a role, remains to be determined. As LUHMES cells change their differential status rapidly within the days of differentiation, it is likely that the timepoint of seeding is important.

In general, large accumulations in live and dead cells were also observed in seeding experiments with α-syn fibrils, and thus are not a unique strain-dependent feature (see section 3.2.3).

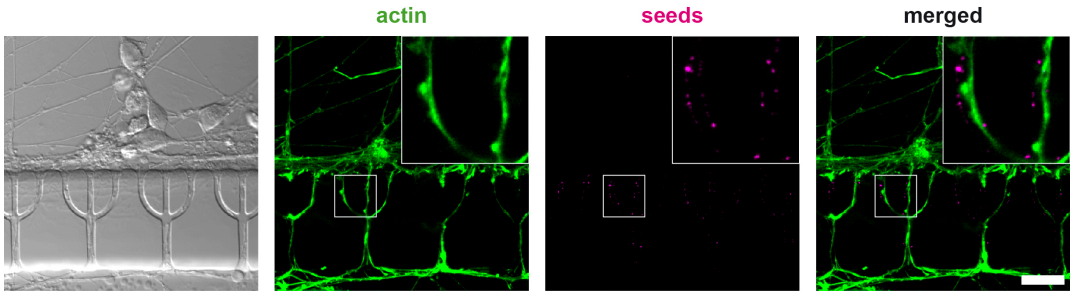

Figure 21. Seeding experiments using oligomers which were added to one of the cell growth chambers in the neuron co-culturing device. Most oligomers (magenta) stick to the PDMS and do not co-localize with the actin filaments (green) of the neurites. Scale bar 20 µm.

Big differences were observed when oligomers and fibrils were applied to microfluidic devices. Whereas α-syn fibrils were internalized by cell bodies and neurites, and transmitted in anterograde and retrograde directions (Figure 13), oligomers were barely detected on cellular structures (Figure 21). Most oligomers bound to the PDMS walls of the microchannels and not to cells. Fibrils usually also attached to the PDMS, but also covered cell bodies and neurites. Low concentrations of oligomers associating with cellular

material could be due to a steady fluid flow in the microfluidics device, which would indicate that oligomers have a much lower binding affinity to cell membranes than fibrils. This is not in agreement with most published data, where a high oligomer adsorption to cell membranes was reported [332]. It is important to note that oligomers with different potentials to trigger aggregate formation can be produced [199]. Although we followed a protocol for highly potent oligomer formation, it is possible that changes in microfluidic culture conditions altered the oligomer binding capacity.

Although conformational strains of α-syn might play an important role in explaining the pathologic variability of synucleinopathies, there is not much known about their ultrastructure. Most studies which use artificial α-syn aggregates for seeding experiments, including this one, prepare their assemblies without thorough characterization or purification. These protein solutions might consist of a polymorphic mixture of monomeric, oligomeric, prefibrillar, and fibrillar α-syn. Thus, when conducting experiments about the prion-like nature of α-syn, valuable information about the influence of each species is lost. Extracting individual assemblies from the cell for characterization, or even direct characterization in cells, would be beneficial. Differences in fibril formation protocols, sonication techniques, or storage could then also explain the different controversial results of different studies.

3.3 Conclusion

In this chapter, seed internalization and secretion was demonstrated in the LUHMES cell model using confocal microscopy and dot blot analysis. Immunofluorescent labeling showed only incompletely marked fibrils, which suggests morphological changes of the initial seeds, hidden epitopes during aggregate formation, or dissociation from fluorescent dyes. In all experiments, LUHMES cells showed weak responses to incubation with α-syn assemblies regarding seed propagation of α-syn. It is suggested that different cell types might display different susceptibilities to α-syn seeds. Furthermore, a huge variety of α-syn fibrils can be produced *in vitro*, although the exact structure of the seeds which are finally used for the experiments remains unclear. Thus, additional studies with different α-syn assemblies are needed to demonstrate a strain dependence in different neuronal model systems. In LUHMES cells, differences in seeding experiments between oligomers and fibrils were marginal. Only when seeded in microfluidic chips did oligomers seem to have a different binding affinity to cell membranes than fibrils.

CHAPTER 4

Making Microfluidics Accessible to Electron Microscopy and Single-Cell Analysis

This chapter evaluates additional techniques to make neuronal co-culturing microfluidic devices accessible to analysis by electron microscopy. Three main approaches were tested for feasibility, of which two include the integration into the visual proteomics pipeline which was developed and constantly improved in this group.

4.1 Introduction

A part of this section has been published and was reprinted and modified with permission from reference [333]. Copyright (2017) Creative Commons License 4.0

*Arnold S.A., Albiez S., **Bieri A.**, Syntychaki A., Adaixo R., McLeod R.A., Goldie K.N., Stahlber H., Braun T., J Struct Biol, 2017. 197(3): p. 220-226.*

Microfluidic cell cultures aim for a small number of cells per condition down to single-cell experiments. Often biological analysis techniques lack sensitivity on a single-cell level. A seamless integration of microfluidic cell culture would require the handling of small volumes. Therefore, a direct integration of cellular microfluidics to EM sample preparation techniques would benefit from both small sample volumes and cell numbers, as well as high sensitivity. Currently, we are developing a modular microfluidics pipeline with the aim of integrating sample extraction, purification, and analysis preparations in one workflow. As of now, this platform provides working modules for single-cell lysis [334], sample conditioning for EM [335] and lossless cryo-EM grid preparation [333]. Modules for purification and additional handover to other analysis methods are in progress. However, analysis by cryo-EM would have a great impact on the proteomic analysis of small volumes and rare events which could happen in microfluidic cell culturing.

In recent years, transmission electron microscopy of vitrified specimens [336] has become a powerful technique for the high-resolution structural analysis of biological matter, and is

now increasingly recognized as a mainstream tool in biology [337-339]. Several technical achievements have made this development possible, the most prominent being the recent introduction of direct electron detection cameras [340-342] and the availability of improved data processing algorithms [343-345].

Cryogenic sample-grid preparation and imaging methods ensure that biological specimens withstand the ultra-high vacuum inside electron microscopes, allowing their investigation while trapped at physiological conditions that conserve the structural arrangement of the biomolecules and reduce the effect of radiation damage [336, 346]. However, these preparation methods have not improved significantly over the last 20 years and have some major drawbacks: A 2-4 µl sample volume is required, and 99.9% of the sample volume is lost during grid preparation, due to an extensive blotting step using filter paper [347]. Furthermore, blotting with filter paper can lead to protein aggregation or denaturation. The current state of the art sample preparation methods are recognized as one of the most significant limitations in cryo-EM [348].

Improved cryo-EM grid preparation strategies that reduce sample consumption are now an essential requirement. A device that combines ink-jet picoliter dispensing with a plunge-freezing apparatus was presented in 2012 [349], and was recently refined by the use of self-blotting grids to allow cryo-grid preparation in combination with ink-jet spotting [350]. Recently, we presented a blotting- and spotting-free method that requires total sample volumes of just a few nanoliters (e.g., 3-20 nl) [333]. It uses a microcapillary to directly ‘write’ the sample on holey carbon EM grids and subsequently vitrifies the deposited liquid, producing thin layers of vitrified specimen in the holes of the carbon film.

In this chapter, we try to benefit from the lossless preparation methods and attempt to integrate microfluidic cell culturing into the single-cell analysis platform (Figure 22A). Regarding neuronal co-culturing devices, the visual proteomics approach of individual cells which were only in contact by their neuronal projections would give insight into several cellular processes, including response to prion-like proteins, susceptibility to PD toxins, and intercellular differences in general.

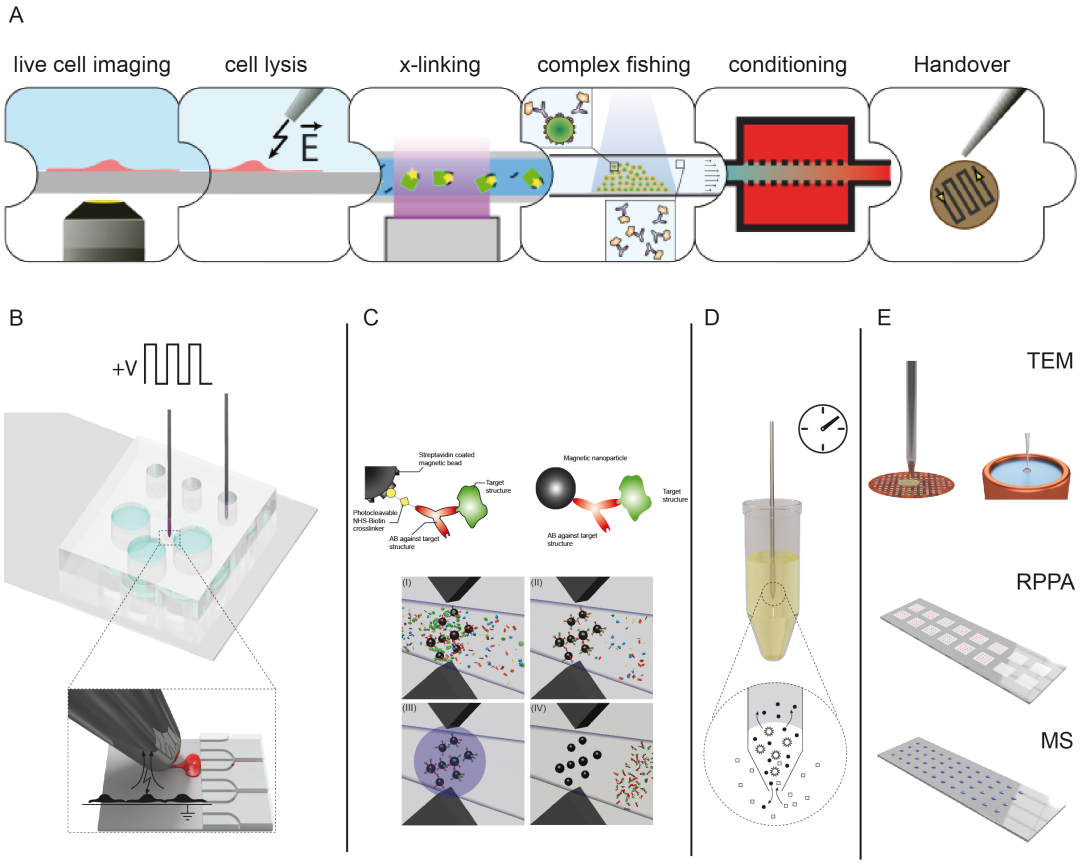

Figure 22. (A) Modular microfluidics pipeline to make small volumes accessible to different analysis methods. New modules can be implemented or skipped. (B) Implementation of co-culturing devices would allow easy transition of the small output volumes and cell lysate. The main instrument includes fluorescence microscopy and a humidity chamber. (C) Antibodies bound to magnetic beads can enrich target proteins from cell lysate. (I) Cell lysate is flushed across the magnetically trapped beads. (II) Target structures can bind and get separated from the other lysate. (III) After washing, UV-light cleaves the antibodies from the beads. (IV) And the target protein is released for further processing. (D) Conditioning, like buffer exchange or negative staining for EM, can be done with nanoliter sample volumes. (E) The sample is handed over to different substrates, depending on the analysis method. As of now, sample preparation for negative stain TEM, cryo-TEM, reverse-phase protein arrays, and mass spectrometry is possible. Reprinted and modified with permission from ref [333, 335]. Copyright (2016) American Chemical Society. Copyright (2017) Creative Commons License 4.0. Panel (A, C) courtesy of Thomas Braun and Claudio Schmidli, C-CINA, University of Basel.

4.2 Results and Discussion

4.2.1 Making Co-Culturing Microfluidics Accessible to Single-Cell Lysis

In the previous chapters 2 and 3, co-cultivation of LUHMES cells was demonstrated and transmission of fibrillar α-syn was observed. The main analysis method therein was fluorescence microscopy, a powerful tool to perform live cell microscopy and track the transmission of possible toxic protein assemblies. However, this technique requires antecedent fluorescent labeling of the protein of interest and no conclusion about structural modifications of the initial seeds can be drawn. With increasing evidence that polymorphisms of α-syn assemblies modify the pathology of synucleinopathies [185], the direct analysis of the seeded fibrils compared to the transmitted fibrils in the second order neurons would give insight to the toxic variants of these proteins (see section 3.2.4).

LUHMES Cells Grown on ITO Slides.

To be able to compare the initial α-syn fibrils with those potent enough to be transmitted, the second order neurons must be lysed and analyzed by EM. Therefore, an integration to the in-house developed single-cell lysis setup for visual analysis by EM is ideal (Figure 22) [334]. This system is designed for electrical lysis of individual adherent cells. It is therefore required to grow LUHMES cells on indium tin oxide (ITO)-coated microscopy slides which act as electrodes. For initial testing of the growth performance on ITO, cells were cultivated on standard glass slides and on ITO glass slides with a PDMS ring as a boundary. LUHMES cells develop a different morphology on ITO-coated glass slides than on normal glass, with both being pre-functionalized with fibronectin and PLO (Supplemental Figure C.2). On ITO, cells don't spread and tend to form larger cell assemblies. In general, LUHMES cells acquire a round morphology on ITO in combination with standard functionalization and often die within 8 days. Growing LUHMES cells on Geltrex®-coated ITO slides, however, only show marginal differences compared to cultivation on uncoated glass slides. This is not surprising, as Geltrex® forms a hydrogel-like layer on the surface, through which cells are not likely to have contact with the ITO coating. Compared to other cell lines like HEK293 cells and BHK cells, the cultivation of LUHMES cells is generally more challenging.

LUHMES Single-Cell Lysis Evaluation.

Before trying to make the co-culturing devices directly accessible to the lysis setup, single-cell lysis experiments were performed on ITO-coated microscopy slides as described in Arnold *et al*. [335]. After LUHMES cells were successfully grown on this substrate, these initial lysis experiments should show if LUHMES cells can be used in a similar way to HEK293 cells with the single-cell instrument setup. As shown in Figure 23A and B, cell

lysate from BHK and HEK293 cells were successfully prepared with a custom-built setup and made accessible for TEM [334, 335]. Compared to those cell lines, LUHMES cells were more challenging to lyse. Because LUHMES cells cannot be passaged at too low confluency, preparing well-separated, healthy cell layers is difficult. It is therefore rare to find an isolated proliferating LUHMES cell (Figure 23C). Additionally, for an efficient lysis, more pulses at a higher amplitude were required, which also affected the surrounding cells. The reason for the lower lysis efficiency is not clear. The Geltrex®-coated surface might be an important factor, as the hydrogel-like surface isolates the cells more from the ITO surface than it does with the PLL coating, as in the case of the BHK and HEK293 cells. It might also be possible that LUHMES cells are of a more resistant nature. Conducting HEK293 lysis experiments on Geltrex®-coated substrates would give more insight into this hypothesis. In the case of differentiated LUHMES cells (Figure 23D), the mentioned issues become more severe. The formed neurite network interferes with the aspiration of the cell lysate, since it detaches easily and can clog the microcapillary. To prevent this, more intense lysis was required to separate the neurites from possible cell debris, or completely isolated cells were required. Unfortunately, preparing isolated single cells is even more difficult with differentiating than with proliferating LUHMES cells, since they start to form clusters. Hypotonic buffers increase the lysis efficiency and weaker electric fields might be used. The morphology of the cells alters as water is forced into the cells (Figure 23D). This, however, might also alter the proteome within a really short timeframe, making parameters difficult to adjust and the experiments less reproducible.

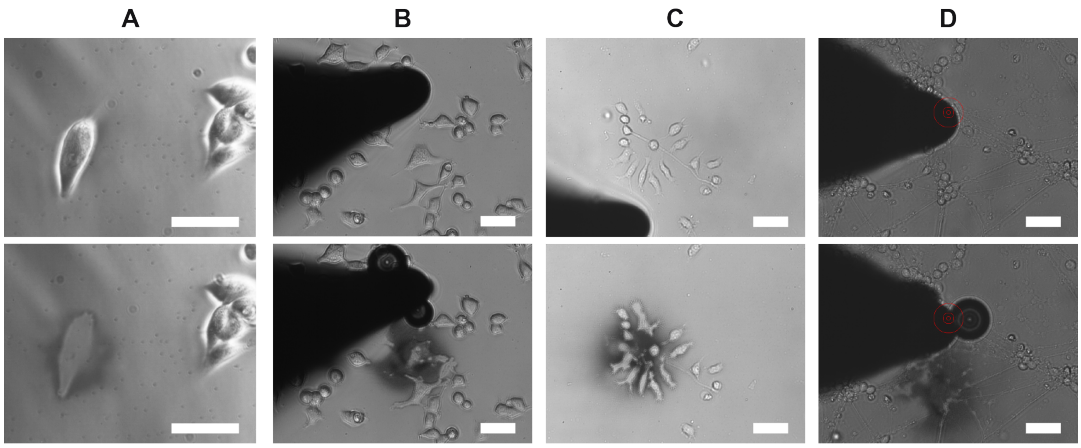

Figure 23. Comparison of different cell types for single-cell lysis. Phase contrast light microscopy images of cells grown on ITO microscopy slides before (top row) and after (bottom row) a sequence of electrical pulses was applied. On B-D, the microcapillary which serves as second electrode is visible from the left side. (A) Adherent BHK21 cells in HEPES buffer. Only a ghost imprint of the cell is left after lysis and aspiration. (B) HEK293 cells before and after lysis. A bubble is formed after electrical pulses were applied. Since cells were grown at high confluence a burst of electrical pulse also affected surrounding cells. (C) Proliferating LUHMES cells were better suited for lysis experiments compared to cells at a high stage of

differentiation (D), as no neurite network is formed yet. LUHMES cells were generally difficult to lyse, likely due to the Geltrex®-coated surface. (D) Differentiated LUHMES cells on Geltrex® in hypotonic PBS buffer. Hypotonic buffer helped for cell lysis. Still LUHMES cells required longer electrical pulses with higher amplitudes for lysis. The formed network became a problem for aspiration and at differentiated stage, isolated cells were difficult to find. Scale bars 20 µm. (A) was reprinted and modified from ref [334]. Copyright (2013) Creative Commons 3.0.

LUHMES Accessibility in Microfluidic Devices.

The design for the co-culturing device offers no open access for a microelectrode to be placed close to the target cells. To the best of our knowledge, there is no PDMS-based microfluidic device which would allow such access while keeping different cell compartments isolated. In principle, the initial PDMS device we produced (Supplemental Figure C.1) would give access to the cell somas in the center of the inlet ports. However, it was not possible to guide neurites of LUHMES cells in this device to other compartments.

The second option would be to lift off the PDMS boundary, exposing the adherent cells in its growth pattern on the glass slides. Since the PDMS is not plasma-bonded to the glass surface, the devices could easily be disassembled as demonstrated in other studies [351]. However, our system required in-channel coating, since the hydrogel-like character of Geltrex® does not allow pre-coating of glass slides before device assembly. In-channel coating made not only the glass surface, but also the PDMS surrounding, a suitable surface for LUHMES cell attachment. To render PDMS resistant to cell adhesion, two polyethylene glycol (PEG)-based surface functionalization methods were tested. PEG is regularly used as an anti-fouling coating and to prevent non-specific biological material binding to surfaces. Regarded as a gold standard, poly-L-lysine PEG copolymers (PLL-g-PEG) in buffered solution are probably the widest and easiest procedure to render a surface non-fouling [352]. Coating of the microfluidics device was solely done on the PDMS replica in order to prevent PLL-g-PEG grafting to the glass surface. After PEG functionalization, devices were prepared as usual for cell experiments. We then labeled the cells with calcein acetoxymethyl ester (calcein-AM) to visualize cell rupture caused by the disassembly of the device. After separation, the glass and PDMS surface were kept humid and were imaged under a fluorescent microscope. Unfortunately, the adherent LUHMES cells preferentially attached to the PDMS walls of the microfluidic channels (Figure 24). The cells did not show any signs of physical stress, as morphology and neurite network corresponded to those of healthy cells, and all cells displayed an even calcein labeling (Figure 24B). These results indicate that Geltrex®-coated PDMS provides better growth conditions than Geltrex®-coated glass, even when LUHMES cells have to grow upside-down. Although microfluidic devices with channel heights of only 10 µm were used in these experiments, the preference to PDMS of the flat cells is still surprising. Apparently,

PLL-PEG coating is not potent enough to avoid the formation of a Geltrex® layer. It is proposed, that Geltrex® forms a sort of a basal lamina, which comprehensively covers the whole area. This hydrogel-like layer is eventually at first repelled by PEG, but with progressive thickening of the hydrogel it stabilizes itself and does not need direct contact with the surface. However, chances are that PLL-PEG surface packing density is not formed highly enough at RT, even after 20h of incubation [353]. Higher incubation temperatures were tried, but at a recommended temperature of 60°C the solution diffuses into the PDMS to a large extent.

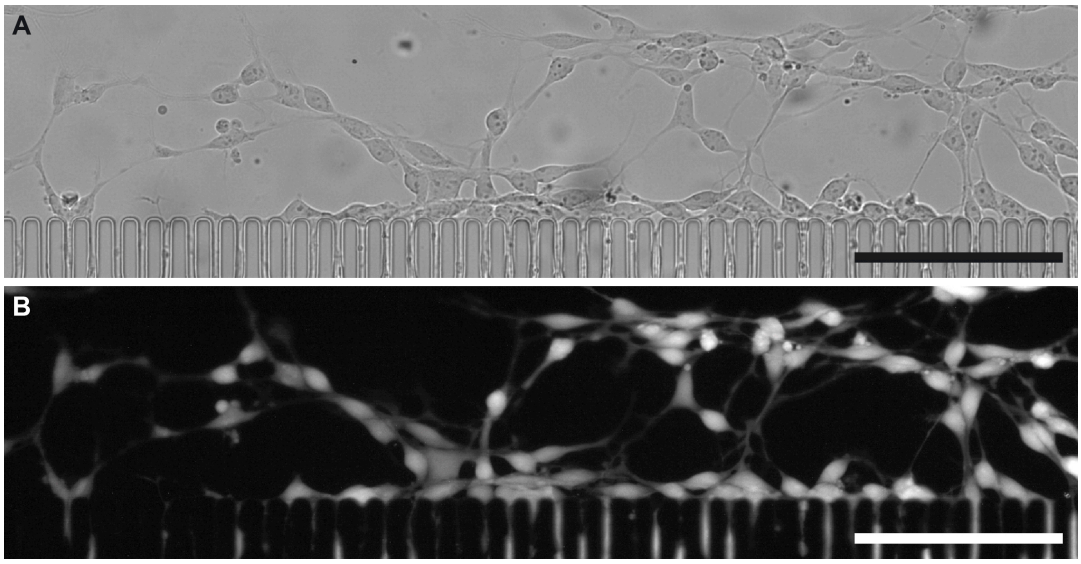

Figure 24. PLL(20)-g[3.5]-PEG(2) functionalized PDMS replica after disassembly from the glass surface. This was not the final design of the co-culturing device and channels had a height of about 10 µm. (A) Bright field light microscopy image of LUHMES cells attaching to the PDMS boundary. (B) The same section as in top panel but cells were labeled with calcein-AM to show that cells detached from the glass surface without being ruptured. Scale bars 100 µm.

The second PEG coating method we tested was not solely based on electrostatic adsorption, but PEG was covalently bound to the PDMS surface via a silane reaction. It was reported that this surface modification of PDMS results in nicer packing density, and reduced hydrophobic recovery renders the surface resistant to nonspecific adsorption for extended periods [354]. Indeed, one week after the coating reaction, surface contact angle measurements indicated a stable PEG-coated surface layer (Figure 25). The control PDMS was subject of the same modification procedure, including oxygen plasma treatment, but with 100% acetone incubation. Although, this plasmaoxydized surface was hydrophilic in the short term, it regained its hydrophobicity after one week (Figure 25A, bottom panel). After standard Geltrex® coating of the modified surface, minor differences in growth

behaviour of LUHMES cells compared to a control surface was found (Figure 25B), but in general, LUHMES cells grew on both surfaces. On pegylated PDMS, the cell monolayer was less continuous with a few areas on which LUHMES cells could not adhere at all (Figure 25B, top panel). This indicates that Geltrex® did not form a continuous, basement membrane-like substrate. Thus, PEG-silane functionalization could improve resistance to adsorption of PDMS, but not significantly change cell adhesion compared to PEG-PLL coating.

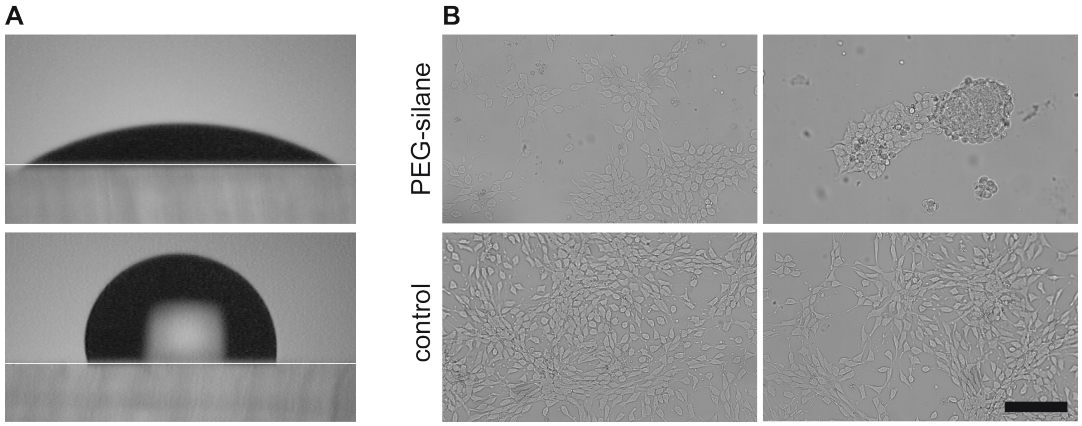

Figure 25. Effect of PDMS surface modification with a PEG functional silane. (A) Surface angle measurements of functionalized PEG. The PEG-coated surface (top panel) is hydrophilic a week after the procedure, whereas the control surface regained a normal hydrophobic characteristic. Both surfaces were initially oxygen plasma treated. (B) LUHMES growing on Geltrex®-coated PDMS, only on minor areas, LUHMES growth performance changes between surface modified (top panel) and control (lower panel) PDMS.

Both approaches, PLL-PEG and PEG-silane coating, did not hinder LUHMES cells to grow on PDMS, mainly due to the excellent coating properties of Geltrex®. Omitting Geltrex® is not an option, as standard fibronectin/PLO coating is not suitable for LUHMES cells in microfluidic devices (Supplemental Figure A.2). We looked for ways to incubate only the glass surface with Geltrex®, leaving the pegylated PDMS exposed to the cell cultures. Due to the proteinous nature of Geltrex®, the coating only worked in fully assembled chips. Incubating only the glass surface required the coating to dry before the PDMS could be assembled, but this destroyed the continuous basement membrane and cells only grew on few clusters. Additionally, to be able to flood the small channels of the device, a liquid with low surface tension had to be applied prior to cell culture media. As we used ethanol for this task, the Geltrex® layer completely denatured.

Also, increasing the height of the microfluidic chambers up to 25 µm did not solve the tendency of LUHMES cells to grow on PDMS. Although most of the cells remained on the

glass surface, this approach would not resolve the problem close to the walls or in the neurite microchannels of the device, with a required height of only 4 µm (Figure 26).

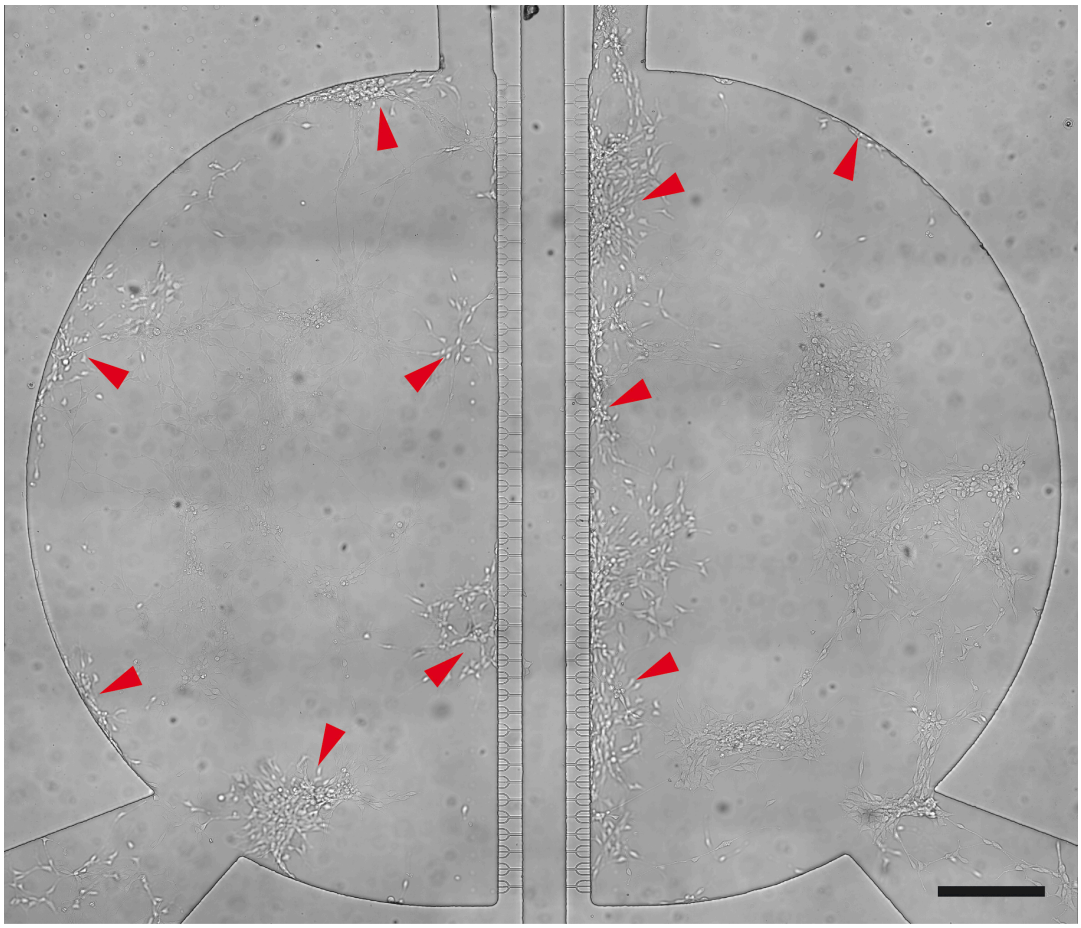

Figure 26. Overview of a whole microfluidic co-culturing device with a height of 25 µm. Red arrowheads show LUHMES cells which do not grow on the glass surface. Scale bar 200 µm.

Overall, making LUHMES cells in co-culturing microfluidic devices accessible to single-cell lysis is challenging, mainly due to the need of Geltrex®-coated surfaces. As Geltrex® forms a thick, extracellular, matrix-like layer it seems to completely isolate all surfaces. Thus, it interfered with the electrical lysis efficiency as the conductive ITO surface was not in close contact with the cells. It also interfered with a usually highly inert PEG surface by simply covering it.

4.2.2 Fishing α-Synuclein Fibrils

The experiments in this section were done in collaboration with Claudio Schmidli, C-CINA, University of Basel.

A trapping module to extract protein complexes from cell lysate is currently being developed for later integration into the single-cell lysis setup (Figure 22C). This is a crucial step in the pipeline, as the identification of protein complexes in crude cell lysate is difficult. Initial experiments with α-syn fibrils were performed to evaluate if α-syn assemblies could be extracted from LUHMES cell lysate.

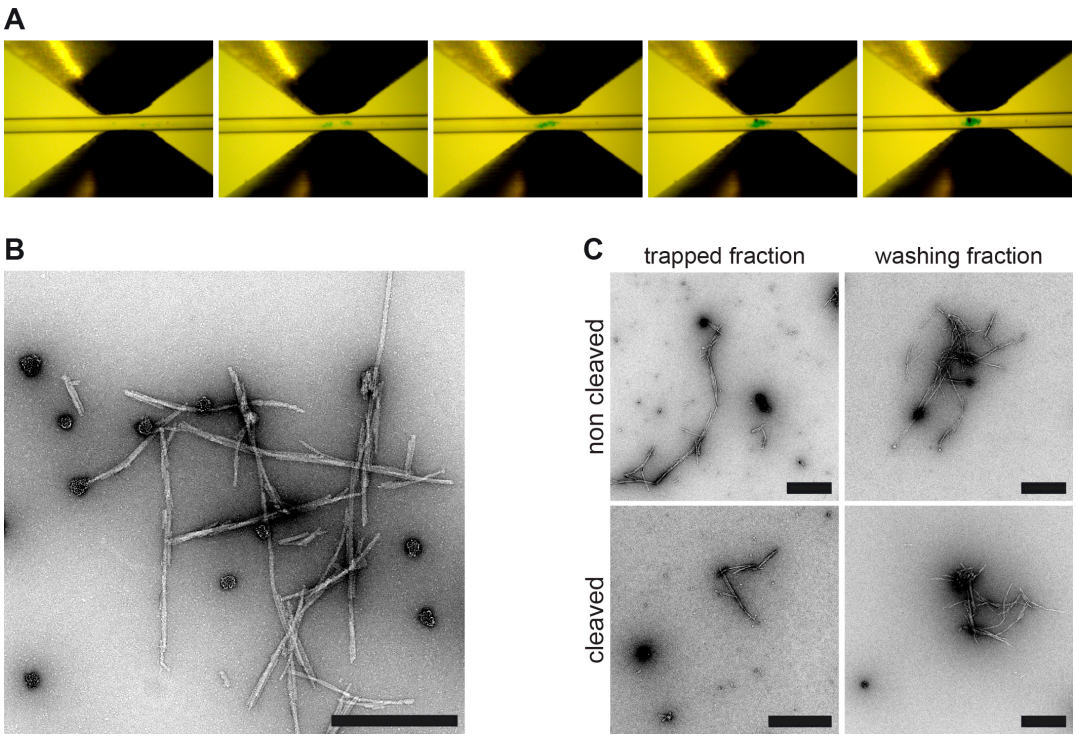

Figure 27. Proof-of-principle study for microfluidics in-line purification of α-syn fibrils. (A) Sequential images (from left to right 10 minutes) of beads being trapped by a magnetic field in a microcapillary, which can be seen by the growing aggregate in the center of the capillary. (B) Starting mixture of streptavidin-coated beads and biotinylated fibrils. From this mixture, biotinylated fibrils should be separated from fibrils which were fluorescently labeled (C). After fibrils were trapped, a washing fraction was collected and then the purified fibrils were released. Scale bars 500 nm.

The working principle is similar to immunoprecipitation. The α-syn fibrils were functionalized with a photo-cleavable biotin and mixed with non-biotinylated fibrils. After incubation with streptavidin coated beads, the solution was loaded to the system via a capillary of 250 µm inner diameter. By passing the magnetic field gradient, the beads, together with bound α-syn fibrils, were trapped (Figure 27A). After flushing PBS across

the trapped particles to remove unbound fibrils, the magnetic trap was switched off to release the purified fibrils bound to nanoparticles. Alternatively, illumination with UV light breaks the photo-cleavable crosslinker from fibrils in the magnetic trap, and isolated α-syn fibrils can be removed from the microcapillary.

As shown in Figure 27B, not all functionalized nanoparticles bound to α-syn fibrils. It is unlikely that there were no biotin binding sites, as an excess of biotin-NHS was used in the reaction. It is possible that there was still free biotin in the sample, which competitively blocked the interaction with α-syn fibrils.

When the fibrils passed the magnetic field, they were efficiently trapped and formed a big cluster (Figure 27C). After the washing step, this cluster did not dissociate even when no magnetic field was applied. Only after harsh pipetting could the sample be made available for TEM. It is possible that streptavidin beads bound to several filaments simultaneously, and filaments themselves tend to form big clusters. This will not be a problem in later applications, as this high number of fibrils will not be available in cell lysate. The washing fraction (Figure 27C, top right panel) still contained bead-decorated fibrils. However, less free nanoparticles were found, indicating that magnetic trapping is not strong enough for bigger protein aggregates with only few beads to withstand the flow.

When the fibrils were separated by UV light, the elute mostly contained bead-free α-syn fibrils, but the concentration was drastically reduced (Figure 27C, bottom panel). Thus, cleaving the photo-crosslinker is not efficient. It is likely that the beads interfere with the incoming light. With lower fibril and bead concentrations, this effect will be reduced.

Overall, the initial microfluidic in-line extraction experiments with α-syn showed potential to isolate α-syn assemblies from cell lysate. The major drawbacks mentioned above, were mostly the result of the high fibril concentrations, leading to a big plaque. However, it remains to be proven if the system is efficient enough to trap a few fibrils from a single-cell lysate.

4.2.3 LUHMES Cells for Reverse-Phase Protein Arrays

The experiments in this section were done in collaboration with Stefan Arnold, C-CINA, University of Basel.

Miniaturization of single-cell protein analysis is crucial regarding the small cell numbers in microfluidics and the stochastic nature of biological processes in a putative homogeneous cell population. As mentioned above, efforts were made to analyze LUHMES cells on a single-cell level by visual proteomics. Since the setup used has a modular organization, the same instrument can be used for sample handover to other analysis techniques (Figure 22E). Instead of writing the sample on an EM grid, it can be spotted on a nitrocellulose or hydrogel-coated glass slides. Upon immunofluorescent labeling, the spots can be analyzed

by a microarray scanner, which is in principle a miniaturized dot-blot platform based on reverse-phase protein (RPPA) technology [355]. Because the integration of co-cultured LUHMES cells in the single-cell lysis setup was not reproducible, we performed RPPA with LUHMES batch lysate.

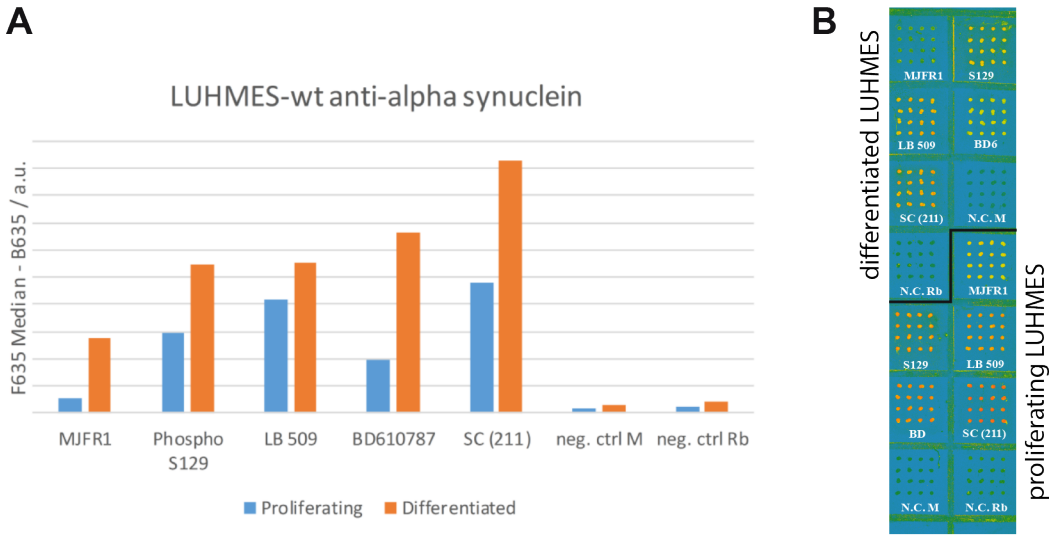

Figure 28. Multiple arrays of 4x4 spots of LUHMES cell lysate was spotted on a hydrogel-coated glass slide and immunofluorescent labeled with various antibodies against α-syn. (A) The signal intensity varied depending on the primary antibody. (B) 10 nl of cell lysate from differentiating LUHMES cells and proliferating LUHMES cells at a concentration of 5 x 10^6 cells/ml was spotted.

A solution was prepared which contained the lysate of 5 million cells per milliliter. By using 10 nl of sample, each spot contained an equal of 50 lysed cells. Multiple arrays of 16 spots were prepared with lysate of proliferating and differentiating LUHMES cells. With an incubation chamber module, each set of 4x4 spots could be immunofluorescent labeled individually. The aim of this initial experiment using LUHMES cells and the miniaturized dot blot application was, (i) testing labeling performance of different antibodies against α-syn, (ii) comparing α-syn expression of proliferating and differentiating LUHMES cells, (iii) estimating the detection limit for α-syn with this method.

The five primary antibodies showed significant differences in labeling efficiencies (Figure 28A). This is not surprising, as all of them target different epitopes. Still, all of them are recommended for detection of α-syn by western blot analysis. The reduced sensitivity might be related to secondary antibody binding, but could not be assessed with this experimental design. Interestingly, the ratio between α-syn signals of lysate from differentiating and proliferating cells is not constant among the antibodies.

The MJFR antibody was demonstrated to be the least efficient, showing the weakest signal. However, regarding the previously mentioned signal ratio, it is the most specific. Given that the lysate of 50 cells was concentrated per spot, it his hardly possible to use this antibody for single-cell lysis detection of α-syn. Although other antibodies were more efficient, the detection of α-syn on low cell numbers is difficult with this technique. When using the same antibodies for immunofluorescent labeling in confocal microscopy, the efficiency does not coincide with the RPPA experiments (Supplemental Figure B.2). In those fixed samples, the BD antibody was the least efficient and the MJFR antibody showed high specificity also for α-syn fibrils. It is normal that some antibodies only work for specific assays.

Consistent with the literature, differentiating LUHMES cells have an upregulated expression of α-syn [305]. The amount of α-syn which we detected in proliferating cells was quite high and, depending on the antibody, almost reached the level of differentiating LUHMES cells. Although we also detected some α-syn in proliferating cells by immunofluorescence labeling and confocal microscopy analysis (chapter 2.2.3), the signals here are clearly too strong. This indicates nonspecific labeling of the cell lysate independent of the state of differentiation. Since there is only a weak signal when the primary antibody was omitted, the nonspecific labeling could be assigned to the primary antibodies.

The miniaturized dot-blot experiments are a promising approach for detection and quantification of proteins. However, in the case of measuring endogenous α-syn with this method, some antibodies already reached the detection limits with 50 cells per spot. It is, therefore, unlikely to detect less abundant proteins on a single-cell level with this technique. Different strategies to enhance the sensitivity have been demonstrated. It was shown that novel nanostructured plasmonic gold substrates enhanced the near-infrared fluorescence signals of protein microarrays up to 100-fold, allowing protein detection in the femtomolar range [356]. Recently, another study, based on surface-enhanced Raman scattering, reported immunoassays also with femtomolar sensitivity [357]. A third approach could make use of signal amplification by sequential incubation of fluorescently labeled secondary antibodies [358]. Such improvements in microarray sensitivity, together with improvements on the single-cell lysis setup to prevent further dilution of the sample, would allow the detection of less abundant proteins down to single cell level.

4.2.4 LUHMES Cells for Liquid Chromatography-Mass Spectrometry

The experiments in this section were performed in collaboration with Stefan Arnold, C-CINA, University of Basel.

Similar to RPPA experiments, LUHMES lysate could be handed over for mass spectrometry (MS). Batch lysate was differently prepared based on a urea buffer and special cyclic olefin copolymer (COC) microscopy slides were used as substrate to spot the samples. Small volumes in the range of 2-18 nl with 2 nl increments were spotted on COC slides. The spots were eluted using a thin layer chromatography interface and fed into the liquid chromatography-MS device, where a targeted mode was used to detect glutamic acid. As seen in Figure 29, the peak area increased linearly with the deposited volume. Theoretically, the smallest spot contained only lysate from 2–3 cells. Although cells were thoroughly rinsed prior to lysis, traces of glutamic acid could still be introduced by the original cell media. Additionally, lysis buffer based on urea is not ideal for mass spectrometry, as it causes a lot of ion suppression. An alternative lysis buffer might further increase the sensitivity. Nevertheless, the experiments showed that with this system, single-cell sensitivity could potentially be reached. With further optimization of the setup and instrumentation, even less abundant metabolites should be detectable at the single-cell level.

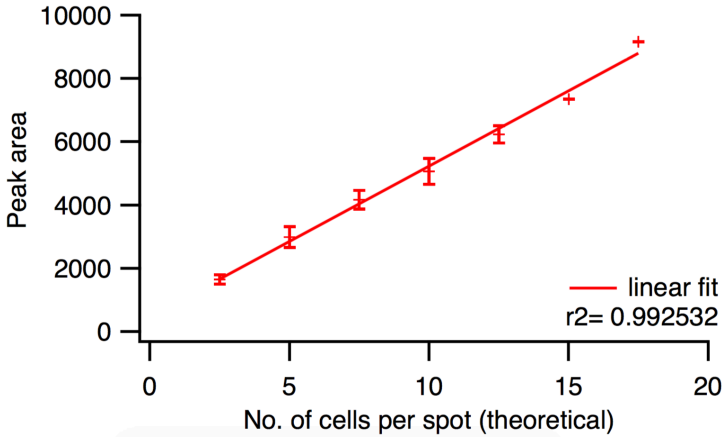

Figure 29. Testing LUHMES batch lysate for glutamic acid. The detected amount increased linearly with the amount of spotted lysate. Reprinted with permission from ref [359].

4.3 Conclusion

Attempts were made to integrate LUHMES co-culturing devices to the in-house developed single-cell lysis instrument. Therefore, initial experiments at several modules of the single-cell proteomic pipeline were performed to test the suitability of LUHMES cells for further integration.

At the beginning of this pipeline, culturing LUHMES cells on conductive surfaces for electrical lysis and access to the isolated cells within a microfluidic chip was required. Growing the cells on ITO was successful. However, slight interference between the growth substrate and electrical lysis was assumed. In general, LUHMES cells are more challenging for single-cell lysis compared to other cell types.

The need for Geltrex® appeared to be an obstacle also for exposing cells by lifting off the PDMS replica. As it forms a continuous basement membrane matrix, it renders most surfaces suitable for culturing LUHMES cells, even when coated against fouling. To overcome this problem, a new surface coating must be found which in the best case can run dry to pretreat only the growth surface, not the PDMS replicas.

Proof-of-concept experiments for inline protein isolation showed, that in principle, α-syn fibrils could be fished from protein lysate. This would be an interesting application for seeded transmission experiments, to isolate transmitted α-syn assemblies from recipient cells and hand over to TEM for strain analysis. However, the low single cell volume and low fibril number compared to a system volume several orders of magnitudes bigger would require an extremely high efficiency.

Finally, RPPA and MS with LUHMES cell lysate revealed that other analysis methods than TEM would be suitable at the end of the single-cell lysis pipeline. However, sensitivity must be increased in both cases to detect proteins and metabolites on a single-cell level.

CHAPTER 5

Correlative Light and Electron Microscopy to Study Mitochondrial Degeneration in Native Environment

This chapter describes the primary evaluation of correlative light and electron microscopy (CLEM) for the in situ study of LUHMES cell organelles. This approach aims for fast sample preparation without inducing changes in neuronal cells.

5.1 Introduction

Differentiated neurons develop a complex arbor of neurites which are responsible for distribution and collection of information. Some axonal projections form extensive networks and connect different brain regions. Increasing evidence indicates a spreading of Lewy pathology based on the prion-like behavior of α-syn, therefore it seems likely that pathological α-syn species undergo a neuron-to-neuron transfer along these axonal projections [280]. Hence, it is crucial to know the neuronal architecture and structure of potential organelles which are involved in this axonal transport.

Electron microscopy offers a unique possibility to study neurons and their connections as its resolution is high enough to structurally characterize cellular contents at nanometer scale. However, due to limited penetration of the electron beam, most conventional EM techniques require sectioning of previously dehydrated and resin-embedded cells or tissue [360]. This harsh chemical procedure can induce changes from their native state. Although there are sophisticated techniques to preserves the physiological state of a biological sample by sectioning vitrified specimens, there might be compression artefacts introduced.

Since the thickness of neurites does not exceed the limits of cryo-EM, several studies demonstrated the growth, vitrification, and visualization of neurons grown directly on EM grids [361-366]. The advantage therein is to preserve the neurites in a close-to-physiological state. Light microscopy can be used to guide the EM search for structures of interest. Advanced CLEM techniques allow automatic position mapping in light

microscopy and spatial correlation to the EM control software, allowing for high throughput and automated image acquisition. Thus, with specific fluorescent labeling, this technique is ideal to study neurite architecture and interaction sites of labeled, internalized α-syn fibrils.

Here, we present the applicability of frozen-hydrated LUHMES cells to direct visualization by light and electron microscopy. As an example, we focused on mitochondrial architecture upon incubation with α-syn fibrils. Additionally, a method is suggested to combine microfluidics co-culturing devices with cryo-EM to study intra-neurite transport.

5.2 Results and Discussion

5.2.1 LUHMES on-Grid Preparation for CLEM

The general steps for growing and vitrifying neurons on EM grids were thoroughly described elsewhere [361]. As we have seen in other applications, preparation of LUHMES cell cultures can be challenging, depending on the required surface (see Chapter 4.2.1). Thus, an adapted protocol for LUHMES cell preparation on EM grids was developed.

Growing LUHMES Cells on EM Grids

Disinfected and glow-discharged gold EM grids were placed in the center of miniaturized Petri dishes which were made from PDMS rings on standard microscopy slides. Unlike other protocols [361], we did not experience any advantages from flame-sterilization as gold grids are highly fragile. The heat often bent the grids and destroyed the holey carbon film. Re-exposure to the environment after glow-discharging was not considered a risk for contamination, as the wells were sterilized with ethanol once the grids were in position. Additionally, we experienced a better coating with glow-discharged grids.

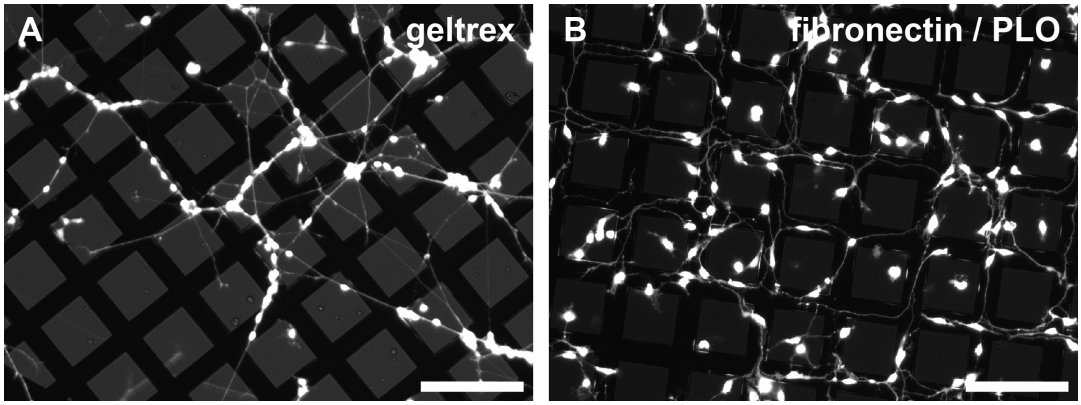

Figure 30. LUHMES cells growing on EM gold grids. (A) Supportive layer of Geltrex® was used. (B) Gold grids were coated with fibronectin and PLO. Scale bar 200 µm.

In general, we faced the same problems with the standard fibronectin/PLO coating as in microfluidic devices or on ITO coated glass, (i) weak spreading and attachment, (ii) slow neurite network formation, (iii) formation of cell aggregates after few days of differentiation, (iv) differentiated cells detached easily, (v) cells did not grow at low cell numbers. Additionally, the formed network was often guided along the bars of the EM grid, where they could not be imaged (Figure 30B). However, Geltrex® coating allowed for plating at lower cell density, and with cells still forming networks without being influenced by grid bars (Figure 30A). Since cell bodies are too thick for cryo-EM, cell density should be kept as low as possible. With Geltrex® coating, it was possible to grow cells at a concentration as low as 200'000 cells/ml. While loading 300 µl of cell suspension in each well, an absolute cell number of about 60'000 cells per well was loaded. Fewer cells often resulted in less stable cell cultures. This cell number exceeds the recommended cell density fourfold [361], which influenced the vitrification quality (see section 5.2.2).

Vitrifying LUHMES Cells on EM Grids

For the plunge freezing process, two commercial vitrification devices were used. At first, a vitrobot (ThermoFisher Scientific, USA) was used in a manual mode, as one-sided manual blotting was preferred. The normal mode of the vitrobot performs a both-sided blotting, which completely ruptured the cell monolayer. Manual blotting from the backside of the grid for 10 seconds gave reproducible results. Unlike described in the literature, using calcium free blotting paper did not make any difference [361].

As second device, a Leica EM GP (Leica Microsystems GmbH, Germany) was used. Although this machine performs one-sided blotting, it resulted in more damaged grid windows than when manually performed. Adjusting the parameters for only slight contact often resulted in not properly blotted grids. Therefore, manual blotting is recommended.

Different types of gold EM grids were tested. Finder grids can assist with correlating light and electron micrographs. Here, only manual correlation based on prominent features was done. This was also possible with normal gold grids. 400 mesh grids appeared to be more stable due to smaller window sizes. However, 200 mesh grids were preferred since the chances of finding neurites in good conditions are enhanced despite increased damage. Similarly, 3.5 µm dimeter holes offered more field of view compared to R2/2 holey carbon films.

5.2.2 Correlative Light and Electron Microscopy

Observing sample grids by light microscopy prior to EM can be of great use to find the regions of interest, to identify labeled targets, and to assess the grid quality. Here, we correlated light micrographs of vitrified and life cell monolayers to EM. In order to make sure that the grid could be correlated to the EM images and to avoid lacking data when parts of the carbon film crack, the whole grid was imaged.

Cryo-Light Microscopy Mapping

To record light microscopy images of frozen grids, an upright light microscope equipped with a cryostage was used. The tongue of the cryoholder was immersed in LN_2 for the grid transfer of up to 9 grids. As no transfer station was available for this type of cryostage, a polystyrene box was modified to fit the grid holder. The transfer process was kept as short as possible to avoid ice contamination.

In bright-field mode of the light microscope, cell bodies were clearly visible through the vitreous ice (Figure 31 top panels). This mode is useful to assess the ice quality. In general, when cells were clearly visible, as in Figure 31A's leftmost windows, the vitreous ice was thin enough for cryo-EM. Thicker ice often displayed cracks, as it can be seen in the other windows. Since we were interested in imaging neurites, exact localization on grids was required. Because neurites were hardly visible in bright field, viable cells were labeled with calcein-AM prior to vitrification. As it can be seen in the lower panel of Figure 31, calcein fluorescence is strong enough for the detection of neurites through vitreous ice. Still, compared to the fluorescent brilliance in liquids (see Figure 30), samples in vitreous ice showed a weaker signal and could appear blurry. This might be explained by quenching effects and increased scattering of light, leading to reduced fluorescence and poor focus. Thus, correlating small or rare features require strong fluorescent labeling.

High cell numbers could impact the ice quality negatively. With many cells on a grid window, the ice was still too thick, even with increased blotting times over 15 s. In this case, over-blotting was hardly possible as water was trapped in close proximity to the cells (Figure D.2.). Ideally, cell bodies grow on grid bars with only neuronal projections crossing the windows. Since the position could not be directed, the cell density was kept as

low as possible. This increased the field of view and decreased the ice thickness. Using concentrations of 100'000 cells per well corrupted the vitrification of the whole grid (Figure 31B). Reducing the cell concentration to 60'000 cells per well resulted in a stable cell monolayer but still made large parts of the grid unusable (Figure 31A). Unfortunately, loading even less cells could lead to a poor neurite network formation. This however, is a trade-off that was considered beneficial for a good ice quality, as the grids were examined and selected before vitrification.

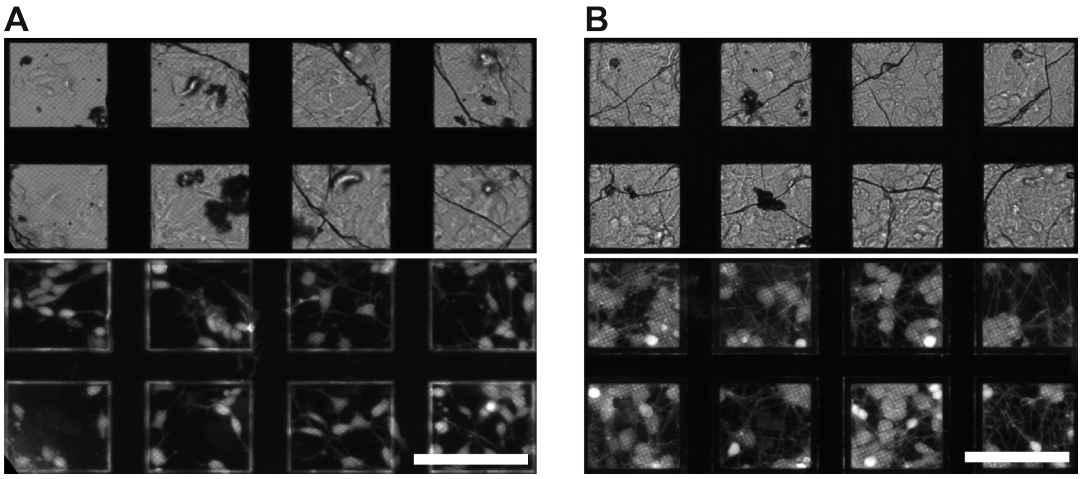

Figure 31. Representative light microscopy images of frozen-hydrated LUHMES cells on EM grids. Upper panels show the grid in bright-field mode and lower panels shows the same cells by fluorescence microscopy of calcein. (A) About 60'000 cells were seeded per well, resulting in a quite high cell density. (B) About 100'000 cells were seeded per well. Cells almost entirely cover the grid, leaving almost no window to perform cryo-EM measurements.

Although examining vitrified grids for latter correlation in cryo-TEM is useful to assess the quality of the frozen grids, it was often favorable to map the grids in liquid state based on the following issues. The used setup increased the risk of ice contamination and defects on the grid with each manipulation step. The intensity of the fluorescent signal and image quality is much better in liquid samples. When mapping was done right before vitrification, the cell state would not change significantly. Overloaded grids, damaged grids, and grids without fluorescent target signal could be discard before vitrification. Possible changes during the freezing process were recognized manually. Additionally, the focus in this study centered on the identification of mitochondrial alteration upon α-syn fibrils incubation. Since both mitochondria and α-syn fibrils were highly abundant, light microscopy mapping was rather to control sample integrity than to localize target features.

However, for future studies using LUHMES cells and CLEM where rare events or cell features should be observed a correlation with frozen grids is beneficial.

Live-Cell Light Microscopy Mapping

Sample preparation for live-cell imaging was nearly identical as for cryo-light microscopy, except for the vitrification step. Additionally, LUHMES cells were incubated with fluorescently labeled α-syn fibrils 24 h prior to imaging. To obtain a whole image at a resolution where fluorescent α-syn fibrils could be correlated to cellular features, several images at high magnification were recorded and later stitched together. Since light microscopy work was done at RT, image acquisition had to be performed fast. Afterwards, grids were immediately frozen to prevent changes in the cellular arrangement. This process could be improved significantly by using live-cell imaging incubation chambers and automatic image mosaicking on the light microscope.

Neurites could clearly be located in bright field images, as it can be seen in the inset of Figure 32A. Therefore, no calcein staining was required. Fluorescent labeled α-syn fibrils were detected mostly co-localizing with cell bodies (Figure 32B). Furthermore, mitochondria were labeled to assist the search in cryo-EM. However, the resolution was not high enough to discriminate individual mitochondria (see Figure 32D). Using higher magnification objectives was not advantageous as imaging time at RT would have increased. In this case, the exact location of mitochondria was irrelevant, as they were highly abundant in neurites.

The light microscopy images were mirrored to match the orientation of EM projections (Figure 32C). When comparing Figure 32 C-E, a neurite can be detected in bright field and fluorescent microscopy and finally by cryo-TEM. Several high magnification micrographs were recorded based on an overview image of this neurite (Figure 32F). There, the positions where the mitochondria were found are labeled with asterisks. Since no mitochondria can be seen on this overview, TEM images were recorded randomly along the neurite.

This basic workflow for CLEM of mitochondria in LUHMES neurites could be substantially reduced. In principle, no correlation would be necessary at all regarding the abundance of mitochondria and α-syn fibrils. Still, for observing the integrity of neurites and co-localizing α-syn fibrils with target cells, light microscopy correlation was maintained. For further studies using LUHMES cells with CLEM, where rare events or organelles should be observed, high resolution light microscopy is indispensable.

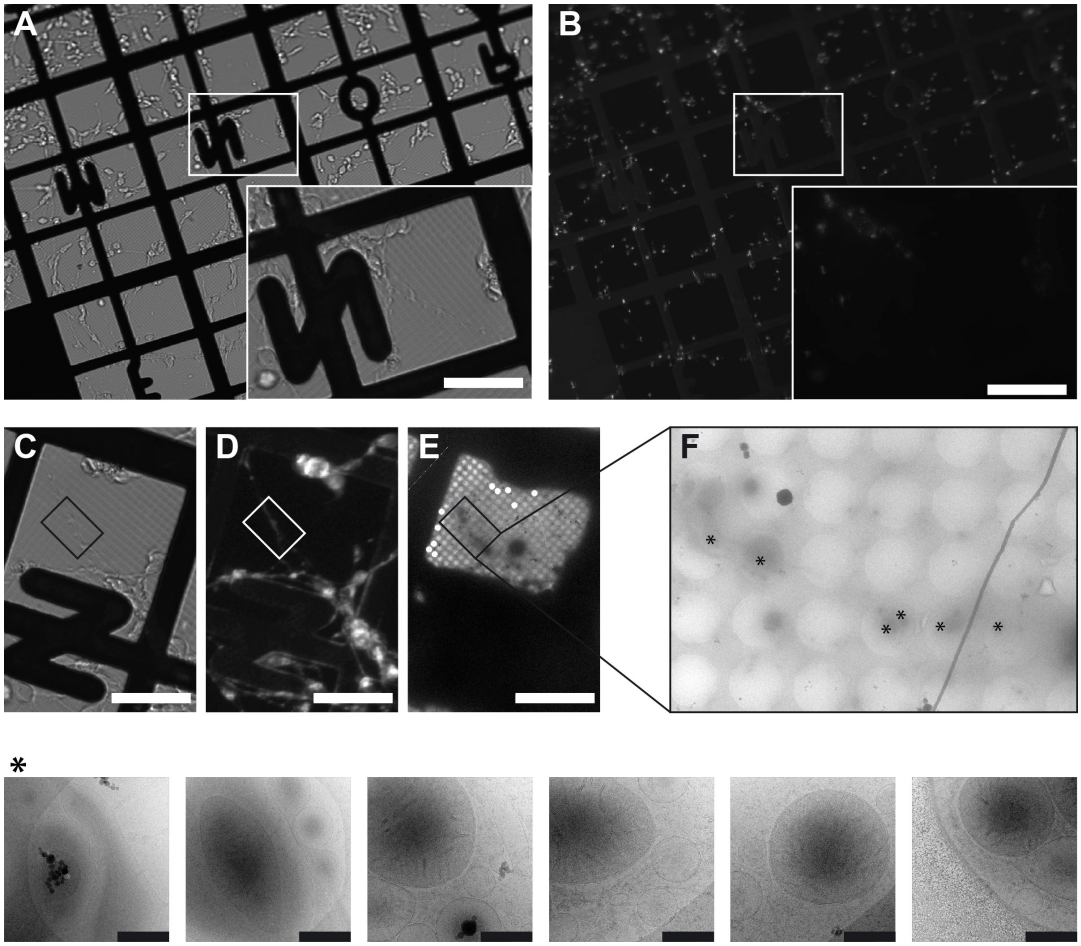

Figure 32. LUHMES cells differentiated for 6 days on EM grid and incubated with 2 µg/ml fluorescent α-syn fibrils 24h prior vitrification. Grids were mapped by light microscopy before vitrification. (A) Bright field image representing parts of an EM finder grid in non-frozen state. Inset was recorded at higher magnification for correlation with cryo-TEM micrographs. (B) Fluorescence microscopy was used to determine co-localization of fluorescent fibrils and cells. (C) Inset of A was mirrored on the horizontal axis. This is necessary for comparison with TEM micrographs, since TEM produces projections of the sample. (D) Fluorescent images of the same section but labeled with mitotracker. (E) Cryo-TEM images correlated to the previously shown light microscopy images. (F) Cryo-TEM images of the neurite of interest, as this neurite labeled positive for mitochondria in D and the connected cell labeled positive for α-syn fibrils in B. (*) Asterisks label the positions where images of mitochondria were recorded (high resolution micrographs follow the same order). White scale bars 50 µm. Black scale bars 500 nm.

5.2.3 α-Syn Fibrils and Mitochondrial Dysfunction

Both mitochondria and α-syn seem to play an important role in the pathogenesis of PD [367]. It was suggested that the mitochondrial dysfunction enhances the formation of misfolded α-syn aggregates [216], although no study was found which supports this theory. On the other hand, several studies suggest a function of α-syn in the control mechanisms of mitochondria [368]. Therefore, a perturbation of this relation is likely to have an effect on mitochondrial function. Overexpression of α-syn affects the normal

function of respiratory chain complexes *in vivo* [369] and induces mitochondrial fragmentation *in vitro* [213, 214]. Additionally, oligomeric [215] and fibrillar species [370] of α-syn could cause mitochondrial impairment. Direct association of α-syn to mitochondrial membrane was demonstrated, but the exact localization remains unclear [371]. According to our knowledge, direct interaction of any internalized α-syn assemblies have not been demonstrated. To study interaction sites of α-syn and its effect on mitochondria shape, the adapted protocol for visualizing mitochondria in dopaminergic LUHMES cell neurites could be of great use.

According to the developed protocol described in the previous section, LUHMES cells were differentiated on gold EM grids. Specifically for the presented data in Figure 33, cells were incubated with 2 µg/ml α-syn fibrils on day 6 of differentiation. Samples were mapped on day 10 of cell differentiation and subsequently vitrified. Fewer fluorescent fibrils were detected after four days of incubation than after 24 h of incubation (compare Figure 33A and Figure 32B). It is possible that fibrils were removed during media exchange or were released as discussed in section 3.2.2. Otherwise, cells did not show any morphological signs for α-syn-induced toxicity (Figure 33A).

Cryo-TEM images were acquired using the Serial EM software [372]. First, an atlas of the EM grid was recorded, based on which regions of interest were correlated manually with the light microscope map, and windows with thin ice were selected. Montages of overlapping images of these windows were prepared (Figure 33C). On these montages, random coordinates along neuronal projections were programmed to automatically record the neurite architecture. Most of the programmed spots contained mitochondria (Figure 33D).

All mitochondria displayed a short, almost round shape (Figure 33D). This type of structure was reported for mitochondria in α-syn overexpressing mammalian cells, whereas wild type cells displayed long and thin mitochondria [214]. Regarding the ultrastructure of the mitochondria, no obvious effect of α-syn fibrils was detected. Cristae are of regular order with narrow intermembrane spaces, which is not consistent to observations in α-syn overexpressing cells, where irregular and enlarged intercristal spaces were observed [151].

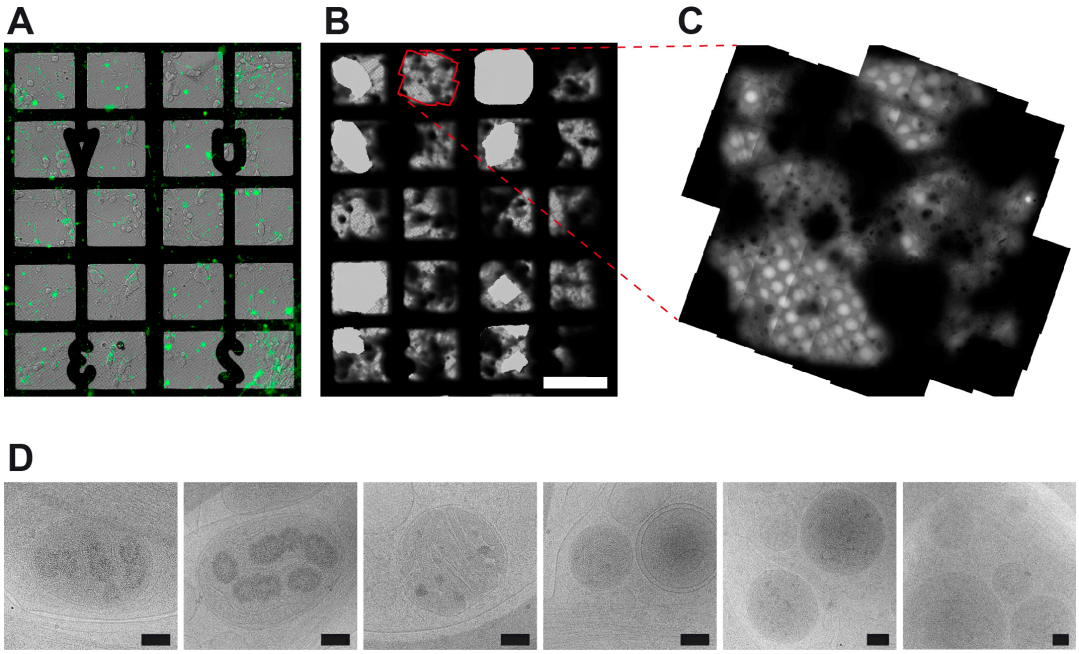

Figure 33. CLEM of LUHMES cells on day 10 of differentiation. Cells were incubated with 2 µg/ml α-syn fibrils for 4 days. (A) Merged bright field and fluorescent image locating the fluorescent seeds on the cells. (B) Same region in cryo-TEM recorded as an atlas in serial-EM. (C) Region of interest recorded as individual images and stitched together with the polygon function of Serial-EM. (D) Mitochondria were imaged on random spots which were selected on the overview map in C. White scale bar 100 µm. Black scale bars 100 nm.

In comparison with earlier structural data (Figure 32 asterisk), the ultrastructure of cristae and the round shape was mostly identical, although the samples from Figure 33 were exposed to α-syn over a longer period. Interestingly, all of the mitochondria with longer α-syn exposure contained electron-dense granules. In samples with 24 h fibril incubation we did not find any intra-mitochondrial granules. Since they appeared in only one condition, a systematic artefact from sample preparation cannot be excluded. It is also possible that granules are formed in older mitochondria, since there were no granules in cells which were vitrified on day 6 of differentiation.

Several conflicting reports exist about the presence of such electron-dense granules. They were considered to be the result of pathological conditions or due to sample preparation artefacts [373]. Some studies exclude a link to cellular stress or toxicity [361]. In general, it is agreed that the granules are involved in the regulation of the ionic environment in mitochondria [373, 374]. Furthermore, it has been reported that the intracellular calcium concentration in old neurons is significantly elevated compared to young neurons [375]. Thus, if granules regulate the internal ionic environment of mitochondria by deposition of the divalent ions in granules, it would explain our data, where granules were only detected in older LUHMES cells. Whether these granules are linked to α-syn toxicity or to age

remains to be systematically tested. But given the above considerations, it is likely the neurons in some of our preparations did not display mitochondrial electron-dense granules as a result of α-syn toxicity.

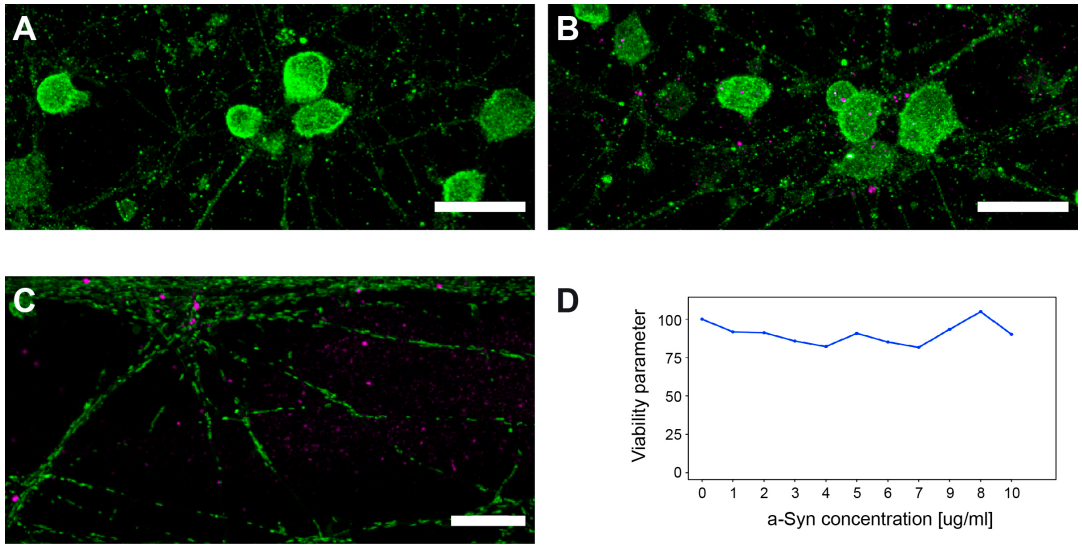

Figure 34. Influence of α-syn fibrils on mitochondria in LUHMES cell cultures. Seeds were applied on day 2 of differentiation and cells were fixed on day 10 of differentiation. Mitochondria are labeled in green, seeds are labeled in magenta. (A) LUHMES cells without incubation of α-syn fibrils. (B) Fibrils are incubated on day 2 of differentiation. (C) LUHMES cells were cultivated in a co-culturing device and seeds were applied to the central channels. Mitochondria were labeled with mitotracker. (D) Cell viability test of LUHMES cells incubated to different seed concentrations. Scale bars 20 µm

Confocal microscopy studies with LUHMES cells prepared under the same conditions as for the CLEM studies did not reveal any effect of α-syn fibrils on mitochondrial morphology. Immunofluorescent labeled mitochondria in fixed samples display the same pattern in LUHMES cells which were incubated with fibrils and in the control sample (Figure 34A and B). Unlike the reported tubular and connected pattern of mitochondria in wild type mammalian cells [214], the mitochondria appeared small, in a punctuated pattern. This would be consistent with the round shape of the mitochondria in the cryo-TEM data (Figure 33D). Interestingly, when mitochondria in live cells were labeled using mitotracker, the fixed sample showed a tubular mitochondrial pattern (Figure 34C). Additionally, using both labeling methods, α-syn fibrils did not co-localize with mitochondria (Figure 34B and C). It has been shown in many experimental models that monomeric α-syn is localized to mitochondria [371]. The direct interaction of bigger α-syn assemblies was not demonstrated. It remains unclear how α-syn fibrils might indirectly affect mitochondria.

Additionally, we tested what concentration of α-syn fibrils is needed to induce a substantial toxic effect in LUHMES cells. The resazurin assay is particularly interesting in this matter, as it gives us information about cell viability based on dehydrogenase activity in mitochondria. Therefore, it also provides insight into mitochondrial respiratory function. Here, we did not observe any significant decrease in reduction of resazurin, even at high α-syn fibril concentrations (Figure 34D). This indicates that neither did cells die from α-syn toxicity nor was there a reduced mitochondrial activity. Several controversial reports about α-syn fibril toxicity exist. In some, only the oligomeric, not monomeric or fibrilar form of α-syn, can induce mitochondrial dysfunction which is consistent with our results [215]. Other studies reported mitochondrial impairment in cell cultures as a direct effect of α-syn fibrils [370]. Either way, mitochondrial changes do not inevitably lead to detectable mitochondrial dysfunction [214]. Therefore, absence of overt cellular toxicity in LUHMES cells does not necessarily conclude that α-syn fibrils have no effect in cellular integrity.

The results from this chapter are in agreement with observations from chapter 2 and 3, where no obvious toxic effect from α-syn fibrils was observed. Supported with cell viability tests and mitochondrial ultrastructure, most seeding experiments indicate that LUHMES cells are not susceptible to α-syn pathology of this strain of fibrils.

5.2.4 Microfluidics Co-Culturing on EM Grids

With the development of automated high-resolution CLEM, sample preparation remains the main bottleneck in this technique. Regarding the preparation of LUHMES cells on EM grids, the main problem is the relatively high cell number which is required to grow a healthy monolayer. This conflicts with the need in cryo-TEM for a thin ice layer, since a continuous cell monolayer interferes with the vitrification. As only cell bodies are an obstacle in this method, a separation from neurites and somas would be beneficial. Initial evaluation of this concept was done, combining microfluidic co-culturing devices with CLEM.

PDMS replicas for the co-culturing devices were prepared as described previously (chapter 2.2.1) Instead of assembling the devices, replicas were bisected along the central channel, dividing the two cell-growth chambers in separate replicas. A pair of those were placed in Petri dishes with enough distance to place a gold grid in the central space (Figure 35). From this point, devices were processed according to standard LUHMES cell culturing in microfluidic devices. No difference in growth behavior between the normal and these bisected devices were observed. Indeed, this application even offers a few advantages. As there is no central channel, the big space between the two halves had to be filled with cell media, which meant the whole space in the dish around the device was filled with media. In this huge excess of media, cells could easily survive for 4 days without media change.

For seed transfer experiments in anterograde direction, Petri dishes must be filled to at least the same level as the inlet ports of the growth chambers, otherwise seed transport would occur with the stream through the neurite channels. This high level of media often detached the devices due to good buoyance of PDMS and weak interaction with plastic Petri dishes. To perform experiments which don't allow a stream from the growth pool to the central space, the PDMS needed to be weighted.

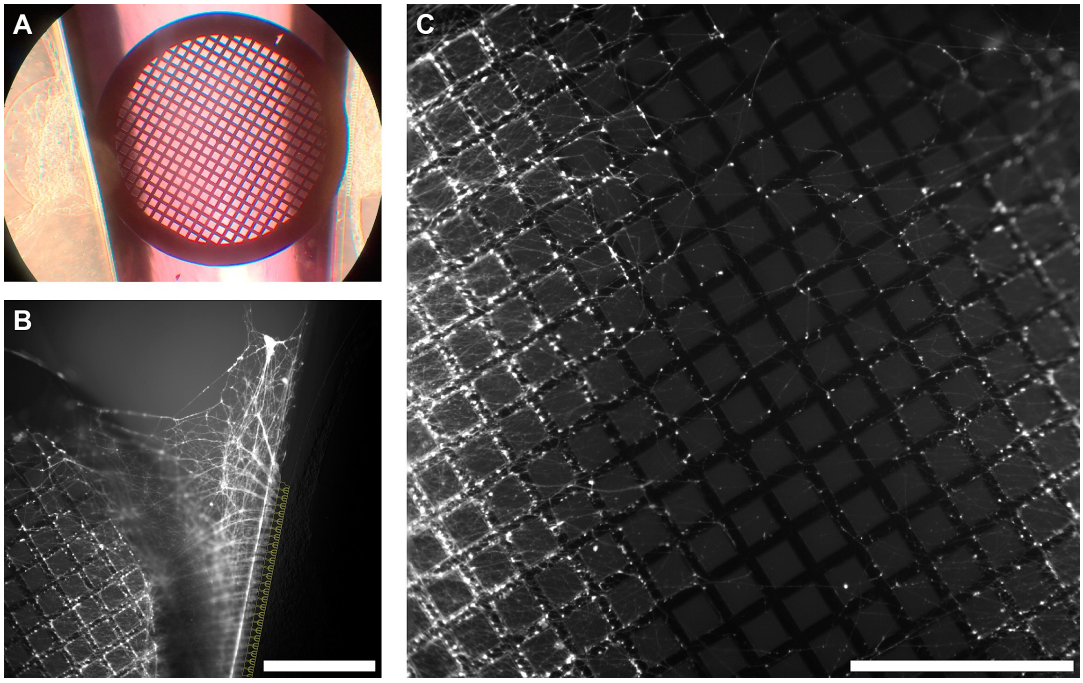

Figure 35. Combining microfluidics and CLEM. (A) An EM holey carbon gold grid (ø 3.05 mm) was place in-between a bisected microfluidics co-culturing chip. (B) Fluorescence microscopy image of neurites growing through the microchannels onto the gold grid. (C) Neurites from individually cultured LUHMES cells meet at the center of a gold grid. Scale bars 0.5 mm.

As in normal co-culturing devices, neurites begin to grow through the microchannels after three days of differentiation. Grids could also be inserted at this point, when it is certain the cells are growing regularly. Unfortunately, as gold grids have a thickness of 20 µm and can be slightly bent, neurites mostly grow underneath the grid (Figure 35B). Interestingly, neurites didn't stick to the Geltrex®-coated plastic surface, but instead they formed a dense network upside-down on the bottom side of the gold grids. Thus, EM grids should be positioned upside-down.

To have enough neurites in the field of view for cryo-TEM, neurites must push towards the center. With exactly aligned PDMS replicas and EM grids, neurites still have to grow over a distance of 1.5 mm. However, after 10 days of differentiation with a high cell number in

the growth pools, there were enough neurites in the central region of the grid, with some even crossing the center (Figure 35B). This then even allows the study of direct interaction sites of two different cell populations.

The vitrification of the sample also follows the presented CLEM procedures, whereas neurites could be imaged on live-cells or after the vitrification. It was difficult to mount the grid on the tweezer, while the grid was pushed around in the dish. With the first contact between the grid and the tweezer, the neurites get injured and crush. From this moment, the fine structure of the neurites start to change. Since this is not a problem when cells are grown together with their neurites on the grid, we thought that this new method would be less physiological. However, the time between first contact with the grid and final plunge freezing can be below 30 seconds. Time for the part distal to the injury to degenerate can only be estimated. It was reported, that after crush trauma, Wallerian degeneration starts in the distal part of the neurites. The progressive anterograde degeneration begins usually within 24 hours [376]. Mitochondrial swelling and disintegration, and ER degradation are early changes, followed by microtubule depolymerization. However, it was shown that both ends die back within 30 min for several hundred micrometers from the site of injury [377]. This acute degeneration is similar to Wallerian degeneration but affects both ends.

Taking this into account, parts of the neurites which reach the center of the grid should still be intact after hours. But to avoid taking chances, vitrification of the grid should be done rapidly after first contact with the tweezer, especially since the described degeneration processes were studied *in vivo*, whereas neurites in cell cultures might respond differently. However, even if mounting the grid can take several seconds, and subsequent blotting time takes 10 seconds, the whole plunge freezing process can be managed within 30 seconds. Thus, neurites at grid center still should display a physiological neurite architecture.

Overall, this technique offers several advantages. Neurites and soma can be treated independently, which allows experiments on neuronal transport of α-syn fibrils. Since neurites can span half of the grids, projections of two independently-treated cell populations can be studied. No large cell bodies grow on the grid which would interfere with the vitrification. Thus, sample preparation should be more reproducible, and fewer expensive gold grids would be required. In contrast to on-grid cell cultivation, grids can be positioned when neurites start to grow through the channels. This again reduces the loss of grids due to poor cell conditions. In general, grids should display a cleaner background since secreted vesicles, apoptotic cell debris, and other cellular residuals mostly remain in the microfluidic chambers.

5.3 Conclusion

Here we have presented a protocol of how LUHMES cells can successfully be made available for CLEM studies of neurites in near-physiological state. Initial findings indicated that α-syn fibrils do not induce a significant reaction in these cells. In general, LUHMES cells do not seem to be susceptible to fibrils.

The main problem in sample preparation was poor vitrified ice due to a high number of cell bodies on the EM grids. To avoid this problem, we presented initial results of a concept where only neurites grow on the grids, by using microfluidic co-culturing devices.

With the development of automatic correlation between light microscopy and EM, automatic image acquisition in cryo-TEM, and sophisticated microscopes to record high-resolution images, many steps were taken already for high throughput experimentations. However, there is plenty of space for optimization in the CLEM process. Here, the protocol would profit further from automatic mapping in light microscopy with automatic z-stack recording at high magnification and image stitching.

CHAPTER 6

General Conclusion and Outlook

The overall aim of this thesis was the co-cultivation of LUHMES cells in microfluidic devices as a minimalistic *in vitro* model system for PD-related research on the prion-like spreading of α-syn. As a far-reaching aim, a flawless integration of several single-cell lysate analysis techniques and of CLEM was pursued.

First, LUHMES cell cultures were established. The decision to use these cells was based on the lack of alternative stable, dopaminergic neuronal cells of human origin, and on the suitability of LUHMES cells as a model for PD-related studies [301]. This human cell line was developed to fill the gap between animal models, where often the disease phenotype of PD is missing, and cellular models, which often don't meet the dopaminergic requirements, or are not of human origin. Since the creation of LUHMES cells in 2005 [298], several studies have used this cell model to reveal DA-related cell death mechanisms, often due their suitability for MPP+ toxin-induced neurodegeneration [300, 305, 378], and LUHMES cells were well-characterized in this process [301]. However, so far, no studies were published using LUHMES cells as a model for seeded aggregation and transmission of α-syn. Therefore, LUHMES cells needed to be characterized upon incubation with α-syn fibrils. Uptake and release of extracellularly added fibrils was observed by confocal microscopy. The internalization of fibrils in LUHMES cells is a process which starts immediately after incubation and does not reach saturation within 24 h. Most of the α-syn fibrils thereby remain on the cell surface. Furthermore, extracellular added fibrils seem to form aggregates, inside the cell and on the cell membrane. Unlike as reported in several studies using other cell lines, we could not observe any seeded aggregation of endogenous α-syn [253, 379]. Regarding release, there were some indications that α-syn fibrils are secreted from LUHMES cells, although it seems that most fibrils are released after cell death. Degradation of α-syn fibrils by endosome-lysosome pathways could not be verified since corresponding markers did not co-localize with seeds. While studying seed propagation of α-syn, we continuously prolonged the cultivation

times of adherent LUHMES cells for up to 20 days of differentiation. Compared to the reported 12 days of differentiation [301], a further increase of some neurological markers was detected, making LUHMES cells at longer differentiation times a more complete dopaminergic model to study PD. Additionally, we found an improved differentiation within shorter time when using a different surface coating.

In the second step a co-culturing microfluidic device was developed to study the transmission of α-syn through neuronal projections – a further key element of the prion-like spreading hypothesis in PD. In general, fluidic separation from axons and soma of neuronal cells is an established technique. Although attempts to cultivate LUHMES cells in microfluidic devices were made in the past [312], so far no published data is available on this matter. To improve growth and neurite guidance of LUHMES cells in PDMS-on-glass devices, the cultivation protocol and surface coating were heuristically adapted. The design of the microfluidic device was improved for stable cell cultivation with no cross-contamination of different cell populations. The developed devices were used to study intra-neurite transmission of α-syn fibrils, which seems to be less efficient in LUHMES cells compared to other cell lines. In general, LUHMES cells seem only slightly susceptible to α-syn pathology, which does not make them a bad model system, as many experimental parameters, including α-syn strains, seed concentration, and cellular heterogeneity need to be clarified by further testing. As the efficiency of uptake and transmission is only low, it is even more important to make microfluidics devices accessible to other analysis techniques which allow for detection of rare events.

On these grounds, attempts to connect microfluidic co-culturing devices with a single-cell lysis device were made. This instrument has a modular structure, which allows the integration of different modules at several steps of the pipeline, and can handover the final sample to several analysis methods, including cryo-TEM, MS, and RPPA. The initial sample-loading can be done by directly lysing and aspirating single cells. Therefore, LUHMES cells were successfully grown on ITO slides and provided for electrical lysis, which is the main task for further processing at a single-cell level. Direct lysis from microfluidic chips was evaluated, and failed mainly due to the need for adherent LUHMES cells to grow on Geltrex®-coated surfaces. Further steps in the single-cell lysis pipeline were successfully tested, particularly the handover to complementary single-cell analysis methods like RPPA and MS. These results demonstrated the feasibility of single-cell analysis with LUHMES cells, although more work will be necessary for a flawless integration of co-culturing devices.

In the final part, protocols were established to visualize LUHMES cell neurites by CLEM. With the importance of mitochondria degeneration in PD in mind, correlating light microscopy and EM with LUHMES cells can be of great use in studying the influence of

α-syn to dopaminergic cells. An improved cultivation procedure was tested which combines LUHMES co-cultivation with CLEM, thereby reducing the damage caused by a cell monolayer to the holey carbon EM grids, and allowing the study of seed transmission through neurites.

Overall, many methods were presented in this thesis, with all of them involving the cultivation of a stable LUHMES cell monolayer. The benefits of stronger adhesion to a particular substrate would be high, especially in single cell lysis experiments to avoid aspirating cell debris, and in CLEM to avoid altering the morphology of the neuronal network during vitrification. But also for longer differentiation times, LUHMES cells need an improved substrate to avoid detachment during washing steps. By using Geltrex® an improvement was made in this respect. Additionally, the use of Geltrex® demonstrated that LUHMES cells might be able to differentiate into a more complete neuronal cell line. We showed that a monolayer growth of up to 20 days is possible and increased SP levels were detected. Development of better growth substrate and media composition would be necessary for a complete polarization of this cell line. To this effect, co-cultivation of LUHMES cells with astrocytes, and long-term cultivation in a 3D model was already demonstrated [307, 310]. Regarding the prion-like spreading of α-syn, a better differentiated and more mature cell culture would possibly lead to different behavior of the cells and a more developed α-syn pathology. Thus, it might be possible to detect endogenous α-syn template recruitment.

Seeding experiments can be done with an endless number of possibilities, using different seeds to study strain dependence of spreading, using cells at various stages of differentiation to study cell development dependence, and using co-cultivation models with other cell types to study protective mechanisms of neurodegeneration. Live-cell fluorescent microscopy at high resolution could improve these experiments. Real-time analysis of seed uptake, release, and transmission would give important insights into the mechanisms of prion-like spreading. Especially for assessing the influence of different strains, a fluorescent analysis of the individual cells is fundamental, e.g. to evaluate the cell's condition with respect to the selective vulnerability theory.

Direct implementation of the microfluidic co-culturing device into the single-cell lysis setup would allow a whole new analysis perspective for α-syn fibrils. Initial seeds could be compared directly to seeds which were isolated from second order neurons. Handover to EM can be used to directly characterize α-syn fibril or oligomer structure and possible seeding parameters, as transmission efficiency and toxicity can be correlated in combination with live-cell microcopy.

Future improvements will also involve the seeded α-syn fibril localization in a native neuron by CLEM. Electron tomography can give exact structural data of organelles and the

position of α-syn fibrils. Improved cultivation on EM grids in combination with co-cultivation microfluidics gives a higher yield of proper vitrified grids. Furthermore, advanced cryo-light microscopy will allow fast and automatic correlation with cryo-TEM image recording. Especially with experiments where only rare events take place, light microscopy is crucial to aid the search for exact locations in EM. Additionally, evaluation of fluorescent markers for dopaminergic cells might give insights into the selective vulnerability of certain cells which then can be analyzed by cryo-EM.

Finally, microfluidic devices can be highly automated, controlling the flow rate, time point of media exchange, or addition of seeds. Additionally, a better fluidic separation over long incubation times would be guaranteed, as no hydrostatic pressure equalization would invert the flow.

This thesis has clearly demonstrated that LUHMES cells can be stably cultivated in a microfluidics co-culturing device and can be used to study the prion-like spreading of α-syn.

Closing remarks

The initial goal of this project was the assessment of different α-syn fibrils regarding their transfer efficiency to second order neurons by comparing the structure of initial seeds and those transmitted. When I started my Ph.D. no cell cultures were maintained, no clean-room was accessible, no α-syn fibrils were generated, and no cryo-CLEM was performed. Starting from scratch, each technique needed to be established in order to finally realize that the bottleneck is, as so often, the challenges that lie in cell cultures. However, all the methodologies are now available and can be used to tackle questions in the field of Parkinson's disease.

CHAPTER 7

Experimental Section

In this chapter, all experimental procedures which were used in this thesis are described. Some were reproduced and modified with permission from the corresponding references [334, 335].

LUHMES Cell Maintenance Standard Procedure. The LUHMES cell line was kindly provided by Prof. Dr. Marcel Leist (University of Konstanz, Germany). Apart from the cells in microfluidic devices, cell cultivation and differentiation was performed following the original protocol [301]. Only Nunclon^{TM} Delta treated cell culture flasks and multi-well plates (Thermo Fisher Scientific, USA) were used. For confocal microscopy cell preparation, 0.18 mm thick glass slides were additionally added into 12-well plates (Mänzel-Gläser, Thermo Fisher Scientific). All dishes were pre-coated with 50 µg/mL poly-L-ornithine (PLO, Sigma-Aldrich) and 1 µg/mL fibronectin (Sigma-Aldrich) in culture grade H_2O (Sigma-Aldrich) overnight. Prior cell transfer coated dishes were rinsed twice in PBS (Sigma-Aldrich) and air-dried. For maintenance in proliferation state, adherent cell monolayer was briefly rinsed with PBS- and then dissociated with 0.05% trypsin-EDTA solution (Thermo Fisher Scientific). After 3 min incubation, trypsin was deactivated with 10 ml Advanced DMEM/F-12, pelleted at 100 rcf for 5 min and resuspended in proliferation media. Proliferation media was freshly prepared with Advanced DMEM/F-12 containing 2mM Glutamax^{TM} supplement (Sigma-Aldrich), 1 x N2 supplement (Gibco) and 40 ng/ml recombinant human FGF basic (R&D systems). To keep cells in proliferating state they were passaged 1:5 every second day or when they reached 80% confluency. For pre-differentiation, 2 x 10^6 proliferating LUHMES cells were splitted in a T-25 flask containing proliferation media. After one day, differentiation was started by media exchange to differentiation media consisting of Advanced DMEM/F-12 supplemented with 2mM Glutamax^{TM}, 1 x N2 supplement, 1 µg/mL tetracycline (Sigma-Aldrich), 1 mM dibutyryl cAMP (Sigma-Aldrich) and 2 ng/mL recombinant human GDNF

(R&D Systems). After two days of differentiation cells were trypsinized, pelleted at 100 rcf for 5 min, and resuspended in differentiation media. For further differentiation in 12-well plates, cells were diluted to 4 x 10^5 cells/ml and 1 ml was added per well.

Immunofluorescence Labeling for Confocal Microscopy. The labeling procedure was the same for cells grown in 12-well plates and in microfluidic devices. Cell monolayer was washed three times with prewarmed (37°C) PBS+ and fixed in 4% PFA (Sigma-Aldrich) for 30 minutes at RT. After washing three times in Modified Hank's buffer (MHB; Ca^{2+}-free, 137 mM NaCl, 5 mM KCl, 1.1 mM Na_2HPO_4 x 12 H_2O, 0.4 mM $KHPO_4$, 4 mM $NaHCO_3$, 5.5 mM glucose, 2mM MgCl, 2mM EGTA, 5 mM MES, pH 6.5) plates were sealed with parafilm and stored at 4°C until further use.

Incubation with the primary antibodies was done for 2 h after 10 min cell permeabilization with 0.25 % Triton X-100 in MHB. After 2 x 10 min washing in cell buffer secondary antibodies were applied for 2h. In some cases, cells were stained with DAPI or phalloidin after these steps. After 3 x 10 min washing in MHB, glass coverslips where embedded in mowiol and dried for 24 h before imaging. Due to narrow channels in microfluidic devices, a mounting media with lower viscosity was needed. We used either ProLong™ Diamond Antifade Mountant (Thermo Fisher Scientific) or ProLong™ Gold Antifade Mountant (Thermo Fisher Scientific). For confocal microscopy, a Leica SPE was used.

Antibodies for Immunofluorescence and WB. The following commercial available primary antibodies were used in this thesis:

Antigen	Name	Supplier	Dilution CLSM	Dilution WB	Species
α-syn (AA 120-202)	SC211	Santa Cruz Biotechnology	1:200	1:1000	mouse
α-syn (AA 118-123)	MJFR1	Abcam	1:150	1:1000	rabbit
α-syn (AA 115-122)	LB509	abcam	1:500	1:2000	mouse
α-syn (AA 15-123)	BD	BD Bioscience	1:500	1:2000	mouse
α-syn	S129	abcam	1:200	1:1000	rabbit
β-III-tubulin	TUJ	Sigma-Aldrich	1:500	-	rabbit
synaptophysin	SP	Sigma-Aldrich	1:300	1:500	mouse
VDAC1	VDAC	Abcam	1:500	-	mouse
LAMP1	LAMP1	Abcam	1:300	-	rabbit
LAMP2 H4B4	LAMP2	Abcam	1:400	-	mouse
Thyroxin hydroxylase	TH	Santa Cruz Biotechnology	1:500	-	rabbit

Microfluidic Co-Culturing Device Production. The design for the microfluidic device was adapted from Dinh *et al. 2013* [311] and allows stable LUHMES cell growth and neurite connections between two cell populations, which can be handled independently. The microfluidic devices were prepared by replica molding with PDMS (Sylgard 184, Down Corning) on a multi-height SU-8 master on a silicon waver, allowing two different channel depths. Therefore, the three-way microchannels from a chrome mask (Delta Mask, the Netherlands) were exposed on a ~4 µm thick SU8-3005 (MicroChem) layer. A second layer of SU8-3025 (MicroChem) was then additionally spin coated to a depth of ~30 µm on which the big flow channels were exposed from a foil mask (Selba S.A, Switzerland). In the PDMS replicas (Sylgard 184, Down Corning) 3 mm in diameter inlet ports and 1.5 mm in diameter outlet ports were made with biopsy punches (Harris Uni-Core™). Replicas were then sonicated in ethanol for 10 minutes, thoroughly rinsed with deionized water, air dried and assembled with thin microscopy cover slips to the final microfluidic device. The glass slides need to be suitable for confocal microscopy.

Microfluidic Device Testing. Due to possible production variances, all devices were tested for fluidic isolation. Therefore, equal volumes of PBS were applied to the inlet ports and fluorescent dye (sulforhodamine B, 20 µM) was alternately supplemented in the liquid of one port till possible cross-contaminations from the cell-growth chambers could be excluded. After inlet ports were filled the devices were stored in cell humidity chambers for two days and monitored frequently in a fluorescent microscope (Zeiss Axio Imager M2).

LUHMES Cell Cultures in Microfluidic Devices. Microfluidic co-culturing devices were coated with Geltrex® (Thermo Fischer Scientific) according to producer's protocol at a dilution of 1/100 in PBS+. Assembled devices were flushed with EtOH absolute and PBS+ before Geltrex® in PBS was applied for 1 hour at 37°C. Neuronal differentiation in microfluidic devices did not require a pre-differentiation of LUHMES cells. Proliferating cells were trypsinized, centrifuged and resuspended in differentiation media at a concentration of 3 x 10^6 cells/ml. 20 µl cell suspension was loaded into the flanking inlets of the microfluidic device and slight vacuum with a cell culture aspiration system at -400 mbar compared to atmospheric pressure (vacusafe, integra bioscience) was applied at the outlet ports. Afterwards, inlet ports where washed with PBS+ and filled with 50 µl differentiation media. Microfluidic devices were placed in rectangular 4-well plates with one well being filled with water and filter paper to prevent inlet ports from running dry. All cells in flasks, plates, or microfluidic devices were stored in a humidified cell culture incubator at 37°C and 5% CO_2 atmosphere.

WGA Pulse-Chase Experiments. LUHMES cells were differentiated in microfluidic devices as usual and incubated with fluorescent α-syn seeds. After the particular cultivation time, cells were incubated with 5 µg/ml WGA-Alexa488 (Thermo Fisher Scientific) in differentiation media for 30 min, followed by 2 min washing with PBS+ and 4 h further cultivation in differentiation media. Cells were fixed and immunolabeled as described before.

Cell Culture for Single-Cell Lysis Experiments. For single-cell experiments, the standard cell culture procedures were performed, but cell suspension was seeded in miniaturized Petri dishes on ITO-coated glass slides (Diamond Coatings UK, 8-12 Ω /square). The miniaturized Petri dishes were made from PDMS (Dow Corning SYLGARD 184) rings and pressed onto the ITO surface to form sample wells. The PDMS rings were filled with 300 µl of the particular cell culture media with total 10^4 cells. The cell cultures were incubated as usual at 37°C and 5%CO_2 atmosphere. Prior single-cell lysis experiments, adherent cells were washed with HEPES, PBS or hypotonic PBS buffer, depending on lysis protocol.

PEG Surface Functionalization. Two different approaches were used to coat the PDMS surface with PEG. First, PLL-g-PEG with a PLL (20kDa) to PEG (2kDA) ratio (g) of 3 to 4 (SuSoS AG, Dübendorf, Switzerland) was dissolved at a concentration of 1mg/ml in 10mM HEPES buffer (pH 7.4). Solution was sterile filtered and aliquots were stored at 4°C. Thawed aliquots were diluted to 100 µg/ml with HEPES buffer before use. PDMS devices were plasma activated on the channel side, immersed in the PLL-PEG solution and incubated for 20 h in the range of 20 to 60°C. Devices were washed in nanopure water for 10 min, dried with N_2, and stored at RT till further use.

PEG-silane coating was performed according to previously published protocols [354]. 3-[Methoxy(polyethyleneoxy)propyl]trimethoxysilane, tech-90, 6-9 C_2H_4O units, was purchased from abcr GmbH (Karlsruhe, Germany). Extra dry acetone 99.99 (EMS, Hatfield, USA) was used to make a 50% (v/v) PEG-silane solution immediately prior use. The oxygen plasma activated PDMS device was immersed and allowed to react for 1h at RT. The devices were washed 2 x 10 min in MQ water and dried at RT till further use.

Single-Cell Lysis Procedures. LUHMES single-cell lysis experiments were performed according to our previously published protocols [334, 335]. In brief, cells on ITO wells were placed in the slide holder on the inverted microscope of the cell lysis setup and put to electrical ground. An individual cell was selected under the microscope, and the microcapillary tip was immersed into the buffer and placed 20 µm above it. Three to five short voltage pulses (250 µs at 16–20 V) were delivered via the microcapillary electrodes to the targeted cell. The cell lysed within milliseconds, and its content was directly aspirated into the microcapillary electrodes tip in 3 nl of liquid by the syringe pump. The

outer surface of the microcapillaries was with 2 nm of Ti/W and 200 nm of Pt by sputter deposition, and subsequently functionalized by immersion into a 1 M ethanolic solution of 1-dodecanethiol for 24 h to increase the hydrophobicity.

LUHMES Batch Lysate for MS and Sample Preparation. To prepare batch lysate, the cells cultivated in a T-25 flask were washed with PBS (Dulbecco's Phosphate Buffered Saline, Sigma Aldrich, Switzerland) and lysed with a solution of 8 M urea, 75 mM NaCl in 50 mM Tris buffer, pH 8.2, supplemented with protease inhibitor cocktail (complete mini, Roche, Switzerland), 1 mM β-glycerophosphate, 1 mM sodium orthovanadate, 10 mM sodium pyrophosphate, and 1 mM phenylmethylsulfonyl fluoride (PMSF), all from Sigma Aldrich, Switzerland. 50 µl aliquots of batch lysate at a concentration of ~5 mio cells/ml were stored at -20 °C. To print slides, an aliquot was diluted in 150 µl H_2O, yielding a concentration of ~1250 cells/µl.

Sample deposition was performed similar to RPPA experiments. As substrate, COC slides were used (ChipShop GmbH, Germany), dried after spotting and stored under argon gas till further use.

LUHMES Batch Lysate for Western Blot. LUHMES cells were prepared according to standard protocol. When cells reached the desired day of differentiation, the monolayer was washed twice with PBS- (Dulbecco's Phosphate Buffered Saline, without $MgCl_2$ and $CaCl_2$, Sigma Aldrich, USA) and the whole flask was shock frozen in LN_2 and stored at -20°C till further use. Cells were thawed on ice and incubated for 10 min with lysis buffer (MHB with 1x cOmplete™ protease inhibitor cocktail, 1mM PMSF, 1 mM Na_3VO_4, 0.25% sodium deoxycholate, 1% NP40) on ice. After removal of membranes and cell debris via centrifugation at 10000 rcf for 10min, protein concentration was determined using the BCA assay.

Western Blot. An equal of 35 µg protein from the cell lysate was prepared of each sample, mixed 1:5 with sample buffer, boiled for 5 min at 95°C, and separated by SDS-PAGE. Gels were transferred onto nitrocellulose membranes by semi-dry transfer (TE77XP, Hoefe). After blocking in 10 % BSA in TBS (0.05 M Tris and 0.15 M NaCl, pH 7.6), membranes were incubated with primary antibodies for 2 h in TBS with 0.1% Tween20 and 5% BSA. After 3 x 10 min washing in TBS, secondary antibodies were incubated in the same buffer (IR-antibodies, LI-COR,). Nitrocellulose membranes were scanned with an odyssey infrared imaging system (LI-COR, USA)

Dot Blot Analysis. Dot blot experiments were performed using a 96-well Bio-Dot® microfiltration apparatus (Bio-Rad Laboratories, USA). Assembly and cell lysate loading was done according to manufacturer's instructions. Immunoassay procedure followed the same instructions as for western blots, with minor differences. First blocking step, primary antibody incubation and washing steps were done in the wells of the apparatus.

Subsequently, the apparatus was dismantled and the nitrocellulose was passed into a dish for immunolabeling following the western blot protocol.

α-Syn Expression and Purification. Early experiments in this thesis were performed with lyophilized α-syn powder which was kindly provided by C. Eichmann and P. Kumari. Some purified α-syn in solution was provided by I. Mohammed. Further α-syn was produced according to their protocols using the same plasmids. BL21(DE3) Competent E. coli were transformed with plasmids and grown in lysogeny broth at 37°C and shaking at 120 rpm up to OD 0.8. After adding Isopropyl β-D-1-thiogalactopyranoside (Sigma-Aldrich) to a concentration of 1 mM, cells were grown for additional 4 h at the same conditions. Bacteria were collected by centrifugation and α-syn was extracted and purified according to ref [380].

α-Syn Fibril and Seed Formation. Standard seeds (Figure 19C), which were mainly used in this thesis, were produced in PBS+. Lyophilized α-syn monomers were dissolved at a concentration of 1-10 mg/ml and pH was adjusted to pH 7 using 1 M NaOH solution. When the solution was clear and the pH adjusted, aliquots were frozen in LN_2 and stored at -20°C. Proteins started to form oligomers and fibrils when stored at RT. To have consistent protocol from the same starting product, monomer solution was thawed and immediately ultra-centrifuged at 100,000 rcf for 30 minutes (TL-100, Beckman Coulter, USA). Only supernatant was collected, ensuring that no seed nuclei were present and fibrillization was initialized similarly throughout all experiments. Other types of fibrils were produced according to the standard fibril formation procedure but α-syn monomers were dissolved in different buffers. Ribbons were formed in tris buffer (50 mM Tris, 150 mM KCl, pH 7.5). The fibrils which can be seen in Figure 19C were produced in 20 mM sodium phosphate buffer with a 1M NaCl concentration (pH 7.4).

α-Syn oligomer (Figure 19B) formation procedure is similar to the fibril formation. A 12 mg/ml α-syn monomer solution was incubated at 37°C, but without agitation and seeds were already harvested after 24 h. Already formed fibrils were separated from oligomers by ultracentrifugation for 1 h at 247,000 x g ((TL-100, Beckman Coulter, USA). Monomers and small multimers were removed by repeated filtration using centrifugal filters with a 100 kDa cutoff (Amicon Ultra, MerckMillipore). Up-concentrated oligomers were frozen in LN_2 and stored at -20°C until further use.

To produce seeds of sheared α-syn fibrils, the fibril solution in 2 ml Eppendorf tube was sonicated for 1 h at 4°C in a UP200St VialTweeter block sonitrode (Hielscher, Germany) at full power and half second intervals just prior use.

Protein Labeling. Before seeds were formed, α-Syn fibrils were prepared at a concentration of 4 mg/ml in PBS+ and labeled via amine groups using N-hydroxy succinimidyl ester (NHS) conjugates. For fluorescent labeling, Alexa Fluor®546

(Invitrogen, USA), Oregon Green®488 carboxylic acid (Invitrogen, USA) and Sulfo-Cyanin 5 (Lumiprobe, USA) NHS-ester conjugates were used according to established protocols from the manufacturer. Alternatively, fibrils were biotinylated using photo-cleavable N-hydroxysuccinimidobiotin (PC-Biotin-NHS, AmberGen Inc., USA). A 5-fold excess of NHS-ester conjugates from a previously prepared and aliquoted stock solution was added the fibrils solution. After shaking for 2 h at RT, free conjugates were removed from labeled proteins on HiTrap desalting columns (Sephadex G25) using the corresponding running buffer. The labeled proteins were stored in aliquots at -20 °C. Alternatively, labeling solution was repeatedly sedimented at16,000 rcf in an Eppendorf centrifuge and the α-syn fibril pellet was washed four times in the corresponding buffer.

Protein Concentration Determination with Nanodrop. Protein concentrations were determined spectrophotometrically using a NanoDrop microvolume spectrophotometers (ThermoFisher Scientific, USA). For α-syn, an extinction coefficient of 5960 M^{-1} cm^{-1} at 280 nm was used [288].

Protein Concentration Measurement with Bicinchoninic Acid (BCA) Assay. Protein concentration was determined with a commercial available BCA kit (Pierce™ BCA Protein Assay Kit, ThermoFisher Scientific, USA) according to manufacturer's protocol. In brief, diluted BSA standards were prepared from a provided stock solution in a range of 25 µg/ml to 2000 µg/ml. Standards were aliquoted and kept a -20°C to speed up repeated measurement procedures. No difference was found between frozen aliquoted standards and freshly prepared standards. Proteins of interest were diluted to be in the range of the standards. Since measurements were performed on a NanoDrop microvolume spectrophotometers (ThermoFisher Scientific, USA) a sample to working reagent ratio of 1:10 was used. Samples were incubated for 30 min a 37°C. When cooled to RT, absorbance was measured at 562 nm. Measurements were performed using the NanoDrop BCA quantification module.

Microfluidics In-line Protein Extraction. Photo cleavable N-hydroxysuccinimidobiotin (PC-Biotin-NHS, AmberGen Inc., USA) was prepared in anhydrous DMF at a concentration of 50 mM and stored at -20°C. For biotinylation, 0.5 mg/ml α-syn fibrils were prepared in PBS and PC-Biotin-NHS stock was added to a concentration of 100 µM. After 1 hour incubation at RT in an Eppendorf shaker at 600rpm, fibrils were washed four times by centrifugation at 100000g for 30 minutes. Superparamagnetic streptavidin beads (Ocean NanoTech, USA) were mixed 1/100 with the fibril solution and incubated at RT. After 1 hour, 2.5 µl of the sample was aspirated in the capillary of 250 µm in diameter. By passing the magnets, the fibrils which interacted with magnetic beads were trapped. The trapped assemblies were washed with 4 µl of PBS which was aspirated in the setup before

the sample and this washing fraction was collected. To release the fibrils, either the magnet was switched off or the crosslinker was cleaved by UV light.

Buffers for Revers-Phase Protein Array. For PBS-T, PBS+ buffer (Dulbecco's Phosphate Buffered Saline, 2.7 mM KCl, 1.5 mM KH2PO4, 136.9 mM NaCl, 8.9 mM Na2HPO4•7H2O, pH 7.4, Sigma Aldrich, USA) was supplemented with 0.2% or 0.1% (v/v) Tween20 (Sigma Aldrich, Switzerland). TBS-T buffer (0.05 M Tris and 0.15 M NaCl, pH 7.6, 0.01% Tween20 (Sigma Aldrich, Switzerland)) was prepared in advance, sterile filtered and stored at RT. Blocking buffer consisted of a 1:1 mixture of LiCor ODYSSEY blocking buffer (LI-COR Biotechnology GmbH, Germany) and PBS-T 0.2%. A 1:10 dilution of blocking buffer in PBS-T 0.1% was used for washing. The final wash in a 50 ml Falcon tube was done in TBS-T 0.1%.

Revers-Phase Protein Array Principle and Analysis. The same instrument was used for RPPA slide preparation that was also used for single-cell preparation for EM [333]. Instead of performing single-cell lysis of LUHMES cells and writing the sample on EM grids, batch lysate was prepared and spotted on nitrocellulose coated glass slides (UniSart® 3D slide, Sartorius AG, Germany) or on hydrogel coated glass slides (NEXTERION® Slide H, SCHOTT Technical Glass Solutions GmbH, Germany). An openBEB macro script was prepared with defined flow rates, aspiration volumes, deposition volumes and spot positions. To wash the microcapillary between new samples, the tip of the microcapillary was inserted in a detergent solution (1% Alconox, Alconox Inc., USA) and flushed in and out with a high flow of detergent inside and around the tip of the microcapillary. The tip was then flushed with clean ddH2O.

After spotting, the nitrocellulose glass slides were blocked for 10 min at RT with blocking buffer in a 16-well incubation chamber (ProPlate 16 Well Slide Module 204862, Grace Bio-Labs, USA). Subsequently, each well was incubated with 100 µl of primary antibody solution for 18 h at RT. After washing with 200 µl washing buffer, secondary antibody solution was applied for 1 h at RT and again washed twice. Finally, slides were quickly immersed in TBS-T in a 50 ml Falcon tube, dried with nitrogen and kept at RT till used for microarray scanning.

For the analysis, two different scanners were used. Nitrocellulose coated slides were scanned with an odyssey infrared imaging system (LI-COR, USA). The hydrogel coated glass slides were scanned with an MS 200 Microarray Scanner (Roche NimbleGen, USA) with 10 µm/pixel at 532 nm and 635 nm. Images were processed with GenePix Pro 6.0 software (Molecular Devices, LLC, USA) and intensity data was exported and analyzed with TIBCO Spotfire software (TIBCO, USA).

TEM Negative Stain. Sample aliquots of 4 µl were adsorbed for 60 s on glow discharged carbon coated electron microscopy grids. Subsequently, grids were blotted, washed four

times on drops of deionized water and negatively stained by floating them twice for 10 seconds on 2% (w/v) uranyl acetate. The excess of liquid was blotted away between all washing and staining steps with Whatman® 1 filter paper. Grids were imaged with a T12 electron microscope (FEI) operating at 120 kV and equipped with a TVIPS F416 CMOS camera.

CLEM: Growing LUHMES Cells on EM Grids. LUHMES cell culturing and pre-differentiation was done according to a published protocol [301] and described above. Following types of gold EM grids were used: type NH2 200 mesh finder grids R 3.5/1, 200 mesh R3.5/1 and 400 mesh R2/2, all from Quantifoil® (Quantifoil Micro Tools GmbJ, Germany). All of them are suitable to perform CLEM. However, finder grids, in case the letters are not entirely covered, can assist with the orientation in both manual and software assisted correlation. Grids were sterilized in pure EtOH, glow-discharged for 20 s in air plasma and placed in PDMS rings (ID of 1 cm) on microscopy slides and again washed with EtOH. Prior adding Geltrex® solution, dishes were emptied and rinsed with PBS. Grids must never run dry, otherwise the carbon layer sticks to the glass surface. For the Geltrex® to cure, dishes were placed in rectangular culture dishes and incubated for 1h at 37°C.

Pre-differentiated LUHMES cells (after 24 hours of differentiation) were counted with a hemocytometer counting-chamber and 6 x 10^5 cells in 300 µl differentiation media were loaded in each dish. Cells were incubated at 37°C, 5% CO_2 and cell media was changed every second day.

CLEM: Vitrifying LUHMES Cells on EM Grids. Cryo-EM grids for CLEM were prepared using Vitrobot Mark IV (ThermoFisher Scientific, USA) with manual blotting or a Leica EM GP (Leica Microsystems GmbH, Germany). For manual blotting, vitrobot humitdity chamber was set to 100% humidity at 32°C and blot time was set to zero seconds. Filter paper was cut into small pieces and bent to 90°C, to be a able to hold one end with a tweezer and blot with the other perpendicular to this direction. Liquid ethane was prepared. Grids with LUHMES cells were taken from the cell culture incubator and washed once with PBS. Grids were grabbed by the special vitrobot tweezer and mounted to the vitrobot. 5 µl of 1/10 in PBS diluted ProteinA gold 10 nm was applied on the grid the grid was retracted to the humidity chamber. From the side window, grids were blotted for 10 seconds with the prepared “L” shaped filters and plunge frozen.

CLEM: Imaging Vitrified Grids with Light Microscopy. We used an upright microscopy (Axio Imager M2, Carl Zeiss AG, Jena, Germany) with an AxioCam Mrm camera (Carl Zeiss AG, Germany). Digital acquisition and image analysis was done with AxioVision software (Carl Zeiss AG, Germany). The long working distances of the objectives allowed the application of a CLM77K cryostage (Instec, Inc., USA). A

thermocouple on the grid holder tongue and the cryostage allowed for monitoring the temperature at all times. The temperature of the stage was controlled by the Instec mk1000 temperature controller (Instec, Inc., USA) linked to a liquid nitrogen pump with reservoir. A stream of nitrogen was directed to the top and bottom window of the cryostage to prevent ice formation.

CLEM: Mapping Live Cells on EM grids.

To record a map at RT, a similar procedure was follow as when using vitrified grids. The advantage was to see the state of the cell before vitrification. Additionally, grids get lost or were destroyed easily while using the light microscopy cryostage. Since we used an upright microscopy the glass slides with the grids needed to be imaged upside-down. Spacers made from PDMS were placed on both sides of a second glass slide on which the sample grids were placed. Forming a 'sandwich' like that, the miniaturized PDMS Petridish was not in contact with the second slide and cell media was retained in the dish by surface tension. Image were recorded using a Zeiss Axiophot microscope. 4 x 4 images were recorded per grid and stitched together with the grid/collection stitching plugin in Fiji software. Mounting and recording was done within 5 min, as samples were at RT. Subsequently, suitable grids were plunge frozen immediately.

CLEM: Cryo Electron Microscopy. Vitrified LUHMES cells were imaged on two different EM. First, a Philips CM200 equipped with a field emission gun was used. The microscope operated at an acceleration voltage of 200kV and images were acquired on an UltrascanTM1000 CCD camera.

Other samples were recorded on a Titan Krios (ThermoFisher Scientific, USA) which operated at 300kV, and equipped with an Gatan Quantum-LS Energy Filter (GIF, 20eV energy loss window; Gatan Inc.). Images were recorded with a K2 Summit direct electron detector (Gatan Inc.,) in dose fractionation mode (50 frames) using Serial EM software [372] at a magnification of 33,000 x. Micrographs were drift-corrected and dose-weighted through the Focus interface [381].

Resazurin Assay. LUHMES cells were cultivated in 96-well plates according to standard protocol. Specifically for this assay, 40'000 predifferentiated cells in 100 µl differentiation media were loaded in each well. To test the effect of α-syn fibrils on cell viability, differentiation media with different concentrations of fibrils were prepared and 100 µl of the particular solution was added per well on day 4 of differentiation. Resazurin assay was performed on day 12 of differentiation. Till then, 100 µl of differentiation media was exchanged in each well every second day.

Resazurin sodium salt powder (Sigma-Aldrich, USA) was dissolved in PBS (Dulbecco's, Sigma-Aldrich, USA) to a final concentration of 1 mg/ml. The resazurin solution was

diluted in differentiation media to a final concentration of 5 µg/ml. Media from wells was replaced with staining solution and cells were incubated at 37°C, 5% CO_2 2 hours. Then, 50 µl supernatant of the reduced solution was replated to a second well plate and fluorescent intensity was measured at 530 nm_{ex} and 570 nm_{em} / 600 nm_{em} using the fluorescent intensity scanning mode on a Tecan Infinite M1000® microplate reader (Tecan, Switzerland).

Mitochondria Labeling with MitoTracker. Labeling with MitoTracker™ was done according to manufacturer's protocol with minor changes. In brief, 1 mg/ml stock solution was prepared from lyophilized MitoTracker™ Green FM (ThermoFisher Scientific, USA) at RT in anhydrous DMSO. Aliquots of 10 µl were stored at -20°C. For staining, stock aliquots were thawed and diluted in LUHMES differentiation media to either 40 nM for live cell imaging or 200 nM when cells were fixed. After incubation for 15 min at 37°C, 5% CO_2, staining media was replaced with normal differentiation media and cells were immediately observed on a fluorescent microscope. For fixed samples, normal fixation procedure was followed immediately after incubation.

Computational Fluid Dynamics Simulation. The computational fluid dynamics (CFD) module of the software COMSOL Multiphysics 5.2 (COMSOL Inc, Burlington, USA) was used to evaluate the fluidic isolation between the two cell compartments of the microfluidic co-culturing device. The static laminar state right after applying media to the inlet ports was described by solving the incompressible Navier-Stokes-equation. We assumed a Newtonian fluid with properties of water at RT. PDMS was chosen as boundary material from COMSOL's material library. To simulate the hydrostatic pressure driven flow, an atmospheric pressure of 101325 Pa was assigned to the outlet ports and a pressure of 101364.24 Pa to the inlet ports, which corresponds to a 4 mm column of water.

APPENDIX A

Supporting Information: Chapter 2

A.1 Computational Fluid Dynamics Simulation

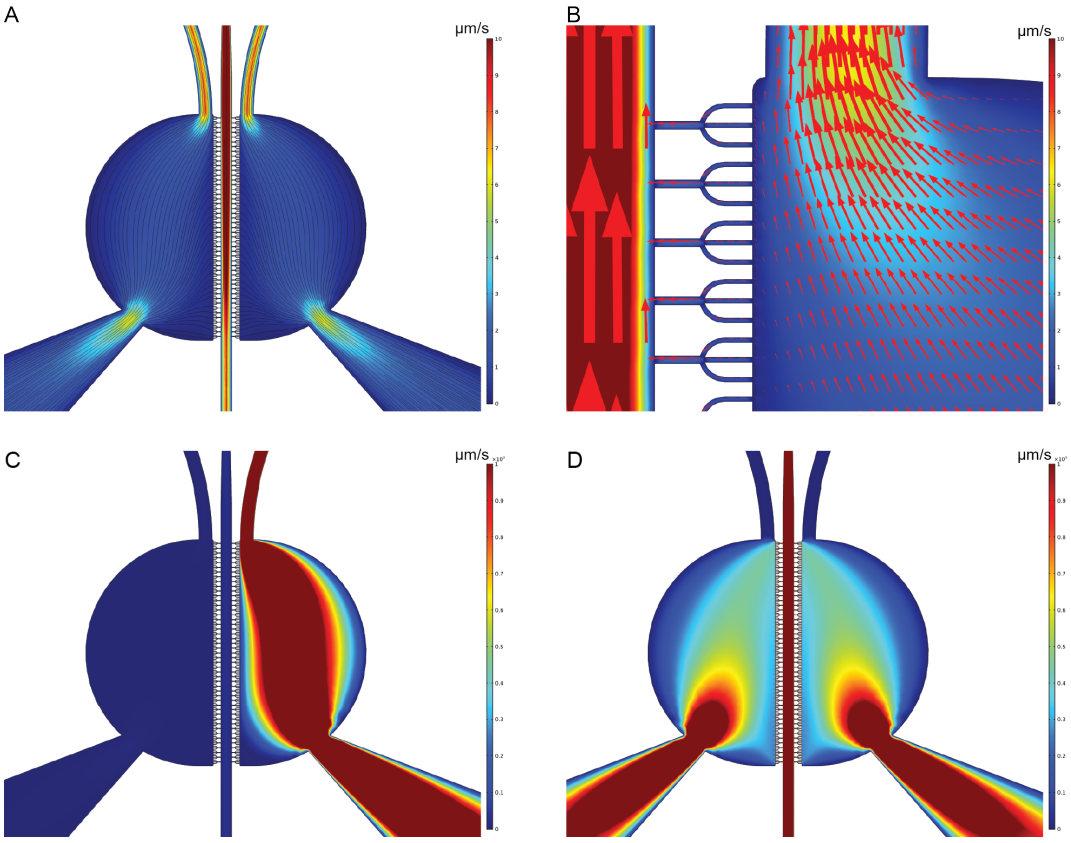

Figure A.1. CFD analysis of fluid flow through the microfluidic co-culturing device with different pressures applied. Flow rates are pictured in colored spectra. (A) Black lines represent stream lines. A pressure difference corresponding to a 4 mm water column in all three inlet ports was applied. (B) Same conditions as in A. Size of the arrows is proportional to the flow velocity and their direction is aligned to the stream. (C) An underpressure of -400 mbar was applied to the outlet port of the right channel. (D) An under-pressure of -400 mbar was applied to the outlet port of the central channel.

Flow velocities in microfluidic co-culturing devices were simulated by the CFD module in COMSOL Multiphysics 5.2. A pressure difference of about 40 Pa between the inlet and outlet ports resulted in a velocity of under 3 µm/s in the center of the cell growth compartments (Figure A.1A). This maintains a constant media change without disturbing cell growth. Still, neurite alignment was observed at this low velocity (Figure 12). Using the same parameters, a slight inflow from the cell compartments through the central channels was simulated (Figure A.1B). This does not influence the fluidic separation towards the second growth chamber, as the same inflow occurs and the central channels high flow rate acts as a fluidic barrier. During cell loading a vacuum is applied to the outlet ports of the growth chambers. Comparing Figure A.1C and D, it becomes clear why no vacuum should be applied to the central channel, as high velocities press the cells to the microchannels, resulting in shear stress and cell damage.

A.2 Geltrex® Coating vs. Fibronectin / PLO Coating

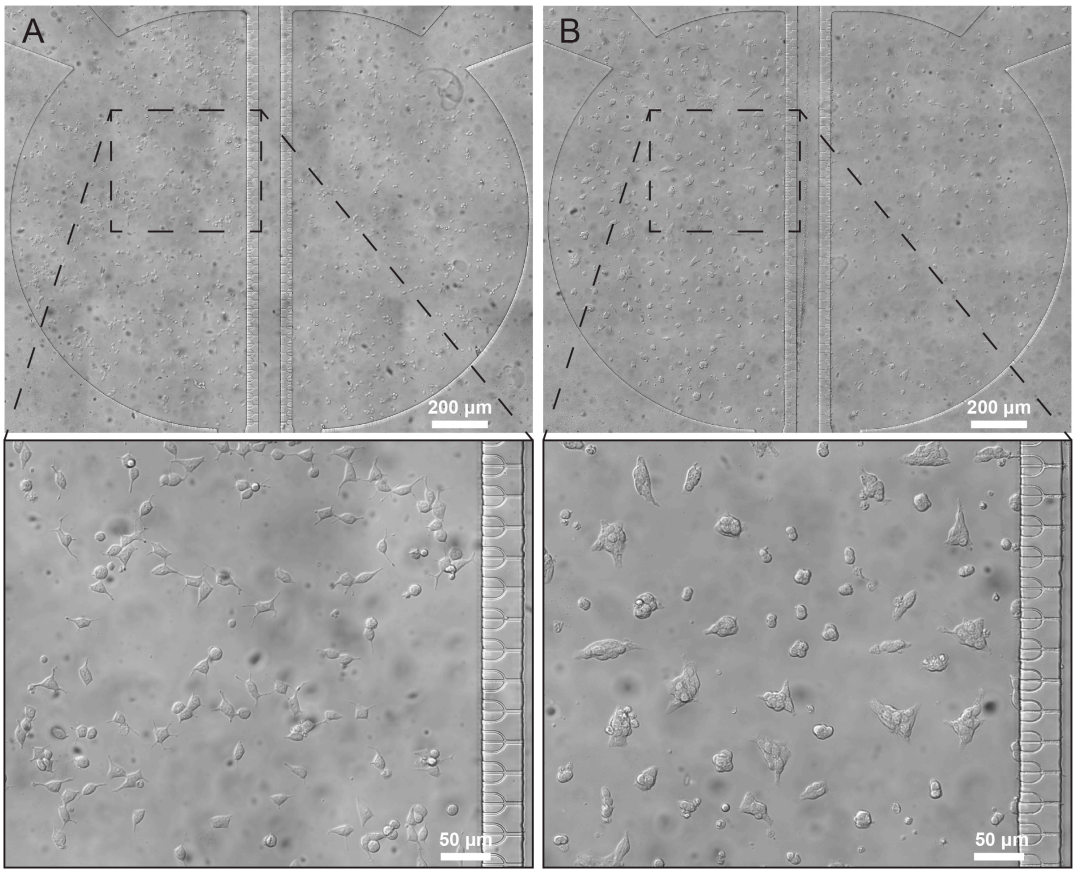

Figure A.2. Comparison of LUHMES cells growing on Geltrex® (A) or fibronectin/PLO (B) coating in microfluidic devices. Cells were taken directly from proliferating stated and resuspended in differentiation media. Images were taken 1 h after cells were loaded.

A.3 Evaluation of Optimal Seed Concentration

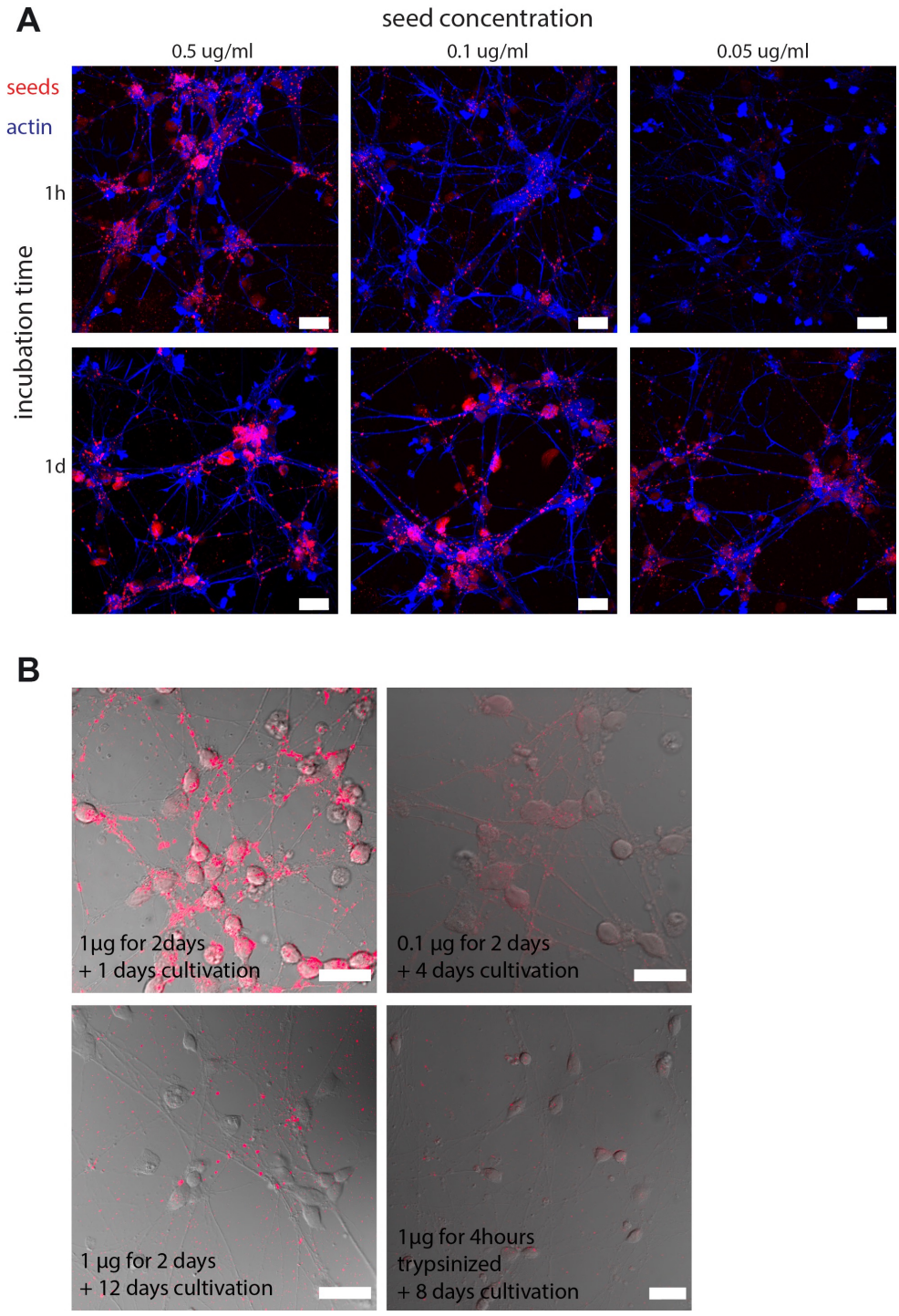

Figure A.3. (A) Seeds were added to LUHMES cells at different concentrations and media solution was replaced after 1 h or 1 day. After seeding, cells were cultivated for an additional 3 days. (B) Seeding experiments with different concentrations, incubations times, and cultivation times. Scale bars 20 µm.

Seed dilution and incubation time series were made to assess seeding conditions using LUHMES cells. It appears that seeds attach to cell membranes within 1 hour (Figure A.3.A, top panel) and seed concentration increases with longer incubation time, as α-syn fibrils have more time to settle (Figure A.3.A, bottom panel).

When cells grow for longer periods after depletion of α-syn fibrils in the culturing media, it appears that the amount of fluorescent signal decreases (Figure A.3B). This may be due to internalization and seed degradation, or seeds detaching from the membranes and being removed during media change. However, most of the α-syn fibrils seeds stick to the membrane, as they can be easily removed by washing the cells with trypsine (Figure A.3B, bottom right). Additionally, labeled fibrils can be found on the background, not covering any obvious cell body or neurite. This can also be observed after trypsinizing and washing the cells, indicating that some α-syn fibrils are secreted or released from apoptotic cells.

A.4 Seed Uptake and Aggregate formation

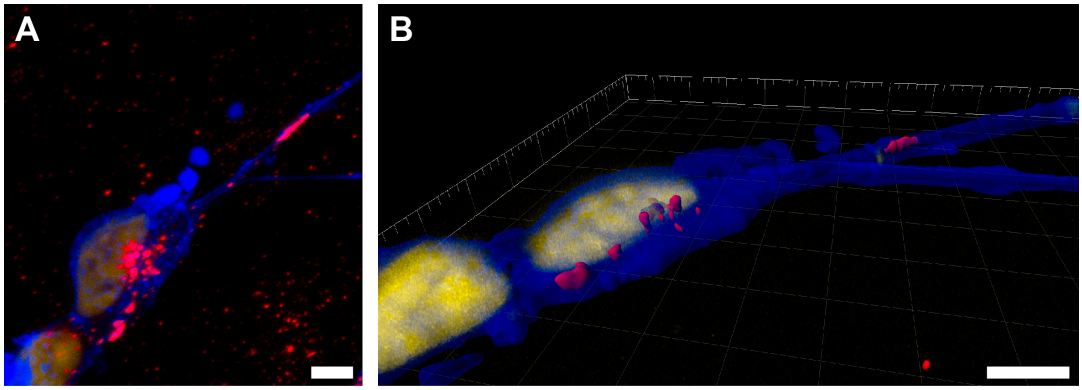

Figure A.4. (A) Confocal images of LUHMES cells incubated with fluorescent seeds. (B) Same cells as in A but intensity isosurface rendered in Imaris 9. Scale bars 5 µm.

Aggregate formation of extracellularly added seeds can be observed inside cell soma and neurites, and extracellularly on the cell membrane. This is usually only the case after incubation times of more than one day and at high seed concentrations (Figure A.3B). Whether the extracellular aggregates are formed in solution, on the cell membrane, or intracellularly followed by release remains to be determined. However, intracellular aggregates can be observed at seed concentrations of 0.1 µg/ml after 4 days of cultivation (Figure A.4). The aggregates appear much brighter in confocal microscopy than the average of small puncta in the background (Figure A.4A). Aggregates can also be found in neurites, where they adapt an elongated shape.

A.5 Anterograde Transport of α-Syn Fibrils

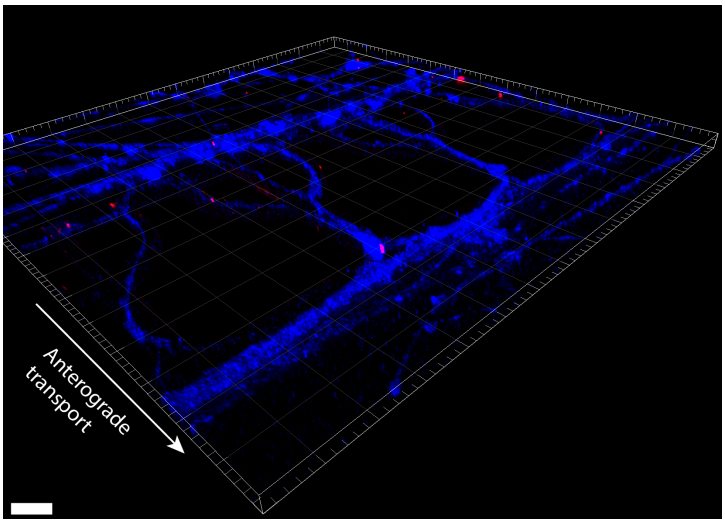

Figure A.5. 3D Volume of LUHMES cell neurites growing through microchannels. A 0.5 µg/ml seed solution was applied to the inlet of one growth chamber on day 2 of differentiation. Cells were fixed after 8 days of cultivation. Scale bar 20 µm.

APPENDIX B

Supporting Information: Chapter 3

B.1 Strains of α-Syn Assemblies

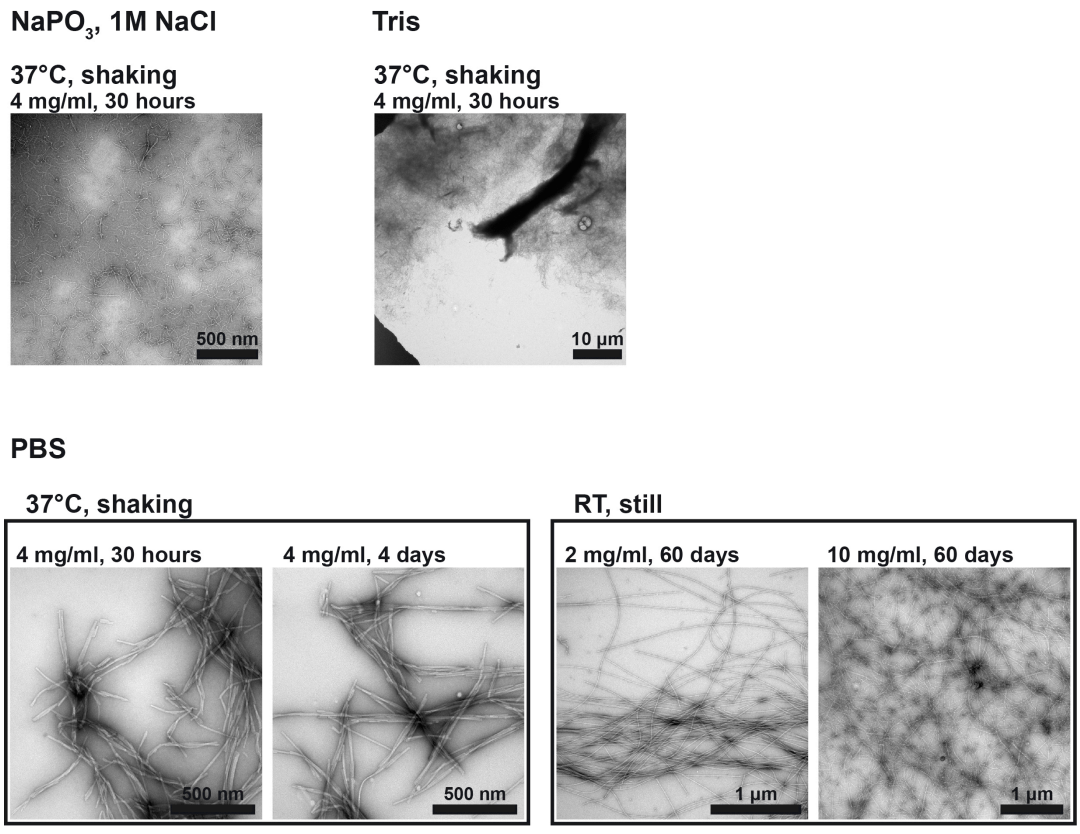

Figure B.1. Additional selection of negatively stained α-syn fibrils. Crucial protocol steps are linked to the figures.

B.2 Immunolabeling of Endogenous α-Syn

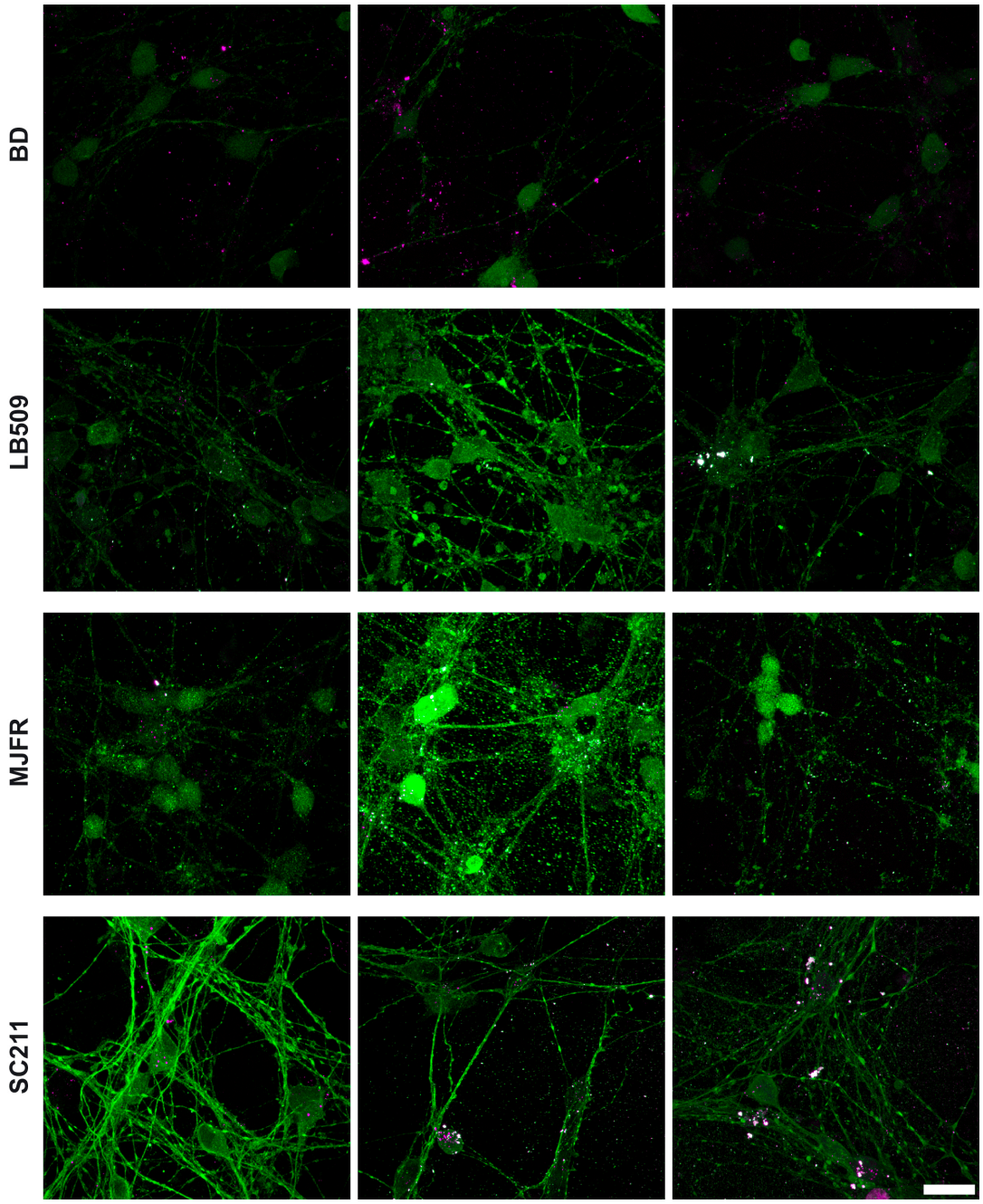

Figure B.2. Confocal images of LUHMES cells with immunolabeling against α-syn. Four different antibodies were tested. Antibody labeled α-syn can be seen in green and fluorescent seeds are in magenta. When antibodies co-localize with seeds, it appears in white color. Scale bar 20 µm.

APPENDIX C

Supporting Information: Chapter 4

C.1 Simple Microfluidic Co-Culturing Devices

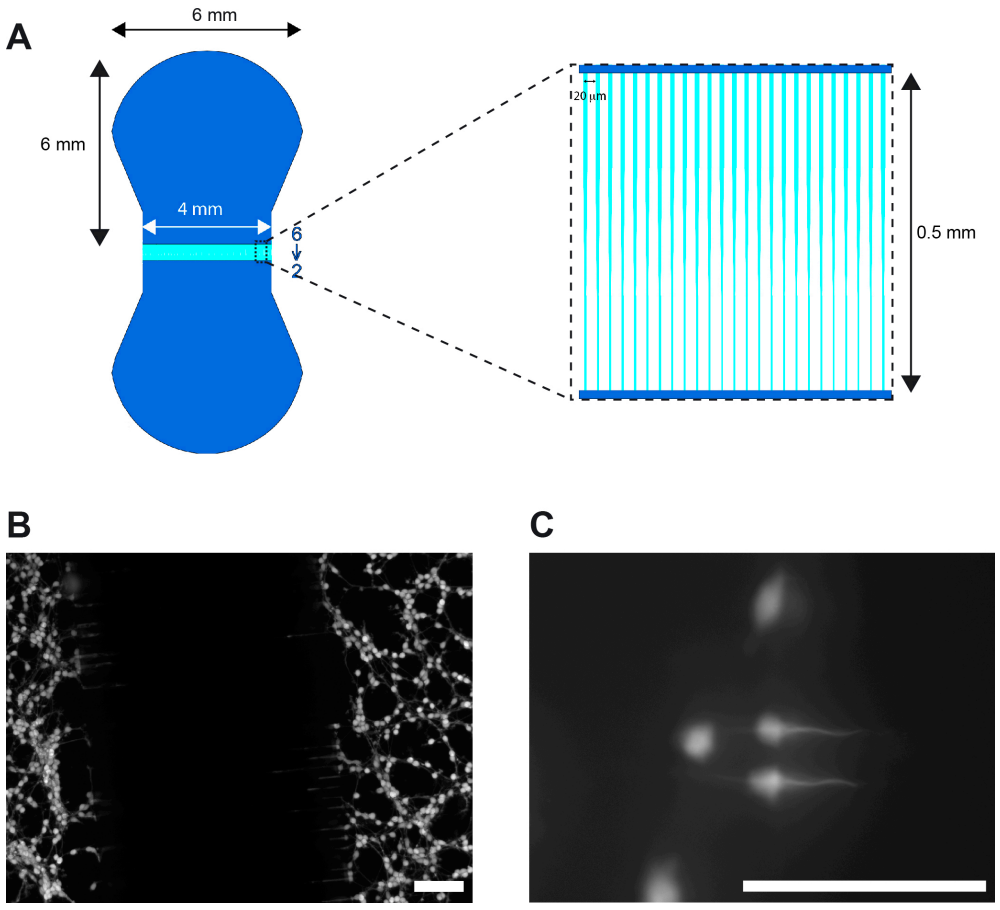

Figure C.1. (A) Scheme of a basic microfluidic co-culturing device designed by M.K. Lewandowska. (B) LUHMES cells labeled with calcein-AM. (C) Neurites of LUHMES cells never grew completely through the connecting microchannels in this microfluidic device. Scale bars 100 µm.

C.2 LUHMES Cell Growth on ITO Glass

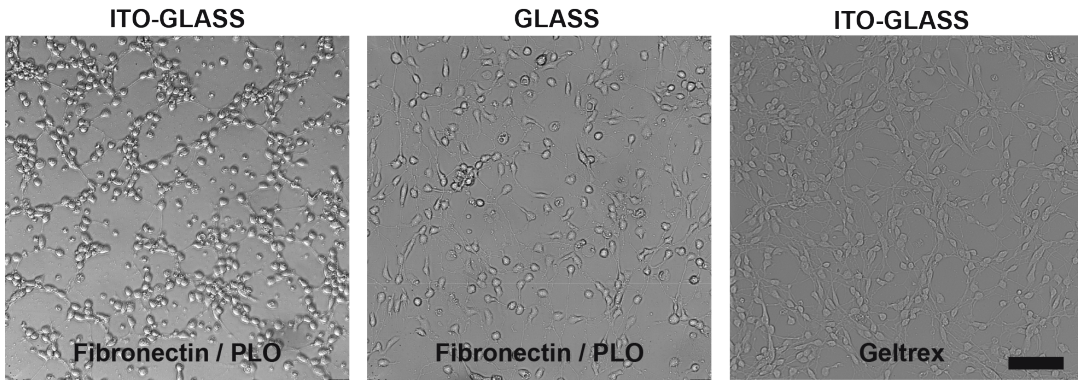

Figure C.2. Comparison of LUHMES cells differentiating on ITO-coated glass and non-coated glass. When the surface is coated with Geltrex®, cells differentiated also on ITO-coated glass slides. Scale bar 40 µm.

APPENDIX D

Supporting Information: Chapter 5

D.1 CLEM: Cryo-TEM Images of Neurites

When LUHMES cells are cultivated on EM grids, almost the whole grid is covered with neurites, cell bodies, and cellular material. In cryo-TEM, cell bodies are visible as black areas, since they are too thick for the electrons to pass. Between cell bodies of differentiating cells, an extensive neurite network is built (Figure D.1A). At low magnification, this network looks disordered and neurites cross each other from all directions. At higher magnification, it is revealed that several thinner neurites grow in parallel (Figure D.1B). The fine structures in the neurites can clearly be discerned (Figure D.1D), allowing the study of microtubule and luminal particles [362].

In Figure D.1C, an expanded end of a neurite can be seen, which is filled with vesicles in the range of 40-60 nm. Their size match the reported dimensions of synaptic vesicles [382]. Indeed, this neurite resembles the synaptic compartments which were recently imaged by a similar CLEM technique as it was used in this thesis [366]. However, LUHMES cells were reported to be an incompletely differentiated cell line [301]. Although MESC2.10 cells, the precursor of LUHMES cells, display excitatory and inhibitory postsynaptic potentials, indicating functional synapsis [297], no functional synapses were assumed in the LUHMES cell line using the standard differentiation protocol [301]. However, so far no cryo-EM studies were conducted using LUHMES cells. To make LUHMES cells accessible for CLEM, Geltrex®-coated EM-grids were used. As mentioned before, LUHMES cells acquire neuronal morphology much faster on Geltrex® compared to PLO/fibronectin coating. Thus, the synaptic maturity of LUHMES cells cannot be excluded and requires further investigation.

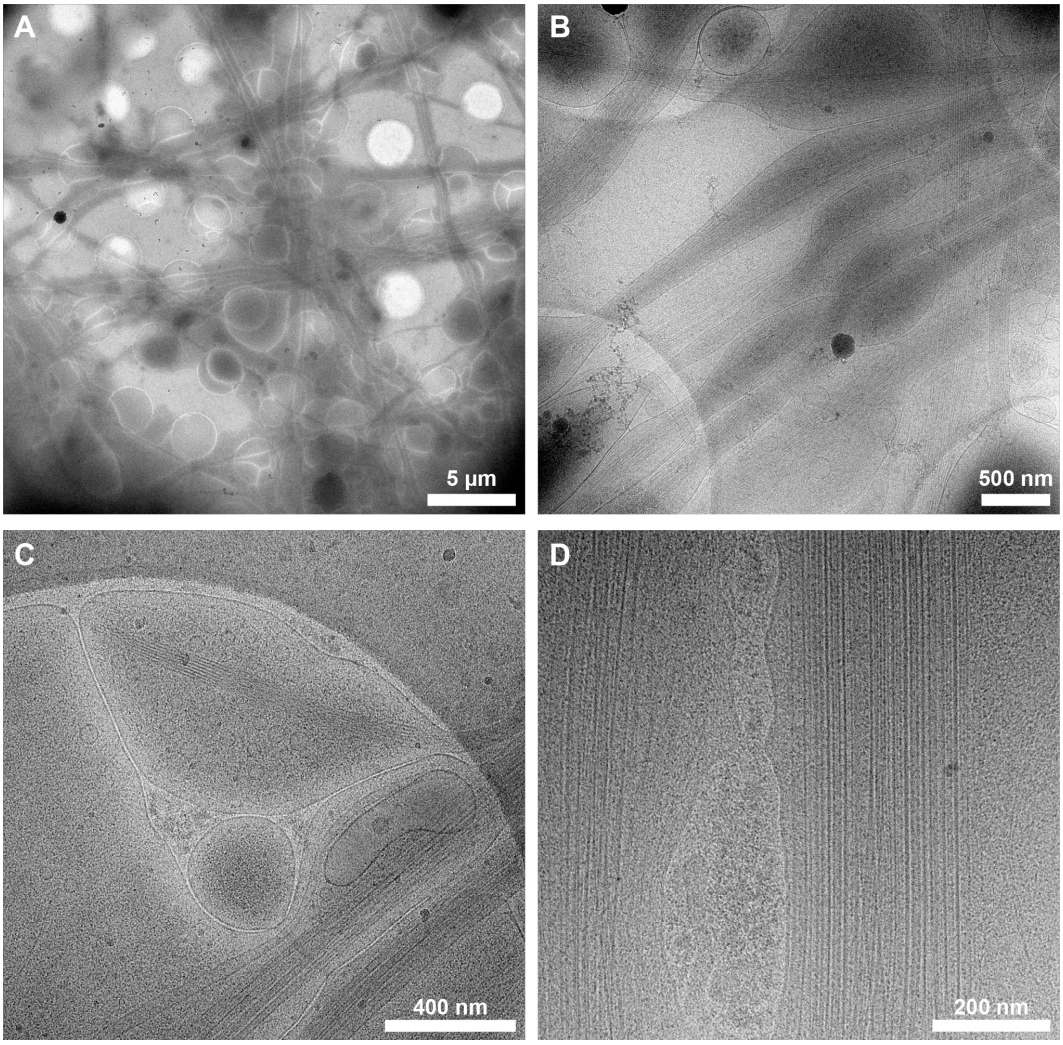

Figure D.1. Selection of cryo-TEM micrographs of LUHMES cell neurites. (A) Low magnification image of crossing neurites. (B) Neurites of grow parallel to each other. (C) Vesicle size at the end of a neurite is between 40 and 60 nm, which correspond to the size of synaptic vesicles. (D) Microtubules in neurites.

D.2 CLEM: Extended Blotting

Blotting times appear to be less crucial for vitrified sample preparation of on-grid cultivated cells as compared to protein solutions, for example. Cell bodies and the extended neurite network seem to retain liquid on the grid, even at long blotting times of 17 s (Figure D.2.C). Although large parts of the grids are dry, larger neurite bundles are nicely frozen for cryo-EM. However, whether or not long blotting times affect the neurite integrity remains to be tested.

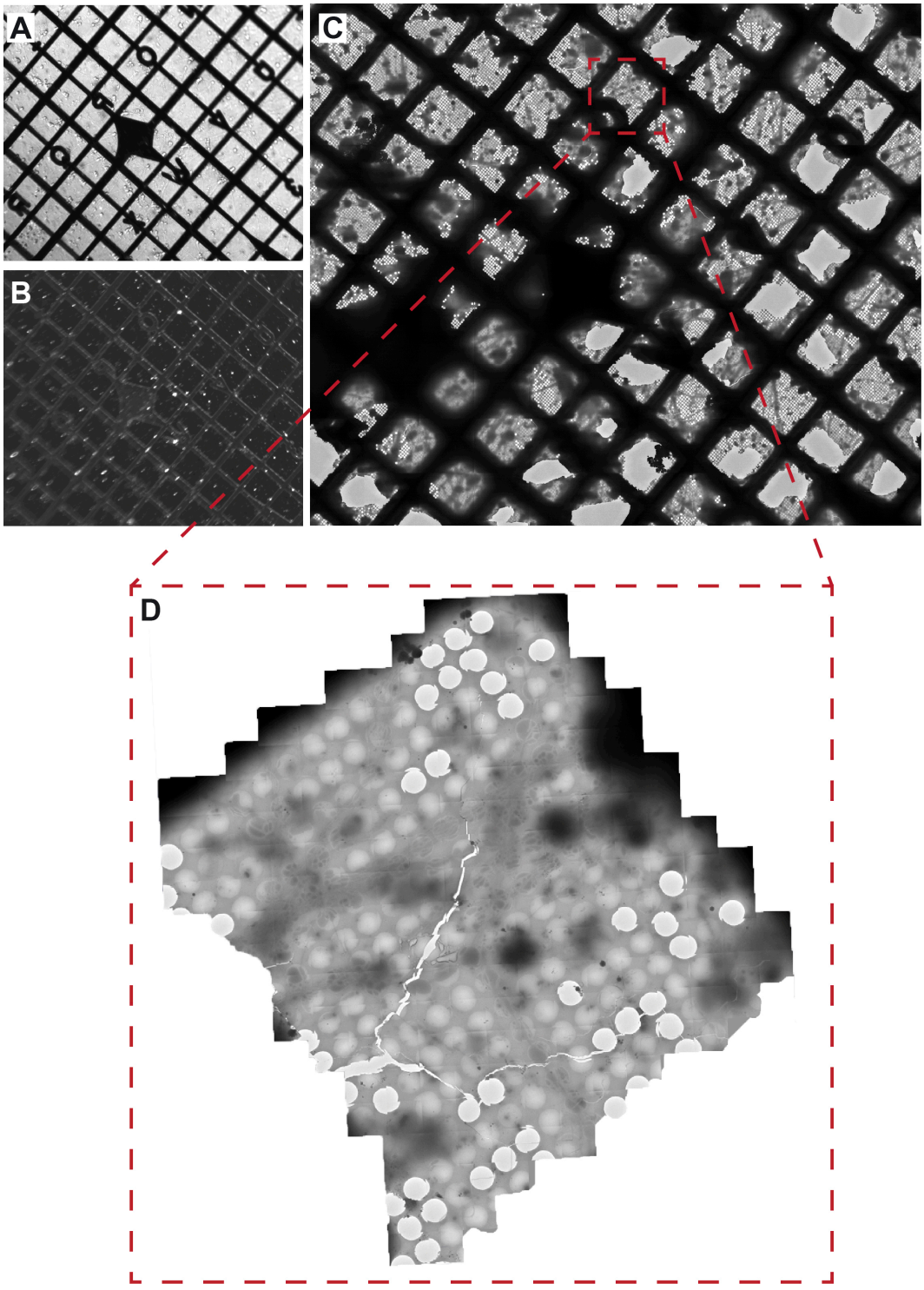

Figure D.2. (A) Bright field and (B) fluorescence microscopy of LUHMES cells growing on an EM finder grid. The grid was vitrified after light microscopy imaging. Blotting time before vitrification was extended to 17 seconds. (C) Cryo-TEM image of the same grid at low resolution. (D) Inset image recorded at higher resolution.

BIBLIOGRAPHY

1. Gammon, K., Neurodegenerative disease: brain windfall. *Nature*, **2014**. 515(7526): p. 299-300.
2. World Health Organization, Neurological Disorder: Public Health Challenges. *World Health Organization, Geneva*, **2006**.
3. Parkinson, J., An essay on the shaking palsy. 1817. *J Neuropsychiatry Clin Neurosci*, **2002**. 14(2): p. 223-36.
4. Tysnes, O.B. and Storstein, A., Epidemiology of Parkinson's disease. *J Neural Transm (Vienna)*, **2017**. 124(8): p. 901-905.
5. Hirsch, L., et al., The Incidence of Parkinson's Disease: A Systematic Review and Meta-Analysis. *Neuroepidemiology*, **2016**. 46(4): p. 292-300.
6. Reeve, A., Simcox, E., and Turnbull, D., Ageing and Parkinson's disease: why is advancing age the biggest risk factor? *Ageing Res Rev*, **2014**. 14: p. 19-30.
7. Alcalay, R.N., et al., Frequency of known mutations in early-onset Parkinson disease: implication for genetic counseling: the consortium on risk for early onset Parkinson disease study. *Arch Neurol*, **2010**. 67(9): p. 1116-22.
8. Marder, K.S., et al., Predictors of parkin mutations in early-onset Parkinson disease: the consortium on risk for early-onset Parkinson disease study. *Arch Neurol*, **2010**. 67(6): p. 731-8.
9. Poewe, W., et al., Parkinson disease. *Nat Rev Dis Primers*, **2017**. 3: p. 17013.
10. Van Den Eeden, S.K., et al., Incidence of Parkinson's disease: variation by age, gender, and race/ethnicity. *Am J Epidemiol*, **2003**. 157(11): p. 1015-22.
11. Baldereschi, M., et al., Parkinson's disease and parkinsonism in a longitudinal study: two-fold higher incidence in men. ILSA Working Group. Italian Longitudinal Study on Aging. *Neurology*, **2000**. 55(9): p. 1358-63.
12. Pringsheim, T., et al., The prevalence of Parkinson's disease: a systematic review and meta-analysis. *Mov Disord*, **2014**. 29(13): p. 1583-90.
13. Postuma, R.B., et al., MDS clinical diagnostic criteria for Parkinson's disease. *Mov Disord*, **2015**. 30(12): p. 1591-601.
14. Gelb, D.J., Oliver, E., and Gilman, S., Diagnostic criteria for Parkinson disease. *Arch Neurol*, **1999**. 56(1): p. 33-9.
15. Postuma, R.B. and Berg, D., The New Diagnostic Criteria for Parkinson's Disease. *Int Rev Neurobiol*, **2017**. 132: p. 55-78.
16. Hughes, A.J., Daniel, S.E., and Lees, A.J., Improved accuracy of clinical diagnosis of Lewy body Parkinson's disease. *Neurology*, **2001**. 57(8): p. 1497-9.
17. Rizzo, G., et al., Accuracy of clinical diagnosis of Parkinson disease: A systematic review and meta-analysis. *Neurology*, **2016**. 86(6): p. 566-76.
18. Buchman, A.S., et al., Nigral pathology and parkinsonian signs in elders without Parkinson disease. *Ann Neurol*, **2012**. 71(2): p. 258-66.
19. Garnett, E.S., Firnau, G., and Nahmias, C., Dopamine visualized in the basal ganglia of living man. *Nature*, **1983**. 305(5930): p. 137-8.

20. Seifert, K.D. and Wiener, J.I., The impact of DaTscan on the diagnosis and management of movement disorders: A retrospective study. *Am J Neurodegener Dis*, **2013**. 2(1): p. 29-34.

21. Pyatigorskaya, N., et al., A review of the use of magnetic resonance imaging in Parkinson's disease. *Ther Adv Neurol Disord*, **2014**. 7(4): p. 206-20.

22. Klein, C. and Westenberger, A., Genetics of Parkinson's disease. *Cold Spring Harb Perspect Med*, **2012**. 2(1): p. a008888.

23. Lill, C.M., Genetics of Parkinson's disease. *Mol Cell Probes*, **2016**. 30(6): p. 386-396.

24. Chen-Plotkin, A.S., Unbiased approaches to biomarker discovery in neurodegenerative diseases. *Neuron*, **2014**. 84(3): p. 594-607.

25. Førland., M.G., et al., Evolution of cerebrospinal fluid total α-synuclein in Parkinson's disease. *Parkinsonism & Related Disorders*, **2018**. 49: p. 4-8.

26. Caslake, R., et al., Changes in diagnosis with follow-up in an incident cohort of patients with parkinsonism. *J Neurol Neurosurg Psychiatry*, **2008**. 79(11): p. 1202-7.

27. Dickson, D.W., et al., Neuropathological assessment of Parkinson's disease: refining the diagnostic criteria. *Lancet Neurol*, **2009**. 8(12): p. 1150-7.

28. Damier, P., et al., The substantia nigra of the human brain. II. Patterns of loss of dopamine-containing neurons in Parkinson's disease. *Brain*, **1999**. 122 (Pt 8): p. 1437-48.

29. Iacono, D., et al., Parkinson disease and incidental Lewy body disease: Just a question of time? *Neurology*, **2015**. 85(19): p. 1670-9.

30. Bernheimer, H., et al., Brain dopamine and the syndromes of Parkinson and Huntington. Clinical, morphological and neurochemical correlations. *J Neurol Sci*, **1973**. 20(4): p. 415-55.

31. Hornykiewicz, O., Basic research on dopamine in Parkinson's disease and the discovery of the nigrostriatal dopamine pathway: the view of an eyewitness. *Neurodegener Dis*, **2008**. 5(3-4): p. 114-7.

32. Roy, S. and Wolman, L., Ultrastructural Observations in Parkinsonism. *Journal of Pathology*, **1969**. 99(1): p. 39-44.

33. Spillantini, M.G., et al., α-Synuclein in Lewy bodies. *Nature*, **1997**. 388(6645): p. 839-40.

34. Baba, M., et al., Aggregation of alpha-synuclein in Lewy bodies of sporadic Parkinson's disease and dementia with Lewy bodies. *Am J Pathol*, **1998**. 152(4): p. 879-84.

35. Duffy, P.E. and Tennyson, V.M., Phase and Electron Microscopic Observations of Lewy Bodies and Melanin Granules in Substantia Nigra and Locus Caeruleus in Parkinsons Disease. *Journal of Neuropathology and Experimental Neurology*, **1965**. 24(3): p. 398-414.

36. Ishizawa, T., et al., Colocalization of tau and alpha-synuclein epitopes in Lewy bodies. *Journal of Neuropathology and Experimental Neurology*, **2003**. 62(4): p. 389-397.

37. Olanow, C.W., et al., Lewy-body formation is an aggresome-related process: a hypothesis. *Lancet Neurology*, **2004**. 3(8): p. 496-503.

38. Wakabayashi, K., et al., The Lewy body in Parkinson's disease and related neurodegenerative disorders. *Mol Neurobiol*, **2013**. 47(2): p. 495-508.

39. Forno, L.S., Neuropathology of Parkinson's disease. *J Neuropathol Exp Neurol*, **1996**. 55(3): p. 259-72.

40. Mackenzie, I.R.A., The pathology of Parkinson's disease. *BCMJ*, **2001**. 43(3): p. 142-147.

41. Halliday, G., Lees, A., and Stern, M., Milestones in Parkinson's disease--clinical and pathologic features. *Mov Disord*, **2011**. 26(6): p. 1015-21.

42. Parkkinen, L., et al., Disentangling the relationship between lewy bodies and nigral neuronal loss in Parkinson's disease. *J Parkinsons Dis*, **2011**. 1(3): p. 277-86.

43. Schulz-Schaeffer, W.J., The synaptic pathology of alpha-synuclein aggregation in dementia with Lewy bodies, Parkinson's disease and Parkinson's disease dementia. *Acta Neuropathol*, **2010**. 120(2): p. 131-43.

44. Jellinger, K.A., Lewy body-related alpha-synucleinopathy in the aged human brain. *J Neural Transm (Vienna)*, **2004**. 111(10-11): p. 1219-35.

45. Terry, R.D., Do neuronal inclusions kill the cell? *J Neural Transm Suppl*, **2000**. 59: p. 91-3.

46. Gaig, C., et al., G2019S LRRK2 mutation causing Parkinson's disease without Lewy bodies. *J Neurol Neurosurg Psychiatry*, **2007**. 78(6): p. 626-8.

47. Braak, H., et al., Staging of brain pathology related to sporadic Parkinson's disease. *Neurobiol Aging*, **2003**. 24(2): p. 197-211.

48. Del Tredici, K., et al., Where does parkinson disease pathology begin in the brain? *J Neuropathol Exp Neurol*, **2002**. 61(5): p. 413-26.

49. Braak, H., et al., Stanley Fahn Lecture 2005: The staging procedure for the inclusion body pathology associated with sporadic Parkinson's disease reconsidered. *Mov Disord*, **2006**. 21(12): p. 2042-51.

50. Jellinger, K.A., A critical reappraisal of current staging of Lewy-related pathology in human brain. *Acta Neuropathol*, **2008**. 116(1): p. 1-16.

51. Burke, R.E., Dauer, W.T., and Vonsattel, J.P., A critical evaluation of the Braak staging scheme for Parkinson's disease. *Ann Neurol*, **2008**. 64(5): p. 485-91.

52. Beach, T.G., et al., Unified staging system for Lewy body disorders: correlation with nigrostriatal degeneration, cognitive impairment and motor dysfunction. *Acta Neuropathol*, **2009**. 117(6): p. 613-34.

53. Jellinger, K.A., Formation and development of Lewy pathology: a critical update. *J Neurol*, **2009**. 256: p. 270-9.

54. Attems, J. and Jellinger, K.A., The dorsal motor nucleus of the vagus is not an obligatory trigger site of Parkinson's disease. *Neuropathol Appl Neurobiol*, **2008**. 34(4): p. 466-7.

55. Walsh, D.M. and Selkoe, D.J., A critical appraisal of the pathogenic protein spread hypothesis of neurodegeneration. *Nat Rev Neurosci*, **2016**. 17(4): p. 251-60.

56. Piccini, P. and Brooks, D.J., New developments of brain imaging for Parkinson's disease and related disorders. *Mov Disord*, **2006**. 21(12): p. 2035-41.

57. Chaudhuri, K.R. and Schapira, A.H., Non-motor symptoms of Parkinson's disease: dopaminergic pathophysiology and treatment. *Lancet Neurol*, **2009**. 8(5): p. 464-74.

58. Chaudhuri, K.R. and Naidu, Y., Early Parkinson's disease and non-motor issues. *J Neurol*, **2008**. 255: p. 33-8.

59. Collier, T.J., Kanaan, N.M., and Kordower, J.H., Ageing as a primary risk factor for Parkinson's disease: evidence from studies of non-human primates. *Nat Rev Neurosci*, **2011**. 12(6): p. 359-66.

60. Driver, J.A., et al., Incidence and remaining lifetime risk of Parkinson disease in advanced age. *Neurology*, **2009**. 72(5): p. 432-8.

61. Rodriguez, M., et al., Parkinson's disease as a result of aging. *Aging Cell*, **2015**. 14(3): p. 293-308.

62. Takubo, K., et al., Telomere lengths are characteristic in each human individual. *Exp Gerontol*, **2002**. 37(4): p. 523-31.

63. Double, K.L., et al., Selective cell death in neurodegeneration: why are some neurons spared in vulnerable regions? *Prog Neurobiol*, **2010**. 92(3): p. 316-29.

64. Kusumi, M., et al., Epidemiology of Parkinson's disease in Yonago City, Japan: comparison with a study carried out 12 years ago. *Neuroepidemiology*, **1996**. 15(4): p. 201-7.

65. Shulman, L.M., Gender differences in Parkinson's disease. *Gend Med*, **2007**. 4(1): p. 8-18.

66. Ozelius, L.J., et al., LRRK2 G2019S as a cause of Parkinson's disease in Ashkenazi Jews. *New England Journal of Medicine*, **2006**. 354(4): p. 424-425.

67. Gordon, P.H., et al., Parkinson's disease among American Indians and Alaska natives: a nationwide prevalence study. *Mov Disord*, **2012**. 27(11): p. 1456-9.

68. Wermuth, L., Pakkenberg, H., and Jeune, B., High age-adjusted prevalence of Parkinson's disease among Inuits in Greenland. *Neurology*, **2002**. 58(9): p. 1422-1425.

69. Polymeropoulos, M.H., et al., Mutation in the alpha-synuclein gene identified in families with Parkinson's disease. *Science*, **1997**. 276(5321): p. 2045-7.

70. Mullin, S. and Schapira, A., The genetics of Parkinson's disease. *Br Med Bull*, **2015**. 114(1): p. 39-52.

71. Keller, M.F., et al., Using genome-wide complex trait analysis to quantify 'missing heritability' in Parkinson's disease. *Hum Mol Genet*, **2012**. 21(22): p. 4996-5009.

72. Lill, C.M., et al., Comprehensive research synopsis and systematic meta-analyses in Parkinson's disease genetics: The PDGene database. *PLoS Genet*, **2012**. 8(3): p. e1002548.

73. Nalls, M.A., et al., Large-scale meta-analysis of genome-wide association data identifies six new risk loci for Parkinson's disease. *Nat Genet*, **2014**. 46(9): p. 989-93.

74. Marras, C., et al., Nomenclature of genetic movement disorders: Recommendations of the international Parkinson and movement disorder society task force. *Movement Disorders*, **2016**. 31(4): p. 436-457.

75. Marques, S.C., et al., Epigenetics in neurodegeneration: a new layer of complexity. *Prog Neuropsychopharmacol Biol Psychiatry*, **2011**. 35(2): p. 348-55.

76. Feng, Y., Jankovic, J., and Wu, Y.C., Epigenetic mechanisms in Parkinson's disease. *Journal of the Neurological Sciences*, **2015**. 349(1-2): p. 3-9.

77. Pan-Montojo, F. and Reichmann, H., Considerations on the role of environmental toxins in idiopathic Parkinson's disease pathophysiology. *Transl Neurodegener*, **2014**. 3: p. 10.

78. Brown, T.P., et al., Pesticides and Parkinson's disease--is there a link? *Environ Health Perspect*, **2006**. 114(2): p. 156-64.

79. Ritz, B., et al., Traffic-Related Air Pollution and Parkinson's Disease in Denmark: A Case-Control Study. *Environ Health Perspect*, **2016**. 124(3): p. 351-6.

80. Willis, A.W., et al., Metal emissions and urban incident Parkinson disease: a community health study of Medicare beneficiaries by using geographic information systems. *Am J Epidemiol*, **2010**. 172(12): p. 1357-63.

81. Harris, M.A., et al., Association of Parkinson's disease with infections and occupational exposure to possible vectors. *Mov Disord*, **2012**. 27(9): p. 1111-7.

82. Niehaus, I. and Lange, J.H., Endotoxin: is it an environmental factor in the cause of Parkinson's disease? *Occup Environ Med*, **2003**. 60(5): p. 378.

83. Crane, P.K., et al., Association of Traumatic Brain Injury With Late-Life Neurodegenerative Conditions and Neuropathologic Findings. *JAMA Neurol*, **2016**. 73(9): p. 1062-9.

84. Chin-Chan, M., Navarro-Yepes, J., and Quintanilla-Vega, B., Environmental pollutants as risk factors for neurodegenerative disorders: Alzheimer and Parkinson diseases. *Front Cell Neurosci*, **2015**. 9: p. 124.

85. Ehringer, H. and Hornykiewicz, O., Distribution of noradrenaline and dopamine (3-hydroxytyramine) in the human brain and their behavior in diseases of the extrapyramidal system. *Klin Wochenschr*, **1960**. 38: p. 1236-9.

86. Hornykiewicz, O., Dopamine miracle: from brain homogenate to dopamine replacement. *Mov Disord*, **2002**. 17(3): p. 501-8.

87. Cotzias, G.C., Van Woert, M.H., and Schiffer, L.M., Aromatic amino acids and modification of parkinsonism. *N Engl J Med*, **1967**. 276(7): p. 374-9.

88. LeWitt, P.A. and Fahn, S., Levodopa therapy for Parkinson disease: A look backward and forward. *Neurology*, **2016**. 86(14 Suppl 1): p. S3-12.

89. Aquino, C.C. and Fox, S.H., Clinical spectrum of levodopa-induced complications. *Mov Disord*, **2015**. 30(1): p. 80-9.

90. Poewe, W. and Antonini, A., Novel formulations and modes of delivery of levodopa. *Mov Disord*, **2015**. 30(1): p. 114-20.

91. Schapira, A.H., Monoamine oxidase B inhibitors for the treatment of Parkinson's disease: a review of symptomatic and potential disease-modifying effects. *CNS Drugs*, **2011**. 25(12): p. 1061-71.

92. Youdim, M.B.H. and Bakhle, Y.S., Monoamine oxidase: isoforms and inhibitors in Parkinson's disease and depressive illness. *British Journal of Pharmacology*, **2006**. 147: p. 287-96.

93. Youdim, M.B., Edmondson, D., and Tipton, K.F., The therapeutic potential of monoamine oxidase inhibitors. *Nat Rev Neurosci*, **2006**. 7(4): p. 295-309.

94. Connolly, B.S. and Lang, A.E., Pharmacological treatment of Parkinson disease: a review. *JAMA*, **2014**. 311(16): p. 1670-83.

95. Crosby, N., Deane, K.H., and Clarke, C.E., Amantadine in Parkinson's disease. *Cochrane Database Syst Rev*, **2003**(1): p. CD003468.

96. Jankovic, J. and Poewe, W., Therapies in Parkinson's disease. *Curr Opin Neurol*, **2012**. 25(4): p. 433-47.

97. Voges, J., et al., Thirty days complication rate following surgery performed for deep-brain-stimulation. *Mov Disord*, **2007**. 22(10): p. 1486-9.

98. Deuschl, G. and Agid, Y., Subthalamic neurostimulation for Parkinson's disease with early fluctuations: balancing the risks and benefits. *Lancet Neurol*, **2013**. 12(10): p. 1025-34.

99. Bloem, B.R., de Vries, N.M., and Ebersbach, G., Nonpharmacological treatments for patients with Parkinson's disease. *Mov Disord*, **2015**. 30(11): p. 1504-20.

100. Ahlskog, J.E., Does vigorous exercise have a neuroprotective effect in Parkinson disease? *Neurology*, **2011**. 77(3): p. 288-94.

101. Lotia, M. and Jankovic, J., New and emerging medical therapies in Parkinson's disease. *Expert Opin Pharmacother*, **2016**. 17(7): p. 895-909.

102. Schenk, D.B., et al., First-in-human assessment of PRX002, an anti-alpha-synuclein monoclonal antibody, in healthy volunteers. *Mov Disord*, **2017**. 32(2): p. 211-218.

103. Bartus, R.T., Weinberg, M.S., and Samulski, R.J., Parkinson's disease gene therapy: success by design meets failure by efficacy. *Mol Ther*, **2014**. 22(3): p. 487-497.

104. Blits, B. and Petry, H., Perspective on the Road toward Gene Therapy for Parkinson's Disease. *Front Neuroanat*, **2016**. 10: p. 128.

105. Olanow, C.W., et al., A double-blind controlled trial of bilateral fetal nigral transplantation in Parkinson's disease. *Ann Neurol*, **2003**. 54(3): p. 403-14.

106. Barker, R.A., Drouin-Ouellet, J., and Parmar, M., Cell-based therapies for Parkinson disease-past insights and future potential. *Nat Rev Neurol*, **2015**. 11(9): p. 492-503.

107. Brundin, P., Barker, R.A., and Parmar, M., Neural grafting in Parkinson's disease Problems and possibilities. *Prog Brain Res*, **2010**. 184: p. 265-94.

108. Barker, R.A., et al., Are Stem Cell-Based Therapies for Parkinson's Disease Ready for the Clinic in 2016? *J Parkinsons Dis*, **2016**. 6(1): p. 57-63.

109. Grealish, S., et al., Human ESC-derived dopamine neurons show similar preclinical efficacy and potency to fetal neurons when grafted in a rat model of Parkinson's disease. *Cell Stem Cell*, **2014**. 15(5): p. 653-65.

110. Kordower, J.H., et al., Lewy body-like pathology in long-term embryonic nigral transplants in Parkinson's disease. *Nat Med*, **2008**. 14(5): p. 504-6.

111. Li, J.Y., et al., Lewy bodies in grafted neurons in subjects with Parkinson's disease suggest host-to-graft disease propagation. *Nat Med*, **2008**. 14(5): p. 501-3.

112. Brundin, P. and Kordower, J.H., Neuropathology in transplants in Parkinson's disease: implications for disease pathogenesis and the future of cell therapy. *Prog Brain Res*, **2012**. 200: p. 221-41.

113. Ueda, K., et al., Molecular cloning of cDNA encoding an unrecognized component of amyloid in Alzheimer disease. *Proc Natl Acad Sci U S A*, **1993**. 90(23): p. 11282-6.

114. Jakes, R., Spillantini, M.G., and Goedert, M., Identification of two distinct synucleins from human brain. *FEBS Lett*, **1994**. 345(1): p. 27-32.

115. Polymeropoulos, M.H., et al., Mapping of a gene for Parkinson's disease to chromosome 4q21-q23. *Science*, **1996**. 274(5290): p. 1197-9.

116. Kruger, R., et al., Ala30Pro mutation in the gene encoding alpha-synuclein in Parkinson's disease. *Nat Genet*, **1998**. 18(2): p. 106-8.

117. Zarranz, J.J., et al., The new mutation, E46K, of alpha-synuclein causes Parkinson and Lewy body dementia. *Ann Neurol*, **2004**. 55(2): p. 164-73.

118. Appel-Cresswell, S., et al., Alpha-synuclein p.H50Q, a novel pathogenic mutation for Parkinson's disease. *Mov Disord*, **2013**. 28(6): p. 811-3.

119. Kiely, A.P., et al., alpha-Synucleinopathy associated with G51D SNCA mutation: a link between Parkinson's disease and multiple system atrophy? *Acta Neuropathol*, **2013**. 125(5): p. 753-69.

120. Chartier-Harlin, M.C., et al., Alpha-synuclein locus duplication as a cause of familial Parkinson's disease. *Lancet*, **2004**. 364(9440): p. 1167-9.

121. Singleton, A.B., et al., alpha-Synuclein locus triplication causes Parkinson's disease. *Science*, **2003**. 302(5646): p. 841.

122. Spillantini, M.G., et al., alpha-Synuclein in filamentous inclusions of Lewy bodies from Parkinson's disease and dementia with lewy bodies. *Proc Natl Acad Sci U S A*, **1998**. 95(11): p. 6469-73.

123. Nussbaum, R.L., The Identification of Alpha-Synuclein as the First Parkinson Disease Gene. *J Parkinsons Dis*, **2017**. 7(s1): p. 45-51.

124. Xia, Y., et al., Characterization of the human alpha-synuclein gene: Genomic structure, transcription start site, promoter region and polymorphisms. *J Alzheimers Dis*, **2001**. 3(5): p. 485-494.

125. Davidson, W.S., et al., Stabilization of alpha-synuclein secondary structure upon binding to synthetic membranes. *J Biol Chem*, **1998**. 273(16): p. 9443-9.

126. Rodriguez, J.A., et al., Structure of the toxic core of alpha-synuclein from invisible crystals. *Nature*, **2015**. 525(7570): p. 486-90.

127. Vilar, M., et al., The fold of alpha-synuclein fibrils. *Proc Natl Acad Sci U S A*, **2008**. 105(25): p. 8637-42.

128. Emamzadeh, F.N., Alpha-synuclein structure, functions, and interactions. *J Res Med Sci*, **2016**. 21: p. 29.

129. Ulmer, T.S., et al., Structure and dynamics of micelle-bound human alpha-synuclein. *Journal of Biological Chemistry*, **2005**. 280(10): p. 9595-9603.

130. Weinreb, P.H., et al., NACP, a protein implicated in Alzheimer's disease and learning, is natively unfolded. *Biochemistry*, **1996**. 35(43): p. 13709-15.

131. Lashuel, H.A., et al., The many faces of alpha-synuclein: from structure and toxicity to therapeutic target. *Nat Rev Neurosci*, **2013**. 14(1): p. 38-48.

132. Bartels, T., Choi, J.G., and Selkoe, D.J., alpha-Synuclein occurs physiologically as a helically folded tetramer that resists aggregation. *Nature*, **2011**. 477(7362): p. 107-10.

133. Wang, W., et al., A soluble alpha-synuclein construct forms a dynamic tetramer. *Proc Natl Acad Sci U S A*, **2011**. 108(43): p. 17797-802.

134. Fauvet, B., et al., alpha-Synuclein in central nervous system and from erythrocytes, mammalian cells, and Escherichia coli exists predominantly as disordered monomer. *J Biol Chem*, **2012**. 287(19): p. 15345-64.

135. Fauvet, B., et al., Characterization of semisynthetic and naturally Nalpha-acetylated alpha-synuclein in vitro and in intact cells: implications for aggregation and cellular properties of alpha-synuclein. *J Biol Chem*, **2012**. 287(34): p. 28243-62.

136. Chen, S.W., et al., Structural characterization of toxic oligomers that are kinetically trapped during alpha-synuclein fibril formation. *Protein Science*, **2015**. 24: p. 136-136.

137. Winner, B., et al., In vivo demonstration that alpha-synuclein oligomers are toxic. *Proceedings of the National Academy of Sciences of the United States of America*, **2011**. 108(10): p. 4194-4199.

138. Crowther, R.A., Daniel, S.E., and Goedert, M., Characterisation of isolated alpha-synuclein filaments from substantia nigra of Parkinson's disease brain. *Neurosci Lett*, **2000**. 292(2): p. 128-30.

139. Conway, K.A., et al., Accelerated oligomerization by Parkinson's disease linked alpha-synuclein mutants. *Ann N Y Acad Sci*, **2000**. 920: p. 42-5.

140. Bousset, L., et al., Structural and functional characterization of two alpha-synuclein strains. *Nat Commun*, **2013**. 4: p. 2575.

141. Giasson, B.I., et al., A hydrophobic stretch of 12 amino acid residues in the middle of alpha-synuclein is essential for filament assembly. *J Biol Chem*, **2001**. 276(4): p. 2380-6.

142. Der-Sarkissian, A., et al., Structural organization of alpha-synuclein fibrils studied by site-directed spin labeling. *J Biol Chem*, **2003**. 278(39): p. 37530-5.

143. Guerrero-Ferreira, R., et al., Cryo-EM structure of alpha-synuclein fibrils. *bioRxiv*, **2018**.

144. McLean, P.J., et al., Membrane association and protein conformation of alpha-synuclein in intact neurons. Effect of Parkinson's disease-linked mutations. *J Biol Chem*, **2000**. 275(12): p. 8812-6.

145. Jo, E., et al., alpha-Synuclein membrane interactions and lipid specificity. *J Biol Chem*, **2000**. 275(44): p. 34328-34.

146. Beyer, K., Mechanistic aspects of Parkinson's disease: alpha-synuclein and the biomembrane. *Cell Biochem Biophys*, **2007**. 47(2): p. 285-99.

147. Bartels, T., et al., The N-terminus of the intrinsically disordered protein alpha-synuclein triggers membrane binding and helix folding. *Biophys J*, **2010**. 99(7): p. 2116-24.

148. Pfefferkorn, C.M., Jiang, Z., and Lee, J.C., Biophysics of alpha-synuclein membrane interactions. *Biochim Biophys Acta*, **2012**. 1818(2): p. 162-71.

149. Middleton, E.R. and Rhoades, E., Effects of curvature and composition on alpha-synuclein binding to lipid vesicles. *Biophys J*, **2010**. 99(7): p. 2279-88.

150. Nuscher, B., et al., Alpha-synuclein has a high affinity for packing defects in a bilayer membrane: a thermodynamics study. *J Biol Chem*, **2004**. 279(21): p. 21966-75.

151. Alim, M.A., et al., Tubulin seeds alpha-synuclein fibril formation. *J Biol Chem*, **2002**. 277(3): p. 2112-7.

152. Chen, L., et al., Oligomeric alpha-synuclein inhibits tubulin polymerization. *Biochem Biophys Res Commun*, **2007**. 356(3): p. 548-53.

153. Liu, G., Aliaga, L., and Cai, H., alpha-synuclein, LRRK2 and their interplay in Parkinson's disease. *Future Neurol*, **2012**. 7(2): p. 145-153.

154. Alvarez-Castelao, B. and Castano, J.G., Synphilin-1 inhibits alpha-synuclein degradation by the proteasome. *Cell Mol Life Sci*, **2011**. 68(15): p. 2643-54.

155. Neystat, M., et al., Analysis of synphilin-1 and synuclein interactions by yeast two-hybrid beta-galactosidase liquid assay. *Neurosci Lett*, **2002**. 325(2): p. 119-23.

156. Lee, F.J., et al., Direct binding and functional coupling of alpha-synuclein to the dopamine transporters accelerate dopamine-induced apoptosis. *FASEB J*, **2001**. 15(6): p. 916-26.

157. Chen, R.H., et al., alpha-Synuclein membrane association is regulated by the Rab3a recycling machinery and presynaptic activity. *J Biol Chem*, **2013**. 288(11): p. 7438-49.

158. Wirdefeldt, K., et al., Expression of alpha-synuclein in the human brain: relation to Lewy body disease. *Brain Res Mol Brain Res*, **2001**. 92(1-2): p. 58-65.

159. Huang, Z., et al., Determining nuclear localization of alpha-synuclein in mouse brains. *Neuroscience*, **2011**. 199: p. 318-32.

160. Goers, J., et al., Nuclear localization of alpha-synuclein and its interaction with histones. *Biochemistry*, **2003**. 42(28): p. 8465-71.

161. Masliah, E., et al., Dopaminergic loss and inclusion body formation in alpha-synuclein mice: implications for neurodegenerative disorders. *Science*, **2000**. 287(5456): p. 1265-9.

162. Kahle, P.J., et al., Subcellular localization of wild-type and Parkinson's disease-associated mutant alpha -synuclein in human and transgenic mouse brain. *J Neurosci*, **2000**. 20(17): p. 6365-73.

163. Irizarry, M.C., et al., Characterization of the precursor protein of the non-A beta component of senile plaques (NACP) in the human central nervous system. *J Neuropathol Exp Neurol*, **1996**. 55(8): p. 889-95.

164. Murphy, D.D., et al., Synucleins are developmentally expressed, and alpha-synuclein regulates the size of the presynaptic vesicular pool in primary hippocampal neurons. *J Neurosci*, **2000**. 20(9): p. 3214-20.

165. Nemani, V.M., et al., Increased expression of alpha-synuclein reduces neurotransmitter release by inhibiting synaptic vesicle reclustering after endocytosis. *Neuron*, **2010**. 65(1): p. 66-79.

166. Lundblad, M., et al., Impaired neurotransmission caused by overexpression of alpha-synuclein in nigral dopamine neurons. *Proc Natl Acad Sci U S A*, **2012**. 109(9): p. 3213-9.

167. Scott, D. and Roy, S., alpha-Synuclein inhibits intersynaptic vesicle mobility and maintains recycling-pool homeostasis. *J Neurosci*, **2012**. 32(30): p. 10129-35.

168. Burre, J., The Synaptic Function of alpha-Synuclein. *J Parkinsons Dis*, **2015**. 5(4): p. 699-713.

169. Chandra, S., et al., Alpha-synuclein cooperates with CSPalpha in preventing neurodegeneration. *Cell*, **2005**. 123(3): p. 383-96.

170. Bonini, N.M. and Giasson, B.I., Snaring the function of alpha-synuclein. *Cell*, **2005**. 123(3): p. 359-61.

171. Burre, J., et al., Alpha-synuclein promotes SNARE-complex assembly in vivo and in vitro. *Science*, **2010**. 329(5999): p. 1663-7.

172. Burre, J., Sharma, M., and Sudhof, T.C., alpha-Synuclein assembles into higher-order multimers upon membrane binding to promote SNARE complex formation. *Proc Natl Acad Sci U S A*, **2014**. 111(40): p. E4274-83.

173. Wang, L., et al., alpha-synuclein multimers cluster synaptic vesicles and attenuate recycling. *Curr Biol*, **2014**. 24(19): p. 2319-26.

174. Ostrerova, N., et al., alpha-Synuclein shares physical and functional homology with 14-3-3 proteins. *J Neurosci*, **1999**. 19(14): p. 5782-91.

175. Park, S.M., et al., Distinct roles of the N-terminal-binding domain and the C-terminal-solubilizing domain of alpha-synuclein, a molecular chaperone. *J Biol Chem*, **2002**. 277(32): p. 28512-20.

176. Lucke, C., et al., Interactions between fatty acids and alpha-synuclein. *J Lipid Res*, **2006**. 47(8): p. 1714-24.

177. Jin, H., et al., alpha-Synuclein negatively regulates protein kinase Cdelta expression to suppress apoptosis in dopaminergic neurons by reducing p300 histone acetyltransferase activity. *J Neurosci*, **2011**. 31(6): p. 2035-51.

178. Zhu, M., et al., Alpha-synuclein can function as an antioxidant preventing oxidation of unsaturated lipid in vesicles. *Biochemistry*, **2006**. 45(26): p. 8135-42.

179. Latchoumycandane, C., et al., Protein kinase Cdelta is a key downstream mediator of manganese-induced apoptosis in dopaminergic neuronal cells. *J Pharmacol Exp Ther*, **2005**. 313(1): p. 46-55.

180. Kahle, P.J., et al., Physiology and pathophysiology of alpha-synuclein. Cell culture and transgenic animal models based on a Parkinson's disease-associated protein. *Ann N Y Acad Sci*, **2000**. 920: p. 33-41.

181. Rockenstein, E., et al., Differential neuropathological alterations in transgenic mice expressing alpha-synuclein from the platelet-derived growth factor and Thy-1 promoters. *J Neurosci Res*, **2002**. 68(5): p. 568-78.

182. Abeliovich, A., et al., Mice lacking alpha-synuclein display functional deficits in the nigrostriatal dopamine system. *Neuron*, **2000**. 25(1): p. 239-52.

183. Cabin, D.E., et al., Synaptic vesicle depletion correlates with attenuated synaptic responses to prolonged repetitive stimulation in mice lacking alpha-synuclein. *J Neurosci*, **2002**. 22(20): p. 8797-807.

184. Ibanez, P., et al., Causal relation between alpha-synuclein gene duplication and familial Parkinson's disease. *Lancet*, **2004**. 364(9440): p. 1169-71.

185. Melki, R., Role of Different Alpha-Synuclein Strains in Synucleinopathies, Similarities with other Neurodegenerative Diseases. *J Parkinsons Dis*, **2015**. 5(2): p. 217-27.

186. Luk, K.C., et al., Intracerebral inoculation of pathological alpha-synuclein initiates a rapidly progressive neurodegenerative alpha-synucleinopathy in mice. *J Exp Med*, **2012**. 209(5): p. 975-86.

187. Luk, K.C., et al., Pathological alpha-synuclein transmission initiates Parkinson-like neurodegeneration in nontransgenic mice. *Science*, **2012**. 338(6109): p. 949-53.

188. Caughey, B. and Lansbury, P.T., Protofibrils, pores, fibrils, and neurodegeneration: separating the responsible protein aggregates from the innocent bystanders. *Annu Rev Neurosci*, **2003**. 26: p. 267-98.

189. Campioni, S., et al., The presence of an air-water interface affects formation and elongation of alpha-Synuclein fibrils. *J Am Chem Soc*, **2014**. 136(7): p. 2866-75.

190. Conway, K.A., et al., Acceleration of oligomerization, not fibrillization, is a shared property of both alpha-synuclein mutations linked to early-onset Parkinson's disease: implications for pathogenesis and therapy. *Proc Natl Acad Sci U S A*, **2000**. 97(2): p. 571-6.

191. Ingelsson, M., Alpha-Synuclein Oligomers-Neurotoxic Molecules in Parkinson's Disease and Other Lewy Body Disorders. *Front Neurosci*, **2016**. 10: p. 408.

192. Rockenstein, E., et al., Accumulation of oligomer-prone alpha-synuclein exacerbates synaptic and neuronal degeneration in vivo. *Brain*, **2014**. 137(Pt 5): p. 1496-513.

193. Sharon, R., et al., The formation of highly soluble oligomers of alpha-synuclein is regulated by fatty acids and enhanced in Parkinson's disease. *Neuron*, **2003**. 37(4): p. 583-95.

194. Paleologou, K.E., et al., Detection of elevated levels of soluble alpha-synuclein oligomers in post-mortem brain extracts from patients with dementia with Lewy bodies. *Brain*, **2009**. 132(Pt 4): p. 1093-101.

195. Choi, B.K., et al., Large alpha-synuclein oligomers inhibit neuronal SNARE-mediated vesicle docking. *Proc Natl Acad Sci U S A*, **2013**. 110(10): p. 4087-92.

196. Diogenes, M.J., et al., Extracellular alpha-synuclein oligomers modulate synaptic transmission and impair LTP via NMDA-receptor activation. *J Neurosci*, **2012**. 32(34): p. 11750-62.

197. Volles, M.J., et al., Vesicle permeabilization by protofibrillar alpha-synuclein: implications for the pathogenesis and treatment of Parkinson's disease. *Biochemistry*, **2001**. 40(26): p. 7812-9.

198. Volles, M.J. and Lansbury, P.T., Jr., Vesicle permeabilization by protofibrillar alpha-synuclein is sensitive to Parkinson's disease-linked mutations and occurs by a pore-like mechanism. *Biochemistry*, **2002**. 41(14): p. 4595-602.

199. Danzer, K.M., et al., Different species of alpha-synuclein oligomers induce calcium influx and seeding. *J Neurosci*, **2007**. 27(34): p. 9220-32.

200. Mattson, M.P. and Chan, S.L., Dysregulation of cellular calcium homeostasis in Alzheimer's disease: bad genes and bad habits. *J Mol Neurosci*, **2001**. 17(2): p. 205-24.

201. Xilouri, M., Brekk, O.R., and Stefanis, L., alpha-Synuclein and protein degradation systems: a reciprocal relationship. *Mol Neurobiol*, **2013**. 47(2): p. 537-51.

202. Kaushik, S. and Cuervo, A.M., Proteostasis and aging. *Nat Med*, **2015**. 21(12): p. 1406-15.

203. Emmanouilidou, E., Stefanis, L., and Vekrellis, K., Cell-produced alpha-synuclein oligomers are targeted to, and impair, the 26S proteasome. *Neurobiol Aging*, **2010**. 31(6): p. 953-68.

204. Winslow, A.R., et al., alpha-Synuclein impairs macroautophagy: implications for Parkinson's disease. *J Cell Biol*, **2010**. 190(6): p. 1023-37.

205. Martinez-Vicente, M., et al., Dopamine-modified alpha-synuclein blocks chaperone-mediated autophagy. *J Clin Invest*, **2008**. 118(2): p. 777-88.

206. Mazzulli, J.R., et al., alpha-Synuclein-induced lysosomal dysfunction occurs through disruptions in protein trafficking in human midbrain synucleinopathy models. *Proc Natl Acad Sci U S A*, **2016**. 113(7): p. 1931-6.

207. Ryan, B.J., et al., Mitochondrial dysfunction and mitophagy in Parkinson's: from familial to sporadic disease. *Trends Biochem Sci*, **2015**. 40(4): p. 200-10.

208. Devi, L., et al., Mitochondrial import and accumulation of alpha-synuclein impair complex I in human dopaminergic neuronal cultures and Parkinson disease brain. *J Biol Chem*, **2008**. 283(14): p. 9089-100.

209. Robotta, M., et al., Alpha-synuclein binds to the inner membrane of mitochondria in an alpha-helical conformation. *Chembiochem*, **2014**. 15(17): p. 2499-502.

210. Swerdlow, R.H., et al., Matrilineal inheritance of complex I dysfunction in a multigenerational Parkinson's disease family. *Ann Neurol*, **1998**. 44(6): p. 873-81.

211. Parihar, M.S., et al., Alpha-synuclein overexpression and aggregation exacerbates impairment of mitochondrial functions by augmenting oxidative stress in human neuroblastoma cells. *Int J Biochem Cell Biol*, **2009**. 41(10): p. 2015-24.

212. Chinta, S.J., et al., Mitochondrial alpha-synuclein accumulation impairs complex I function in dopaminergic neurons and results in increased mitophagy in vivo. *Neurosci Lett*, **2010**. 486(3): p. 235-9.

213. Plotegher, N., Gratton, E., and Bubacco, L., Number and Brightness analysis of alpha-synuclein oligomerization and the associated mitochondrial morphology alterations in live cells. *Biochim Biophys Acta*, **2014**. 1840(6): p. 2014-24.

214. Nakamura, K., et al., Direct membrane association drives mitochondrial fission by the Parkinson disease-associated protein alpha-synuclein. *J Biol Chem*, **2011**. 286(23): p. 20710-26.

215. Luth, E.S., et al., Soluble, prefibrillar alpha-synuclein oligomers promote complex I-dependent, Ca2+-induced mitochondrial dysfunction. *J Biol Chem*, **2014**. 289(31): p. 21490-507.

216. Faustini, G., et al., Mitochondria and alpha-Synuclein: Friends or Foes in the Pathogenesis of Parkinson's Disease? *Genes (Basel)*, **2017**. 8(12).

217. Martinez, T.N. and Greenamyre, J.T., Toxin models of mitochondrial dysfunction in Parkinson's disease. *Antioxid Redox Signal*, **2012**. 16(9): p. 920-34.

218. Colla, E., et al., Accumulation of toxic alpha-synuclein oligomer within endoplasmic reticulum occurs in alpha-synucleinopathy in vivo. *J Neurosci*, **2012**. 32(10): p. 3301-5.

219. Colla, E., et al., Endoplasmic reticulum stress is important for the manifestations of alpha-synucleinopathy in vivo. *J Neurosci*, **2012**. 32(10): p. 3306-20.

220. Castillo-Carranza, D.L., et al., Differential activation of the ER stress factor XBP1 by oligomeric assemblies. *Neurochem Res*, **2012**. 37(8): p. 1707-17.

221. Park, J.Y., et al., Microglial phagocytosis is enhanced by monomeric alpha-synuclein, not aggregated alpha-synuclein: implications for Parkinson's disease. *Glia*, **2008**. 56(11): p. 1215-23.

222. Lee, H.J., et al., Direct transfer of alpha-synuclein from neuron to astroglia causes inflammatory responses in synucleinopathies. *J Biol Chem*, **2010**. 285(12): p. 9262-72.

223. Hoffmann, A., et al., Alpha-synuclein activates BV2 microglia dependent on its aggregation state. *Biochem Biophys Res Commun*, **2016**. 479(4): p. 881-886.

224. Zhang, W., et al., Aggregated alpha-synuclein activates microglia: a process leading to disease progression in Parkinson's disease. *FASEB J*, **2005**. 19(6): p. 533-42.

225. Wilms, H., et al., Suppression of MAP kinases inhibits microglial activation and attenuates neuronal cell death induced by alpha-synuclein protofibrils. *Int J Immunopathol Pharmacol*, **2009**. 22(4): p. 897-909.

226. Kim, C., et al., Neuron-released oligomeric alpha-synuclein is an endogenous agonist of TLR2 for paracrine activation of microglia. *Nat Commun*, **2013**. 4: p. 1562.

227. Arawaka, S., et al., Lewy body in neurodegeneration with brain iron accumulation type 1 is immunoreactive for alpha-synuclein. *Neurology*, **1998**. 51(3): p. 887-9.

228. Galvin, J.E., et al., Neurodegeneration with brain iron accumulation, type 1 is characterized by alpha-, beta-, and gamma-synuclein neuropathology. *Am J Pathol*, **2000**. 157(2): p. 361-8.

229. Takei, Y., et al., alpha-Synuclein coaggregation in familial amyotrophic lateral sclerosis with SOD1 gene mutation. *Hum Pathol*, **2013**. 44(6): p. 1171-6.

230. Forman, M.S., et al., Tau and alpha-synuclein pathology in amygdala of Parkinsonism-dementia complex patients of Guam. *Am J Pathol*, **2002**. 160(5): p. 1725-31.

231. Yancopoulou, D., et al., Tau and alpha-synuclein inclusions in a case of familial frontotemporal dementia and progressive aphasia. *J Neuropathol Exp Neurol*, **2005**. 64(3): p. 245-53.

232. Mori, F., et al., Pick's disease: alpha- and beta-synuclein-immunoreactive Pick bodies in the dentate gyrus. *Acta Neuropathol*, **2002**. 104(5): p. 455-61.

233. Nishioka, K., et al., Association of alpha-, beta-, and gamma-Synuclein with diffuse lewy body disease. *Arch Neurol*, **2010**. 67(8): p. 970-5.

234. Arai, K., et al., Pure autonomic failure in association with human alpha-synucleinopathy. *Neurosci Lett*, **2000**. 296(2-3): p. 171-3.

235. Mori, H., et al., Lewy bodies in progressive supranuclear palsy. *Acta Neuropathol*, **2002**. 104(3): p. 273-8.

236. Smith, B.R., et al., Neuronal inclusions of alpha-synuclein contribute to the pathogenesis of Krabbe disease. *J Pathol*, **2014**. 232(5): p. 509-21.

237. Yamashita, S., et al., Concomitant accumulation of alpha-synuclein and TDP-43 in a patient with corticobasal degeneration. *J Neurol*, **2014**. 261(11): p. 2209-17.

238. Jellinger, K.A., Significance of brain lesions in Parkinson disease dementia and Lewy body dementia. *Front Neurol Neurosci*, **2009**. 24: p. 114-25.

239. Parkkinen, L., et al., Widespread and abundant alpha-synuclein pathology in a neurologically unimpaired subject. *Neuropathology*, **2005**. 25(4): p. 304-14.

240. Parkkinen, L., Pirttila, T., and Alafuzoff, I., Applicability of current staging/categorization of alpha-synuclein pathology and their clinical relevance. *Acta Neuropathol*, **2008**. 115(4): p. 399-407.

241. Watanabe, I., Vachal, E., and Tomita, T., Dense core vesicles around the Lewy body in incidental Parkinson's disease: an electron microscopic study. *Acta Neuropathol*, **1977**. 39(2): p. 173-5.

242. Shahmoradian, S.H., et al., Lewy pathology in Parkinson's disease consists of a crowded organellar membranous medley. *bioRxiv*, **2017**.

243. Sato, S., et al., Loss of autophagy in dopaminergic neurons causes Lewy pathology and motor dysfunction in aged mice. *Sci Rep*, **2018**. 8(1): p. 2813.

244. Braak, H., et al., Gastric alpha-synuclein immunoreactive inclusions in Meissner's and Auerbach's plexuses in cases staged for Parkinson's disease-related brain pathology. *Neurosci Lett*, **2006**. 396(1): p. 67-72.

245. Brundin, P., et al., Research in motion: the enigma of Parkinson's disease pathology spread. *Nat Rev Neurosci*, **2008**. 9(10): p. 741-5.

246. Bieri, G., Gitler, A.D., and Brahic, M., Internalization, axonal transport and release of fibrillar forms of alpha-synuclein. *Neurobiol Dis*, **2018**. 109(Pt B): p. 219-225.

247. Devine, M.J., et al., Parkinson's disease and alpha-synuclein expression. *Mov Disord*, **2011**. 26(12): p. 2160-8.

248. Soldner, F., et al., Parkinson-associated risk variant in distal enhancer of alpha-synuclein modulates target gene expression. *Nature*, **2016**. 533(7601): p. 95-9.

249. Danzer, K.M., et al., Heat-shock protein 70 modulates toxic extracellular alpha-synuclein oligomers and rescues trans-synaptic toxicity. *FASEB J*, **2011**. 25(1): p. 326-36.

250. Freundt, E.C., et al., Neuron-to-neuron transmission of alpha-synuclein fibrils through axonal transport. *Ann Neurol*, **2012**. 72(4): p. 517-24.

251. Brahic, M., et al., Axonal transport and secretion of fibrillar forms of alpha-synuclein, Abeta42 peptide and HTTExon 1. *Acta Neuropathol*, **2016**. 131(4): p. 539-48.

252. Tran, H.T., et al., Alpha-synuclein immunotherapy blocks uptake and templated propagation of misfolded alpha-synuclein and neurodegeneration. *Cell Rep*, **2014**. 7(6): p. 2054-65.

253. Volpicelli-Daley, L.A., et al., Exogenous alpha-synuclein fibrils induce Lewy body pathology leading to synaptic dysfunction and neuron death. *Neuron*, **2011**. 72(1): p. 57-71.

254. Masuda-Suzukake, M., et al., Prion-like spreading of pathological alpha-synuclein in brain. *Brain*, **2013**. 136(Pt 4): p. 1128-38.

255. Recasens, A., et al., Lewy body extracts from Parkinson disease brains trigger alpha-synuclein pathology and neurodegeneration in mice and monkeys. *Ann Neurol*, **2014**. 75(3): p. 351-62.

256. Gousset, K., et al., Prions hijack tunnelling nanotubes for intercellular spread. *Nat Cell Biol*, **2009**. 11(3): p. 328-36.

257. Abounit, S., et al., Tunneling nanotubes spread fibrillar alpha-synuclein by intercellular trafficking of lysosomes. *EMBO J*, **2016**. 35(19): p. 2120-2138.

258. Dieriks, B.V., et al., alpha-synuclein transfer through tunneling nanotubes occurs in SH-SY5Y cells and primary brain pericytes from Parkinson's disease patients. *Sci Rep*, **2017**. 7: p. 42984.

259. Lee, H.J., Patel, S., and Lee, S.J., Intravesicular localization and exocytosis of alpha-synuclein and its aggregates. *J Neurosci*, **2005**. 25(25): p. 6016-24.

260. Jang, A., et al., Non-classical exocytosis of alpha-synuclein is sensitive to folding states and promoted under stress conditions. *J Neurochem*, **2010**. 113(5): p. 1263-74.

261. Lee, J.G., et al., Unconventional secretion of misfolded proteins promotes adaptation to proteasome dysfunction in mammalian cells. *Nat Cell Biol*, **2016**. 18(7): p. 765-76.

262. Fontaine, S.N., et al., DnaJ/Hsc70 chaperone complexes control the extracellular release of neurodegenerative-associated proteins. *EMBO J*, **2016**. 35(14): p. 1537-49.

263. Emmanouilidou, E., et al., Cell-produced alpha-synuclein is secreted in a calcium-dependent manner by exosomes and impacts neuronal survival. *J Neurosci*, **2010**. 30(20): p. 6838-51.

264. Alvarez-Erviti, L., et al., Lysosomal dysfunction increases exosome-mediated alpha-synuclein release and transmission. *Neurobiol Dis*, **2011**. 42(3): p. 360-7.

265. Pinotsi, D., et al., Nanoscopic insights into seeding mechanisms and toxicity of alpha-synuclein species in neurons. *Proc Natl Acad Sci U S A*, **2016**. 113(14): p. 3815-9.

266. Rey, N.L., et al., Transfer of human alpha-synuclein from the olfactory bulb to interconnected brain regions in mice. *Acta Neuropathol*, **2013**. 126(4): p. 555-73.

267. Guo, J.L., et al., Distinct alpha-synuclein strains differentially promote tau inclusions in neurons. *Cell*, **2013**. 154(1): p. 103-17.

268. Sacino, A.N., et al., Conformational templating of alpha-synuclein aggregates in neuronal-glial cultures. *Mol Neurodegener*, **2013**. 8: p. 17.

269. Lee, H.J., et al., Assembly-dependent endocytosis and clearance of extracellular alpha-synuclein. *Int J Biochem Cell Biol*, **2008**. 40(9): p. 1835-49.

270. Desplats, P., et al., Inclusion formation and neuronal cell death through neuron-to-neuron transmission of alpha-synuclein. *Proc Natl Acad Sci U S A*, **2009**. 106(31): p. 13010-5.

271. Konno, M., et al., Suppression of dynamin GTPase decreases alpha-synuclein uptake by neuronal and oligodendroglial cells: a potent therapeutic target for synucleinopathy. *Mol Neurodegener*, **2012**. 7: p. 38.

272. Sung, J.Y., et al., Induction of neuronal cell death by Rab5A-dependent endocytosis of alpha-synuclein. *J Biol Chem*, **2001**. 276(29): p. 27441-8.

273. Schonberger, O., et al., Novel heparan mimetics potently inhibit the scrapie prion protein and its endocytosis. *Biochem Biophys Res Commun*, **2003**. 312(2): p. 473-9.

274. Horonchik, L., et al., Heparan sulfate is a cellular receptor for purified infectious prions. *J Biol Chem*, **2005**. 280(17): p. 17062-7.

275. Holmes, B.B., et al., Heparan sulfate proteoglycans mediate internalization and propagation of specific proteopathic seeds. *Proc Natl Acad Sci U S A*, **2013**. 110(33): p. E3138-47.

276. Ihse, E., et al., Cellular internalization of alpha-synuclein aggregates by cell surface heparan sulfate depends on aggregate conformation and cell type. *Sci Rep*, **2017**. 7(1): p. 9008.

277. Mao, X., et al., Pathological alpha-synuclein transmission initiated by binding lymphocyte-activation gene 3. *Science*, **2016**. 353(6307).

278. Shrivastava, A.N., et al., alpha-synuclein assemblies sequester neuronal alpha3-Na+/K+-ATPase and impair Na+ gradient. *EMBO J*, **2015**. 34(19): p. 2408-23.

279. Surmeier, D.J., Obeso, J.A., and Halliday, G.M., Parkinson's Disease Is Not Simply a Prion Disorder. *J Neurosci*, **2017**. 37(41): p. 9799-9807.

280. Brundin, P. and Melki, R., Prying into the Prion Hypothesis for Parkinson's Disease. *J Neurosci*, **2017**. 37(41): p. 9808-9818.

281. Lee, S.J. and Masliah, E., Neurodegeneration: Aggregates feel the strain. *Nature*, **2015**. 522(7556): p. 296-7.

282. Peelaerts, W., et al., alpha-Synuclein strains cause distinct synucleinopathies after local and systemic administration. *Nature*, **2015**. 522(7556): p. 340-4.

283. Vingill, S., Connor-Robson, N., and Wade-Martins, R., Are rodent models of Parkinson's disease behaving as they should? *Behav Brain Res*, **2017**. 352: p. 133-41.

284. Lazaro, D.F., Pavlou, M.A.S., and Outeiro, T.F., Cellular models as tools for the study of the role of alpha-synuclein in Parkinson's disease. *Exp Neurol*, **2017**. 298(Pt B): p. 162-171.

285. Falkenburger, B.H. and Schulz, J.B., Limitations of cellular models in Parkinson's disease research. *J Neural Transm Suppl*, **2006**(70): p. 261-8.

286. Falkenburger, B.H., Saridaki, T., and Dinter, E., Cellular models for Parkinson's disease. *J Neurochem*, **2016**. 139: p. 121-130.

287. Astashkina, A., Mann, B., and Grainger, D.W., A critical evaluation of in vitro cell culture models for high-throughput drug screening and toxicity. *Pharmacol Ther*, **2012**. 134(1): p. 82-106.

288. Hansen, C., et al., alpha-Synuclein propagates from mouse brain to grafted dopaminergic neurons and seeds aggregation in cultured human cells. *J Clin Invest*, **2011**. 121(2): p. 715-25.

289. Lazaro, D.F., et al., Systematic comparison of the effects of alpha-synuclein mutations on its oligomerization and aggregation. *PLoS Genet*, **2014**. 10(11): p. e1004741.

290. Xie, H.R., Hu, L.S., and Li, G.Y., SH-SY5Y human neuroblastoma cell line: in vitro cell model of dopaminergic neurons in Parkinson's disease. *Chin Med J (Engl)*, **2010**. 123(8): p. 1086-92.

291. Wang, H.Q., et al., Cell type-specific upregulation of Parkin in response to ER stress. *Antioxid Redox Signal*, **2007**. 9(5): p. 533-42.

292. Kovalevich, J. and Langford, D., Considerations for the use of SH-SY5Y neuroblastoma cells in neurobiology. *Methods Mol Biol*, **2013**. 1078: p. 9-21.

293. Kriks, S., et al., Dopamine neurons derived from human ES cells efficiently engraft in animal models of Parkinson's disease. *Nature*, **2011**. 480(7378): p. 547-51.

294. Chung, C.Y., et al., Identification and rescue of alpha-synuclein toxicity in Parkinson patient-derived neurons. *Science*, **2013**. 342(6161): p. 983-7.

295. Xiao, B., et al., Induced pluripotent stem cells in Parkinson's disease: scientific and clinical challenges. *J Neurol Neurosurg Psychiatry*, **2016**. 87(7): p. 697-702.

296. Holmqvist, S., et al., Creation of a library of induced pluripotent stem cells from Parkinsonian patients. *NPJ Parkinsons Dis*, **2016**. 2: p. 16009.

297. Lotharius, J., et al., Effect of mutant alpha-synuclein on dopamine homeostasis in a new human mesencephalic cell line. *J Biol Chem*, **2002**. 277(41): p. 38884-94.

298. Lotharius, J., et al., Progressive degeneration of human mesencephalic neuron-derived cells triggered by dopamine-dependent oxidative stress is dependent on the mixed-lineage kinase pathway. *J Neurosci*, **2005**. 25(27): p. 6329-42.

299. Paul, G., et al., Tyrosine hydroxylase expression is unstable in a human immortalized mesencephalic cell line--studies in vitro and after intracerebral grafting in vivo. *Mol Cell Neurosci*, **2007**. 34(3): p. 390-9.

300. Schildknecht, S., et al., Requirement of a dopaminergic neuronal phenotype for toxicity of low concentrations of 1-methyl-4-phenylpyridinium to human cells. *Toxicol Appl Pharmacol*, **2009**. 241(1): p. 23-35.

301. Scholz, D., et al., Rapid, complete and large-scale generation of post-mitotic neurons from the human LUHMES cell line. *J Neurochem*, **2011**. 119(5): p. 957-71.

302. Stiegler, N.V., et al., Assessment of chemical-induced impairment of human neurite outgrowth by multiparametric live cell imaging in high-density cultures. *Toxicol Sci*, **2011**. 121(1): p. 73-87.

303. Tong, Z.B., et al., Characterization of three human cell line models for high-throughput neuronal cytotoxicity screening. *J Appl Toxicol*, **2017**. 37(2): p. 167-180.

304. Zhang, X.M., Yin, M., and Zhang, M.H., Cell-based assays for Parkinson's disease using differentiated human LUHMES cells. *Acta Pharmacol Sin*, **2014**. 35(7): p. 945-56.

305. Schildknecht, S., et al., Generation of genetically-modified human differentiated cells for toxicological tests and the study of neurodegenerative diseases. *ALTEX*, **2013**. 30(4): p. 427-44.

306. Stepkowski, T.M., Meczynska-Wielgosz, S., and Kruszewski, M., mitoLUHMES: An Engineered Neuronal Cell Line for the Analysis of the Motility of Mitochondria. *Cell Mol Neurobiol*, **2017**. 37(6): p. 1055-1066.

307. Efremova, L., et al., Prevention of the degeneration of human dopaminergic neurons in an astrocyte co-culture system allowing endogenous drug metabolism. *Br J Pharmacol*, **2015**. 172(16): p. 4119-32.

308. Efremova, L., et al., Switching from astrocytic neuroprotection to neurodegeneration by cytokine stimulation. *Arch Toxicol*, **2017**. 91(1): p. 231-246.

309. Ilieva, M. and Dufva, M., SOX2 and OCT4 mRNA-expressing cells, detected by molecular beacons, localize to the center of neurospheres during differentiation. *PLoS One*, **2013**. 8(8): p. e73669.

310. Smirnova, L., et al., A LUHMES 3D dopaminergic neuronal model for neurotoxicity testing allowing long-term exposure and cellular resilience analysis. *Arch Toxicol*, **2016**. 90(11): p. 2725-2743.

311. Dinh, N.D., et al., Microfluidic construction of minimalistic neuronal co-cultures. *Lab Chip*, **2013**. 13(7): p. 1402-12.

312. Scholz, D., Regulation of Alzheimer's disease-relevant protein processing in human neurons of the LUHMES cell line. *Dissertation*, **2011**.

313. Mehling, M. and Tay, S., Microfluidic cell culture. *Curr Opin Biotechnol*, **2014**. 25: p. 95-102.

314. Link, D.R., et al., Electric control of droplets in microfluidic devices. *Angew Chem Int Ed Engl*, **2006**. 45(16): p. 2556-60.

315. Vyawahare, S., Griffiths, A.D., and Merten, C.A., Miniaturization and parallelization of biological and chemical assays in microfluidic devices. *Chem Biol*, **2010**. 17(10): p. 1052-65.

316. Halldorsson, S., et al., Advantages and challenges of microfluidic cell culture in polydimethylsiloxane devices. *Biosens Bioelectron*, **2015**. 63: p. 218-31.

317. Toepke, M.W. and Beebe, D.J., PDMS absorption of small molecules and consequences in microfluidic applications. *Lab Chip*, **2006**. 6(12): p. 1484-6.

318. Zheng, W., et al., Fluid flow stress induced contraction and re-spread of mesenchymal stem cells: a microfluidic study. *Integr Biol (Camb)*, **2012**. 4(9): p. 1102-11.

319. Luk, K.C., et al., Exogenous alpha-synuclein fibrils seed the formation of Lewy body-like intracellular inclusions in cultured cells. *Proc Natl Acad Sci U S A*, **2009**. 106(47): p. 20051-6.

320. Brettschneider, J., et al., Spreading of pathology in neurodegenerative diseases: a focus on human studies. *Nat Rev Neurosci*, **2015**. 16(2): p. 109-20.

321. Guo, J.L. and Lee, V.M., Cell-to-cell transmission of pathogenic proteins in neurodegenerative diseases. *Nat Med*, **2014**. 20(2): p. 130-8.

322. Poehler, A.M., et al., Autophagy modulates SNCA/alpha-synuclein release, thereby generating a hostile microenvironment. *Autophagy*, **2014**. 10(12): p. 2171-92.

323. Taylor, A.M., et al., A microfluidic culture platform for CNS axonal injury, regeneration and transport. *Nat Methods*, **2005**. 2(8): p. 599-605.

324. Kunze, A., et al., Co-pathological connected primary neurons in a microfluidic device for Alzheimer studies. *Biotechnol Bioeng*, **2011**. 108(9): p. 2241-5.

325. Wu, J.W., et al., Small misfolded Tau species are internalized via bulk endocytosis and anterogradely and retrogradely transported in neurons. *J Biol Chem*, **2013**. 288(3): p. 1856-70.

326. Ilieva, M., et al., Tracking neuronal marker expression inside living differentiating cells using molecular beacons. *Front Cell Neurosci*, **2013**. 7: p. 266.

327. Nishimura, M., et al., Synaptophysin and chromogranin A immunoreactivities of Lewy bodies in Parkinson's disease brains. *Brain Res*, **1994**. 634(2): p. 339-44.

328. Maier, T., Guell, M., and Serrano, L., Correlation of mRNA and protein in complex biological samples. *FEBS Lett*, **2009**. 583(24): p. 3966-73.

329. Peng, C., Gathagan, R.J., and Lee, V.M., Distinct alpha-Synuclein strains and implications for heterogeneity among alpha-Synucleinopathies. *Neurobiol Dis*, **2018**. 109(Pt B): p. 209-218.

330. Richardson, S.C.W., *Tracking Intracellular Polymer Localization Via Fluorescence Microscopy*, in *Organelle-Specific Pharmaceutical Nanotechnology*, G.G.M.D.S. Volkmar Weissig, Editor. 2010, Wiley Online Library. p. 177-192.

331. Yagi, H., et al., Ultrasonication-dependent formation and degradation of alpha-synuclein amyloid fibrils. *Biochim Biophys Acta*, **2015**. 1854(3): p. 209-17.

332. Fusco, G., et al., Structural basis of membrane disruption and cellular toxicity by alpha-synuclein oligomers. *Science*, **2017**. 358(6369): p. 1440-1443.

333. Arnold, S.A., et al., Blotting-free and lossless cryo-electron microscopy grid preparation from nanoliter-sized protein samples and single-cell extracts. *J Struct Biol*, **2017**. 197(3): p. 220-226.

334. Kemmerling, S., et al., Single-cell lysis for visual analysis by electron microscopy. *J Struct Biol*, **2013**. 183(3): p. 467-473.

335. Arnold, S.A., et al., Total Sample Conditioning and Preparation of Nanoliter Volumes for Electron Microscopy. *ACS Nano*, **2016**. 10(5): p. 4981-8.

336. Dubochet, J., et al., Cryo-electron microscopy of vitrified specimens. *Q Rev Biophys*, **1988**. 21(2): p. 129-228.

337. Callaway, E., The revolution will not be crystallized: a new method sweeps through structural biology. *Nature*, **2015**. 525: p. 172-174.

338. Kuhlbrandt, W., Biochemistry. The resolution revolution. *Science*, **2014**. 343(6178): p. 1443-4.

339. Nogales, E., The development of cryo-EM into a mainstream structural biology technique. *Nature Methods*, **2015**. 13: p. 24-27.

340. Milazzo, A.-C., et al., Initial evaluation of a direct detection device detector for single particle cryo-electron microscopy. *Journal of Structural Biology*, **2011**. 176(3): p. 404-408.

341. Ruskin, R.S., Yu, Z., and Grigorieff, N., Quantitative characterization of electron detectors for transmission electron microscopy. *Journal of Structural Biology*, **2013**. 184(3): p. 385-393.

342. Veesler, D., et al., Maximizing the potential of electron cryomicroscopy data collected using direct detectors. *Journal of Structural Biology*, **2013**. 184(2): p. 193-202.

343. Grigorieff, N., FREALIGN: high-resolution refinement of single particle structures. *J Struct Biol*, **2007**. 157(1): p. 117-25.

344. Lyumkis, D., et al., Likelihood-based classification of cryo-EM images using FREALIGN. *J Struct Biol*, **2013**. 183(3): p. 377-88.

345. Scheres, S.H.W., RELION: implementation of a Bayesian approach to cryo-EM structure determination. *Journal of Structural Biology*, **2012**. 180(3): p. 519-530.

346. Baker, L.A. and Rubinstein, J.L., Chapter fifteen – radiation damage in electron cryomicroscopy. *Methods in enzymology*, **2010**.

347. Kemmerling, S., et al., Connecting μ-fluidics to electron microscopy. *J Struct Biol*, **2012**. 177(1): p. 128-34.

348. Glaeser, R.M., How good can cryo-EM become ? *Nat Methods*, **2016**. 13: p. 28-32.

349. Jain, T., et al., Spotiton: a prototype for an integrated inkjet dispense and vitrification system for cryo-TEM. *Journal of structural biology*, **2012**. 179: p. 68-75.

350. Razinkov, I., et al., A new method for vitrifying samples for cryoEM. *Journal of Structural Biology*, **2016**. 195(2): p. 190-198.

351. Magdesian, M.H., et al., Rapid Mechanically Controlled Rewiring of Neuronal Circuits. *J Neurosci*, **2016**. 36(3): p. 979-87.

352. Konradi, R., Acikgoz, C., and Textor, M., Polyoxazolines for nonfouling surface coatings--a direct comparison to the gold standard PEG. *Macromol Rapid Commun*, **2012**. 33(19): p. 1663-76.

353. Ogaki, R., et al., Temperature-induced ultradense PEG polyelectrolyte surface grafting provides effective long-term bioresistance against mammalian cells, serum, and whole blood. *Biomacromolecules*, **2012**. 13(11): p. 3668-77.

354. Kovach, K.M., et al., The effects of PEG-based surface modification of PDMS microchannels on long-term hemocompatibility. *J Biomed Mater Res A*, **2014**. 102(12): p. 4195-205.

355. Wachter, A., et al., Analysis of Reverse Phase Protein Array Data: From Experimental Design towards Targeted Biomarker Discovery. *Microarrays (Basel)*, **2015**. 4(4): p. 520-39.

356. Tabakman, S.M., et al., Plasmonic substrates for multiplexed protein microarrays with femtomolar sensitivity and broad dynamic range. *Nat Commun*, **2011**. 2: p. 466.

357. Chang, H., et al., PSA Detection with Femtomolar Sensitivity and a Broad Dynamic Range Using SERS Nanoprobes and an Area-Scanning Method. *ACS Sensors*, **2016**. 1(6): p. 645-649.

358. Brase, J.C., et al., Increasing the sensitivity of reverse phase protein arrays by antibody-mediated signal amplification. *Proteome Sci*, **2010**. 8: p. 36.

359. Arnold, S.A., Nanoliter sample preparation for electron microscopy and single-cell analysis. *(Doctoral dissertation)*, **2017**.

360. Frey, T.G., Perkins, G.A., and Ellisman, M.H., Electron tomography of membrane-bound cellular organelles. *Annu Rev Biophys Biomol Struct*, **2006**. 35: p. 199-224.

361. Shahmoradian, S.H., et al., Preparation of primary neurons for visualizing neurites in a frozen-hydrated state using cryo-electron tomography. *J Vis Exp*, **2014**(84): p. e50783.

362. Garvalov, B.K., et al., Luminal particles within cellular microtubules. *J Cell Biol*, **2006**. 174(6): p. 759-65.

363. Lucic, V., et al., Multiscale imaging of neurons grown in culture: from light microscopy to cryo-electron tomography. *J Struct Biol*, **2007**. 160(2): p. 146-56.

364. Fernandez-Busnadiego, R., et al., Insights into the molecular organization of the neuron by cryo-electron tomography. *J Electron Microsc (Tokyo)*, **2011**. 60 Suppl 1: p. S137-48.

365. Ibiricu, I., et al., Cryo electron tomography of herpes simplex virus during axonal transport and secondary envelopment in primary neurons. *PLoS Pathog*, **2011**. 7(12): p. e1002406.

366. Tao, C.L., et al., Differentiation and Characterization of Excitatory and Inhibitory Synapses by Cryo-electron Tomography and Correlative Microscopy. *J Neurosci*, **2018**. 38(6): p. 1493-1510.

367. Gao, F., et al., Mitophagy in Parkinson's Disease: Pathogenic and Therapeutic Implications. *Front Neurol*, **2017**. 8: p. 527.

368. Ludtmann, M.H., et al., Monomeric Alpha-Synuclein Exerts a Physiological Role on Brain ATP Synthase. *J Neurosci*, **2016**. 36(41): p. 10510-10521.

369. Subramaniam, S.R., et al., Region specific mitochondrial impairment in mice with widespread overexpression of alpha-synuclein. *Neurobiol Dis*, **2014**. 70: p. 204-13.

370. Tapias, V., et al., Synthetic alpha-synuclein fibrils cause mitochondrial impairment and selective dopamine neurodegeneration in part via iNOS-mediated nitric oxide production. *Cell Mol Life Sci*, **2017**. 74(15): p. 2851-2874.

371. Pozo Devoto, V.M. and Falzone, T.L., Mitochondrial dynamics in Parkinson's disease: a role for alpha-synuclein? *Dis Model Mech*, **2017**. 10(9): p. 1075-1087.

372. Mastronarde, D.N., Automated electron microscope tomography using robust prediction of specimen movements. *J Struct Biol*, **2005**. 152(1): p. 36-51.

373. Jacob, W.A., et al., Mitochondrial matrix granules: their behavior during changing metabolic situations and their relationship to contact sites between inner and outer mitochondrial membranes. *Microsc Res Tech*, **1994**. 27(4): p. 307-18.

374. Peachey, L.D., Electron Microscopic Observations on the Accumulation of Divalent Cations in Intramitochondrial Granules. *J Cell Biol*, **1964**. 20: p. 95-111.

375. Raza, M., et al., Aging is associated with elevated intracellular calcium levels and altered calcium homeostatic mechanisms in hippocampal neurons. *Neurosci Lett*, **2007**. 418(1): p. 77-81.

376. Beirowski, B., et al., The progressive nature of Wallerian degeneration in wild-type and slow Wallerian degeneration (WldS) nerves. *BMC Neurosci*, **2005**. 6: p. 6.

377. Kerschensteiner, M., et al., In vivo imaging of axonal degeneration and regeneration in the injured spinal cord. *Nat Med*, **2005**. 11(5): p. 572-7.

378. Krug, A.K., et al., Transcriptional and metabolic adaptation of human neurons to the mitochondrial toxicant MPP(+). *Cell Death Dis*, **2014**. 5: p. e1222.

379. Nonaka, T., et al., Seeded aggregation and toxicity of alpha-synuclein and tau: cellular models of neurodegenerative diseases. *J Biol Chem*, **2010**. 285(45): p. 34885-98.

380. Huang, C., et al., A new method for purification of recombinant human alpha-synuclein in Escherichia coli. *Protein Expr Purif*, **2005**. 42(1): p. 173-7.

381. Biyani, N., et al., Focus: The interface between data collection and data processing in cryo-EM. *J Struct Biol*, **2017**. 198(2): p. 124-133.

382. Hu, Y., Qu, L., and Schikorski, T., Mean synaptic vesicle size varies among individual excitatory hippocampal synapses. *Synapse*, **2008**. 62(12): p. 953-7.

ACKNOWLEDGEMENTS

First of all, I would like to thank Thomas Braun and Henning Stahlberg for the opportunity to do my PhD under their supervision and for providing a great environment for research. I am also honored that Prof. Dr. Roland Riek accepted to be the external co-referee for my thesis.

I wish to greatly acknowledge Rosmarie Sütterlin for bringing some light in an electron microscopy lab. She did most of the immunolabeling work, sat hours at the confocal, and often took the turn for the weekend cell culture maintenance.

Many thanks to Gabriel Schweighauser, Elliot Smith, and Adrian Najer for proof-reading my thesis.

I thank Mohamed, Kenny, Lubomir, Carola and Ariane for discussions about sample preparation, help with microscopy work, and maintenance of the microscopes.

I would like to thank Alexander Stettler for letting me into his cleanroom and Albert Martel for helping me to keep everything clean in there.

Stefan Arnold and Claudio Schmidli is thanked for collaboration on their setup.

Thanks to the administrative professionals Karen Bergmann and Heidi Brönnimann who kept most bureaucracy far from me.

I thank Pratibha Kumari and Cedric Eichmann for the help with α-syn, and Simon Gutbier for the introduction into LUHMES cell culturing.

With a special mention to my former colleagues, Benjamin Bircher, Stefan Arnold, Gabriel Schweighauser, Christopher Bleck, Simon Kemmerling, Sebastian Scherrer, Misha Kudryashev and Jarek Sedzick. It was fantastic to work with you guys during some parts of my PhD.

Furthermore, I would like to greatly acknowledge the nice and group atmospheres I have met in this lab. To all Braunis and Cina wutzl team: have a good time and keep training.

I would like to thank all my friends and my former flatmates. We had a great time in basel.

I am grateful to my siblings and parents, who have provided me support during my studies for the last decade.

Finally, and the most, I would like to thank Mona, for her patience and support.

Big thanks for all your help and support!